Lateral Superlattices in Commensurate Magnetic Fields: Electronic Structure, Transport and Optical Properties

Anisimovas, Egidijus

2001

Lateral Superlattices in Commensurate Magnetic Fields: Electronic Structure, Transport and Optical Properties

Egidijus ANISIMOVAS

Division of Solid State Theory
Department of Physics
Lund University

Faculty opponent: Prof. Antti-Pekka Jauho
Mikroelektronik Centret, Technical University of Denmark

To be presented, with the permission of the Faculty of Mathematics and Natural Sciences of Lund University, for public criticism in the Lecture hall B of the Department of Physics on Friday, 18th of May 2001, at 13:15.

Preface

The time has come, the Walrus said,
To talk of many things ...

Lewis Carroll, "Through the Looking Glass"

The time has come, indeed, and we shall talk of the many different things that make up the contents of my PhD thesis produced during the (nearly) four years spent at the Division of Solid State Theory of the Lund University.

The main topic of the thesis is the physics of interacting two-dimensional electrons moving in a perpendicular magnetic field combined with a lateral periodic potential. The two ingredients of the physical problem – the magnetic field and the bidirectionally modulated periodic potential – strongly disagree with each other and their quarrel leads to an admirable jewel of beautiful physics and the underlying mathematics. To make a long story short, the magnetic field tends to define a periodicity of its own with a lattice constant that does not necessarily agree well with that of the periodic modulation. This (dis)agreement is often referred to as (in)commensurability and results in an intricate internal structure of the electron energy spectrum which is known as the "butterfly". You will find a high-resolution picture of it somewhere in Chapter 3. The butterfly is not just a theorist's dream; in the recent years, a number of experimental groups have managed to overcome the involved difficulties and have captured some manifestations of the complicated spectrum. First it was done in the measurements of the lateral transport and, what I was particularly delighted to learn, only last year the butterfly was spotted in the integer quantum Hall effect data.

The present thesis consists of two parts. First, there comes a series of three introductory – or rather Background, as I like to call them – Chapters. They briefly run through the key issues leading us into the field of the thesis: two-dimensional electrons in strong magnetic fields, magnetic translations, suitable basis function sets, commensurability, and so on. The second part is a collection of original papers, listed here in the order they appear in the thesis:

1. E. Anisimovas and P. Johansson, *Butterfly-like Spectra and Collective Modes of Antidot Superlattices in Magnetic Fields*, Phys. Rev. B **60**, 7744 (1999).

2. E. Anisimovas and P. Johansson, *Electronic Structure of Antidot Superlattices in Commensurate Magnetic Fields*, J. Phys.: Condens. Matter **13**, 3365 (2001).
3. E. Anisimovas, *Tunneling Spectroscopy of Modulated Two-Dimensional Electron Systems.*
4. E. Anisimovas, *Hydrodynamics of Antidot Superlattices.*
5. E. Anisimovas and P. Johansson, *Tip Geometry Effects in Circularly Polarized Light Emission from a Scanning Tunneling Microscope*, Phys. Rev. B **59**, 5126 (1999).

All the results presented in the papers are obtained by me personally, and therefore, I am to be held responsible for all of their contents. The last paper is devoted to the light emission from an operating scanning tunneling microscope (STM) and lies somewhat outside the main stream. It does deal with tunneling and collective electronic excitations, however, in a different physical system. Nevertheless, I decided to include it in the thesis as representing a part of my general physical background. There was one more paper written by me which I *do not* include:

0. E. Anisimovas and A. Matulis, *Energy Spectra of Few-electron Quantum Dots*, J. Phys.: Condens. Matter **10**, 601 (1998).

Most of this work was done before I came to Lund.

Numerous thanks go, first of all, to my advisors Dr. Peter Johansson and Prof. Koung-An Chao, as well as other members of the group. While it is certainly difficult to list everybody with whom I have enjoyed enlightening conversations, I would like to particularly mention Prof. Yuri M. Galperin, Prof. Algirdas Matulis, Prof. Eivind-Hiis Hauge, Prof. Allan H. MacDonald, and Dr. Carlo M. Canali.

I think it was a fortune to carry out my PhD work at this Division, a part of whose members work on quite a different set of problems – the many-body theory – and talk a different language. From them I certainly picked up much inspiration and wisdom, for example, writing my own bandstructure code for commensurate magnetic fields. It is always healthy to keep one's mind open to ideas from outside. The people who deserve the credit are: Prof. Lars Hedin, Dr. Carl-Olof Almbladh, Dr. Ulf von Barth, Dr. Ferdi Aryasetiawan, Dr. Robert van Leeuwen, Dr. Stefan Kurth and Nils-Erik Dahlen. Nils has also kindly agreed to read the introductory Chapters and corrected a few misprints.

The financial support from the Swedish Natural Sciences Research Council (NFR), the Nordic Academy for Advanced Studies (NORFA), the National Science Council (NSC) of Taiwan, and the Swedish Royal Academy of Sciences (KVA) was appreciated. I would like to thank Prof. Yuri M. Galperin of the University of Oslo and the Advanced Study Center (Oslo, Norway) for their warm hospitality during the total of 1.5 months that I have spent in Oslo. Likewise, thanks go to Prof. Tsin-Fu Jiang of the National Chiao Tung University (Hsinchu, Taiwan) for everything that has taken place during the exciting month in Taiwan in spring 2000.

Lund, April 2001

Contents

CHAPTER 1

Electron Motion in Magnetic Field

1.1 Formalisms

The motion of a particle of mass m and charge $-e$ (an electron) in the presence of an external electromagnetic field, given in terms of its scalar and vector potentials ϕ and $\mathbf{A}$, respectively, is described by the Lagrangian

$$\mathcal{L} = \frac{m\mathbf{v}^2}{2} + e\phi - \frac{e}{c}\mathbf{v}\cdot\mathbf{A}. \tag{1.1}$$

This expression is most easily understood by noting that the first two terms on the left-hand side of (1.1) represent the usual difference of the kinetic and potential energies, and the last term supplements the contribution of the scalar potential by that of the vector potential in an explicitly covariant form. The presence of the term involving the vector potential $\mathbf{A}$ will supply an extra term to the action

$$S[\mathbf{r}(\tau)] = \int_0^t \mathcal{L}\left(\mathbf{r}, \frac{d\mathbf{r}}{d\tau}\right) d\tau = S_0[\mathbf{r}(\tau)] - \frac{e}{c}\int d\mathbf{r}\cdot\mathbf{A}, \tag{1.2}$$

here S_0 denotes the action in the absence of the magnetic field ($\mathbf{A} = 0$). The semiclassical propagator $G = \exp(iS/\hbar)$ will correspondingly be modified by a phase factor

$$G = G_0 \exp\left(-\frac{ie}{c\hbar}\int d\mathbf{r}\cdot\mathbf{A}\right) \tag{1.3}$$

with G_0 being the zero-field propagator. While the expression (1.3) is manifestly gauge-dependent, the physically meaningful quantity is the phase accumulated by an electron traversing a closed path or, equivalently, a difference of two phases corresponding to two distinct paths sharing the same origin and the destination.

The closed-contour integral of $\mathbf{A}$ equals the magnetic flux Φ penetrating the enclosed area, therefore, the exponential in (1.3) can be written as

$$\exp\left(-\frac{ie}{c\hbar}\oint d\mathbf{r}\cdot\mathbf{A}\right)=\exp\left(-2\pi i\frac{\Phi}{\Phi_0}\right)\quad\text{with}\quad\Phi_0=\frac{ch}{e},\tag{1.4}$$

here we introduced the *magnetic flux quantum* $\Phi_0 = 4.13570\cdot10^{-7}\mathrm{G\,cm^2}$, a quantity of fundamental importance to the subject. The magnetic flux sensitive phase (1.4) can be measured in an experimental setup of the Aharonov-Bohm type. It is exactly this phase that is responsible for bringing about the commensurability-related phenomena in antidot superlattices as well as the crystal momentum shifts in tunneling perpendicular to magnetic field, two main issues considered in the present thesis.

Carrying out the transformation to the Hamiltonian formalism starting with Eq. (1.1) we find the distinction between the canonical ($\mathbf{p}$) and kinetic ($\mathbf{p}_{\mathrm{kin}}$) momenta in finite magnetic fields

$$\mathbf{p}=\frac{\partial L}{\partial\mathbf{v}}=m\mathbf{v}-\frac{e}{c}\mathbf{A},\quad\text{thus}\quad\mathbf{p}_{\mathrm{kin}}\equiv m\mathbf{v}=\mathbf{p}+\frac{e}{c}\mathbf{A},\tag{1.5}$$

and arrive at the following Hamiltonian describing the motion of a free particle in a magnetic field

$$H=\frac{1}{2m}\mathbf{p}_{\mathrm{kin}}^2=\frac{1}{2m}\left(\mathbf{p}+\frac{e}{c}\mathbf{A}\right)^2.\tag{1.6}$$

1.2 **Landau Gauge**

The two commonly used gauges for the vector potential $\mathbf{A}$ are the so-called symmetric gauge given by $\mathbf{A}=\mathbf{B}\times\mathbf{r}/2$, and the Landau gauge $A_y = Bx$ (or alternatively $A_x = -By$).

Before proceeding to the consideration of the solutions to the Hamiltonian (1.6) in either gauge, it is advisable to simplify the expressions by introducing the natural dimensionless units of the length and energy. These are the magnetic length l_c and the cyclotron energy $\hbar\omega_c$, respectively, and are given by

$$l_c=\sqrt{\frac{\hbar c}{eB}},\quad\hbar\omega_c=\frac{\hbar eB}{mc}.\tag{1.7}$$

In these units, the Hamiltonian (1.6) in the Landau gauge is written as

$$H=\frac{1}{2}p_x^2+\frac{1}{2}(p_y+x)^2,\tag{1.8}$$

and obviously commutes with p_y. Therefore, we look for solutions of the form

$$\psi_k(x,y) = \frac{1}{\sqrt{2\pi}} \mathrm{e}^{iky} \varphi(x), \tag{1.9}$$

consisting of a plane wave propagating in the y direction and some function φ of x. Making a substitution $x \to x - k$ we arrive at the following equation for φ

$$\left(-\frac{1}{2}\frac{d^2}{dx^2} + \frac{1}{2}x^2 - E \right) \varphi(x-k) = 0, \tag{1.10}$$

which coincides with the harmonic oscillator equation. Thus, we identify the solutions to (1.10) $\varphi_n(x-k)$ with the harmonic oscillator functions $\chi_n(x)$ and write the total wave function as

$$\begin{aligned} \psi_{nk}(x,y) &= \frac{1}{\sqrt{2\pi}} \mathrm{e}^{iky} \chi_n(x+k), \\ \chi_n(x) &= \left[\sqrt{\pi} n!\, 2^n\right]^{-1/2} \mathrm{e}^{-x^2/2} H_n(x), \end{aligned} \tag{1.11}$$

where H_n denotes the n-th Hermite polynomial. The energy of the state ψ_{nk} is $E_n = (n + 1/2)$ and does not depend on k. Thus, the resulting energy levels, enumerated by the quantum number n and commonly known as the Landau levels, are highly (extensively) degenerate.

1.3 Symmetric gauge

The problem of a single electron moving in a uniform magnetic field can also be approached in the symmetric-gauge formulation leading to a different set of solutions. Of course, since the physical problem is the same the members of one set of solutions are always expressible as linear combinations of the other set. Let us take a brief look at the solution of the problem in the symmetric gauge. The Hamiltonian now reads

$$H = \frac{1}{2}(p_x - y/2)^2 + \frac{1}{2}(p_y + x/2)^2, \tag{1.12}$$

and written in the polar coordinates (ρ, ϕ) becomes

$$H = -\frac{1}{2}\nabla^2 + \frac{1}{8}\rho^2 + \frac{1}{2} l_z, \quad l_z = -i\frac{\partial}{\partial \phi}. \tag{1.13}$$

Here we introduced the angular momentum operator l_z which, owing to the angular symmetry, commutes with the Hamiltonian (1.13). Therefore, we look for

the solutions whose angular dependence is described by the angular momentum eigenfunctions

$$\psi_m(\rho,\phi) = \frac{1}{\sqrt{2\pi}} \mathrm{e}^{im\phi} R(\rho). \tag{1.14}$$

Using

$$\nabla^2 = \frac{\partial^2}{\partial\rho^2} + \frac{1}{\rho}\frac{\partial}{\partial\rho} + \frac{1}{\rho^2}\frac{\partial}{\partial\phi^2} = \frac{1}{\rho}\frac{\partial}{\partial\rho}\left(\rho\frac{\partial}{\partial\rho}\right) + \frac{1}{\rho^2}\frac{\partial}{\partial\phi^2}$$

we arrive at the equation for the radial function $R(\rho)$

$$\frac{1}{\rho}\frac{d}{d\rho}\left(\rho\frac{dR(\rho)}{d\rho}\right) + \left[(2E-m) - \frac{m^2}{\rho^2} - \frac{\rho^2}{4}\right] R(\rho) = 0. \tag{1.15}$$

Making the substitution $\rho^2 = 2x$ we transform the equation into

$$xR''(x) + R'(x) + \left[-\frac{x}{4} + \frac{2E-m}{2} - \frac{m^2}{4x}\right] R(x) = 0 \tag{1.16}$$

which is solved by the (unnormalized) Laguerre functions

$$R_{n_r,k} = \mathrm{e}^{-x/2} x^{k/2} L^k_{n_r}(x).$$

The radial quantum number n_r and the order of the Laguerre polynomial k are related to the parameters entering Eq. (1.16) by $2E - m = 2n_r + k + 1$ and $m^2 = k^2$. Thus we express

$$\begin{aligned} E_n &= n + \frac{1}{2} \quad \text{with } n = n_r + \frac{m+|m|}{2}, \\ \psi_{nm}(\rho,\phi) &= \sqrt{\frac{n_r!}{2\pi 2^{|m|}(n_r+|m|)!}}\, \mathrm{e}^{-\rho^2/4} \rho^{|m|} \mathrm{e}^{im\phi} L^{|m|}_{n_r}\left(\frac{\rho^2}{2}\right), \end{aligned} \tag{1.17}$$

here we also evaluated the normalization prefactor. The electron states can be uniquely identified by specifying the angular momentum quantum number $m = 0, \pm1, \pm2, \ldots$ and either the radial $n_r = 0, 1, 2, \ldots$ or the Landau level $n = 0, 1, 2, \ldots$ quantum number. The relation between the two alternative sets is schematically shown in Fig. 1.1. The dashed lines join the states that belong to the same Landau level. We observe that in each Landau level the possible values of the angular momentum m run from $-\infty$ to the maximum possible value $m = n$. The states possessing the maximum possible value of the angular momentum in each Landau level are encircled by a dotted line.

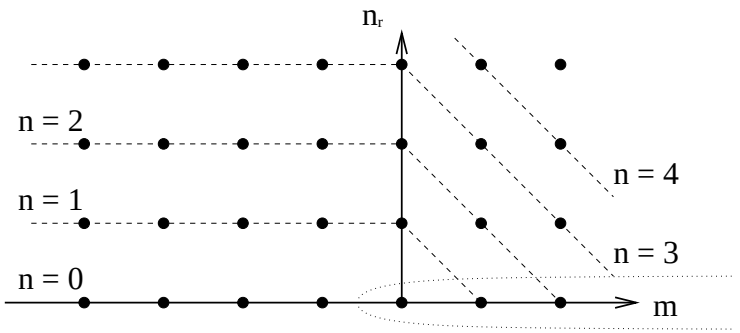

Figure 1.1: Schematic diagram of electron states in a uniform magnetic field.

Let us briefly discuss the states with $n_r = 0$ lying on the m-axis in Fig. 1.1. For the negative values of the angular momentum m these states span the lowest Landau level and can be written in a particularly simple way using the complex number notation

$$\psi_m(\rho,\phi) = \frac{1}{\sqrt{2\pi 2^{|m|}|m|!}}\,\mathrm{e}^{-\rho^2/4}(x-iy)^{|m|}, \tag{1.18}$$

whereas for the positive angular momenta m we obtain the above mentioned states of the maximum possible angular momentum

$$F_n(\rho,\phi) = \frac{1}{\sqrt{2\pi 2^n n!}}\,\mathrm{e}^{-\rho^2/4}(x+iy)^n. \tag{1.19}$$

These states play an important role in the construction of localized basis function sets spanning the respective Landau levels, and will be further discussed in Sec. 1.6.

1.4 Canonical transformation

In this Section, we will discuss the solution of the problem of electron motion in a uniform magnetic field using a canonical coordinate transformation. To be specific, we work in the symmetric gauge, while the corresponding analysis in the Landau gauge is identical in spirit. We start with the symmetric-gauge

Hamiltonian

$$H = \frac{1}{2}(p_x - y/2)^2 + \frac{1}{2}(p_y + x/2)^2, \tag{1.20}$$

and also define the magnetic translation operators

$$T_M(\mathbf{R}) = \exp\left\{-iR_x\left(p_x + \frac{y}{2}\right) - iR_y\left(p_y - \frac{x}{2}\right)\right\}. \tag{1.21}$$

They perform *gauge-preserving* translations by a distance $\mathbf{R}$ in the presence of a uniform magnetic field. The properties of the operators (1.21) are thoroughly discussed in the following Chapter 2. For the present purposes it suffices to observe that they are constructed so as to commute with the free-particle Hamiltonian (1.20) and thus can be used to classify its states.

The new coordinates and their respective momenta are introduced according to

$$\begin{aligned} \xi &= p_y + x/2, \quad p_\xi = p_x - y/2, \\ \eta &= -p_y + x/2, \quad p_\eta = p_x + y/2, \end{aligned} \tag{1.22}$$

with the inverse transformation given by

$$\begin{aligned} x &= \xi + \eta, \quad p_x = p_\eta - p_\xi, \\ y &= (p_\xi + p_\eta)/2, \quad p_y = (\xi - \eta)/2. \end{aligned} \tag{1.23}$$

One can easily see that the definitions of the new variables directly follow the terms in Eqs. (1.20) and (1.21) at the same time obeying the usual canonical commutation relations

$$[\xi, p_\xi] = [\eta, p_\eta] = i, \quad [\xi, \eta] = [p_\xi, p_\eta] = [\xi, p_\eta] = [\eta, p_\xi] = 0. \tag{1.24}$$

A straightforward calculation leads to the following expressions of the transformed operators

$$\begin{aligned} H_0 &= (p_\xi^2 + \xi^2)/2, \\ T_M(\mathbf{R}) &= \exp[-iR_x p_\eta + iR_y \eta], \end{aligned} \tag{1.25}$$

and explains the point of using them. The ξ degree of freedom corresponds to the effectively one-dimensional motion quantized into the Landau levels. Thus, the transformed Hamiltonian (1.25) has turned into the harmonic oscillator Hamiltonian in ξ and is solved by the corresponding oscillator functions $\chi_n(\xi)$. The dependence on η enters only the expression of $T_M(\mathbf{R})$. Therefore, the

η coordinate can be interpreted as describing the placement of the centroid of the harmonic oscillator wave-function, and thus accounts for the extensive (proportional to the system area) degeneracy of the Landau levels.

Working in the canonical coordinates ξ and η, the electronic states in the n-th Landau level are given by a product of the n-th harmonic oscillator wave-function of ξ and *any* function of η. On the other hand, looking for a *complete set* of the solutions one has to construct a complete basis function set for the η degree of freedom. This is the topic of the two following Sections 1.5 and 1.6.

The conversion of a state $|\psi\rangle$ between the xy- and $\xi\eta$-representations is accomplished by using

$$\langle xy|\psi\rangle = \int d\xi \int d\eta \, \langle xy|\xi\eta\rangle\langle\xi\eta|\psi\rangle \tag{1.26}$$

with the transformation kernel

$$\langle xy|\xi\eta\rangle = \frac{1}{\sqrt{2\pi}} \mathrm{e}^{iy(\xi-\eta)/2} \delta(x-\xi-\eta), \tag{1.27}$$

determined from the eigenvalue equations

$$\begin{aligned} (\hat{\xi}-\xi)|\xi\eta\rangle = 0, \quad \left(\frac{x}{2} - i\frac{\partial}{\partial y} - \xi\right)\langle xy|\xi\eta\rangle &= 0, \\ (\hat{\eta}-\eta)|\xi\eta\rangle = 0, \quad \left(\frac{x}{2} + i\frac{\partial}{\partial y} - \eta\right)\langle xy|\xi\eta\rangle &= 0. \end{aligned} \tag{1.28}$$

1.5 Sample η basis sets

In order to become more comfortable with the strange coordinates ξ and η let us try constructing some simple basis function sets for the η degree of freedom and transforming them into the usual x and y coordinates.

If we choose, for example, a complete orthonormal set of η-dependent functions $\varphi_k(\eta) = \delta(\eta + k)$, the complete set of solutions to the Hamiltonian (1.25) will be given by the functions

$$\psi_{nk}(\xi\eta) = \chi_n(\xi)\delta(\eta + k). \tag{1.29}$$

Transforming (1.29) into the xy-dependence by means of Eq. (1.27) we obtain

$$\psi_{nk}(xy) = \mathrm{e}^{ixy/2} \cdot \frac{1}{\sqrt{2\pi}} \mathrm{e}^{iky} \chi_n(x+k). \tag{1.30}$$

The answer is just the usual solution to the problem in the Landau gauge (1.11) transformed into the symmetric gauge be the exponential prefactor $\exp(ixy/2)$.

Alternatively, one could introduce the plane wave basis and write

$$\psi_{nk}(\xi\eta) = \frac{1}{\sqrt{2\pi}} \mathrm{e}^{ik\eta} \chi_n(\xi). \tag{1.31}$$

Then the transformation into the real space using (1.27) yields (up to an insignificant overall phase)

$$\psi_{nk}(xy) = \mathrm{e}^{-ixy/2} \cdot \frac{1}{\sqrt{2\pi}} \mathrm{e}^{ikx} \chi_n(k-y), \tag{1.32}$$

which is exactly the same as (1.30) written in the coordinate frame rotated by $\pi/2$, i. e. the coordinate axes relabelled according to $x \to -y$, $y \to x$.

What if we tried to use the harmonic oscillator functions as the complete orthonormal basis for both ξ and η thus writing the solutions as

$$\psi_{st}(\xi\eta) = \chi_s(\xi)\chi_t(\eta). \tag{1.33}$$

To answer this question one simply has to note that the angular momentum operator

$$l_z = -i\partial/\partial\phi = xp_y - yp_x \tag{1.34}$$

translated into the $\xi\eta$-language turns into a difference of the harmonic-oscillator Hamiltonians for the two degrees of freedom

$$l_z = \frac{1}{2}(p_\xi^2 + \xi^2) - \frac{1}{2}(p_\eta^2 + \eta^2). \tag{1.35}$$

Therefore, the function (1.33) evidently is an eigenfunction to the Hamiltonian (1.25) with the Landau level number $n = s$ and the angular momentum operator with the quantum number $m = s - t$. Relabelling the indices, we argue that

$$\psi_{nm}(\xi\eta) = \chi_n(\xi)\chi_{n-m}(\eta) \tag{1.36}$$

is an eigenfunction of both the Hamiltonian (1.25) and the angular momentum operator (1.34), and consequently, when transformed into the xy dependence should coincide (up to a phase factor) with the usual symmetric-gauge solution with the Landau level index n and the angular momentum m (1.17).

Evaluating the transformation integral (1.26) for this choice of electron state we obtain a valuable formula which is used for the analytic evaluation of the

overlap integrals involving two displaced harmonic oscillator functions and a plane wave

$$\mathrm{e}^{-ixy/2}\int d\xi\,\chi_n(\xi)\,\mathrm{e}^{i\xi y}\chi_{n-m}(\xi-x) = \int d\xi\,\chi_n(\xi+x/2)\,\mathrm{e}^{i\xi y}\chi_{n-m}(\xi-x/2)$$
$$= \sqrt{\frac{(n-m)!}{2^m n!}}\mathrm{e}^{-(x^2+y^2)/4}(x+iy)^m L_n^m\left(\frac{x^2+y^2}{2}\right) \quad (1.37)$$

Still another complete orthonormal basis of η-dependent functions describing delocalized electronic states is given by the eigenfunctions of the magnetic translation operators. These functions were used for the most of the thesis work, and reviewed in the following Chapter 2. This approach to the bandstructure problem basing on this basis essentially parallels that of plane-wave basis approach to the ordinary bandstructure problem with the necessary modifications introduced to account for the influence of strong magnetic fields.

The construction of a localized basis is the topic of the next Section 1.6.

1.6 Coherent states

The idea to use the coherent-state wave-functions to describe the η degree of freedom deserves a special attention.

Let us start by defining the usual lowering and raising operators

$$\hat{a} = \frac{1}{\sqrt{2}}(\eta + ip_\eta), \quad \hat{a}^\dagger = \frac{1}{\sqrt{2}}(\eta - ip_\eta). \quad (1.38)$$

These operators, acting on the harmonic-oscillator functions $\chi_s(\eta)$, produce the (unnormalized) states of index $s \pm 1$. As it is well known, the operator $\hat{a}^\dagger$ has no eigenfunctions at all, while the eigenvalue problem of the operator $\hat{a}$

$$\hat{a}|\alpha\rangle = \alpha|\alpha\rangle \quad (1.39)$$

has a solution for any complex number α which we use to label the corresponding eigenstates $|\alpha\rangle$. These states are commonly known as the *coherent states* and have been extensively used in many branches of quantum physics. A convenient way to generate the coherent state $|\alpha\rangle$ of arbitrary index α is provided by the displacement (also known as shift) operator

$$\begin{aligned}\hat{D}(\alpha) &= \exp[\alpha\hat{a}^\dagger - \alpha^*\hat{a}],\\ |\alpha\rangle &= \hat{D}(\alpha)|0\rangle.\end{aligned} \quad (1.40)$$

We note that the 'central' coherent state $|0\rangle$ used in (1.40) to produce all the others is nothing else but the ground state of the harmonic oscillator $\langle\eta|0\rangle = \chi_0(\eta)$.

The set of all states $|\alpha\rangle$ is enormously overcomplete, however, the overcompleteness problem can be solved by restricting the allowed values of α to a discrete set defined on a lattice in the complex-plane

$$\alpha_{\mu\nu} = \frac{1}{\sqrt{2}}\left(\mu b + i\nu\frac{2\pi}{b}\right), \tag{1.41}$$

here μ and ν are integer indices and b is a real number setting the lattice spacing along the real axis. The spacing along the imaginary axis equals $2\pi/b$ so that the unit cell area is 2π. The defined basis $|\alpha_{\mu\nu}\rangle$ is still slightly overcomplete, and in order to get rid of this problem one has to exclude one them from the set, However, we will not enter the discussion of this intriguing issue here.

Thus, we suggest to consider the following set of solutions to the Hamiltonian (1.25)

$$\psi_{n,\mu\nu}(\xi\eta) = \chi_n(\xi)\langle\eta|\alpha_{\mu\nu}\rangle = \hat{D}(\alpha_{\mu\nu})\chi_n(\xi)\chi_0(\eta), \tag{1.42}$$

here we use the displacement operator to generate the states $|\alpha_{\mu\nu}\rangle$. A straightforward calculation using (1.38) and (1.40) gives the following η-representation of the displacement operator

$$\hat{D}(\alpha_{\mu\nu}) = \exp\left[-i\mu b p_\eta + i\nu\frac{2\pi}{b}\eta\right]. \tag{1.43}$$

Comparing this result to the definition of the magnetic translation operator (1.25) we conclude that

$$\hat{D}(\alpha_{\mu\nu}) \equiv T_M(\mathbf{R}_{\mu\nu}), \quad \mathbf{R}_{\mu\nu} = \mu b\hat{e}_x + \nu\frac{2\pi}{b}\hat{e}_y, \tag{1.44}$$

and the basis (1.42) becomes

$$\psi_{n,\mu\nu}(\xi\eta) = T_M(\mathbf{R}_{\mu\nu})\chi_n(\xi)\chi_0(\eta). \tag{1.45}$$

The transformation of (1.45) from ξ, η into the x, y (or rather the polar ρ, ϕ) coordinates gives the result

$$\psi_{n,\mu\nu}(\rho,\phi) = T_M(\mathbf{R}_{\mu\nu})F_n(\rho,\phi), \tag{1.46}$$

which is evident from the fact that $\chi_n(\xi)\chi_0(\eta)$ is the state of the n-th Landau level with the angular momentum $m = n$. Here F_n is the maximum-angular-momentum function introduced in Eq. (1.19) Section 1.3.

Thus we succeeded in constructing a complete set of localized basis functions. It is obtained by magnetotranslating the symmetric gauge solutions with angular momentum $m = n$ (there will be one representative function for each Landau level) onto a two-dimensional lattice spanned by the vectors (1.44). The condition that the unit-cell area equal 2π (in our dimensionless units) actually means that the flux penetrating it is exactly one flux quantum.

The constructed basis functions (1.46) are nicely localized; remember that the coherent states are in fact the minimum uncertainty wave-packets. However, they are not mutually orthogonal. The underlying reason is rather deep – localization and orthogonality are incompatible in magnetic fields. Thus, any attempt to orthogonalize the functions (1.46) would result in poor localization properties, namely the $1/r$ asymptotic behaviour in one of the two lateral directions.

CHAPTER 2

Magnetic Translations

2.1 Translational symmetry

One of the possible approaches to symmetry transformations in physics – the one that we use in the following discussion – relies on the so-called "active" point of view. According to this convention, the transformations are visualized as affecting the actual physical system. For example, an application of a translation by a given distance vector $\mathbf{R}$ means that an electron whose wave function was centered around a certain point in space $\mathbf{r}_0$, after the translation has ended up in the vicinity of the point $\mathbf{r}_0 + \mathbf{R}$. Introducing the corresponding translation operator $T(\mathbf{R})$ acting in the Hilbert space of electronic states we arrive at the following relation for the transformation of the states induced by the translation

$$\psi'(\mathbf{r}) \equiv T(\mathbf{R})\psi(\mathbf{r}) = \psi(\mathbf{r} - \mathbf{R}). \tag{2.1}$$

Using this result and the formal representation of the Taylor expansion

$$f(x_0 + \Delta x) = \sum_{n=0}^{\infty} \frac{(\Delta x)^n}{n!} \left.\frac{\partial^n}{\partial x^n} f(x)\right|_{x=x_0} = \exp\left(\Delta x \frac{\partial}{\partial x}\right) f(x_0) \tag{2.2}$$

we easily construct the explicit form of the translation operator

$$T(\mathbf{R}) = \exp\left(-\mathbf{R}\frac{\partial}{\partial \mathbf{r}}\right) = \exp\left(-\frac{i}{\hbar}\mathbf{R}\cdot\mathbf{p}\right), \tag{2.3}$$

here $\mathbf{p}$ denotes the canonical momentum operator.

The conventional solid state theory relies on the use of the group of the operators (2.3) to classify the electronic states in a perfect (usually three-dimensional) crystal lattice spanned by the vectors $\mathbf{R} = n_1\mathbf{a}_1 + n_2\mathbf{a}_2 + n_3\mathbf{a}_3$, with n_i being

integer indices and $\mathbf{a}_i$ denoting the three elementary lattice vectors. The translation operators (2.3) mutually commute thus defining an Abelian group. Its irreducible representations

$$D^{\mathbf{q}}(\mathbf{R}) = \mathrm{e}^{-i\mathbf{q}\cdot\mathbf{R}} \tag{2.4}$$

are labelled by a vector $\mathbf{q}$, the crystal momentum, whose allowed values are restricted to a unit cell of the reciprocal lattice spanned by the vectors $\mathbf{G}$ such that $\mathbf{G}\cdot\mathbf{R} = 2\pi \times$ integer. A common approach to the problem of calculation of the electronic states in a crystal uses the planes waves as the basis functions. Clearly, the functions

$$\psi_{\mathbf{G}}(\mathbf{q}|\mathbf{r}) = \exp[i(\mathbf{q}+\mathbf{G})\cdot\mathbf{r}] \tag{2.5}$$

with a given $\mathbf{q}$ and all possible vectors $\mathbf{G}$ have identical transformation properties under the discrete translations by any lattice vector $\mathbf{R}$. It is said that they all belong to the same irreducible representation $\mathbf{q}$. Any potential periodic on the lattice $\mathbf{R}$ can mix the functions (2.5) between themselves but not with the functions belonging to different irreducible representations. The acknowledgement of this fact greatly reduces the effort needed to calculate the energies and wave-functions of electronic states in a complicated crystal potential.

The above description applies to the case when there is no magnetic field or, at least, its influence can be safely ignored from the beginning and taken into account later as a perturbation. Such an approach is perfectly justified in the electronic structure calculations of ordinary solids. The typical energies of magnetic interactions are negligible on the scale of atomic energy levels, and the typical magnetic fluxes penetrating a unit cell are never comparable to the magnetic flux quantum. However, in artificially created lateral superlattices the lattice constants can be sufficiently large thus bringing us into the regime where the applied magnetic fields will essentially modify the mathematical description of the symmetry with respect to discrete translations by a lattice vector. This is the topic of the following Sections.

2.2 Magnetic translation operators

We will consider a two-dimensional lattice spanned by the set of vectors $\mathbf{R} = n_1\mathbf{a}_1 + n_2\mathbf{a}_2$, where $\mathbf{a}_{1,2}$ again denote the unit vectors, and $n_{1,2}$ are integer indices. However, our lattice is placed into a perpendicular (to begin with) magnetic field whose effects can not be neglected. The Hamiltonian to be considered is given by

$$H = \frac{1}{2m}\left(\mathbf{p} + \frac{e}{c}\mathbf{A}\right)^2 + v(\mathbf{r}), \quad v(\mathbf{r}) = v(\mathbf{r}+\mathbf{R}). \tag{2.6}$$

While the physical system described by (2.6) *is* invariant with respect to discrete translations by a lattice vector $\mathbf{R}$, the Hamiltonian itself apparently *is not*. The vector potential in the kinetic energy term introduces an additional localizing potential well through the term $\propto \mathbf{A}^2$. What went wrong?

The answer is that the Hamiltonian (2.6) is still translationally invariant, however, only up to a gauge transformation. Obviously, an attempt to apply the usual translation operator (2.3) to (2.6) would shift not only the scalar potential term $v(\mathbf{r})$ but also the vector potential $\mathbf{A}(\mathbf{r})$. The shifted vector potential has the same curl as the original one and, therefore, describes the same magnetic field $\mathbf{B}$, however, the invariance of the mathematical form is gone.

The situation is rectified by replacing the usual translations (2.3) with the *magnetic* translation operators $T_M(\mathbf{R})$ which actually consist of an ordinary translation (2.3) followed by the necessary gauge transformation needed to restore the required invariance of the kinetic energy term. From another point of view, the magnetic translators can by defined by demanding that they commute with the kinetic energy operator.

Maintaining a certain degree of similarity to the ordinary translations we write the magnetic translation operator in the form

$$T(\mathbf{R}) = \exp\left(-\frac{i}{\hbar}\mathbf{R}\cdot\mathbf{p}_{\mathrm{gen}}\right), \quad \mathbf{p}_{\mathrm{gen}} = \mathbf{p} + \frac{e}{c}\mathbf{f}, \tag{2.7}$$

where $\mathbf{p}_{\mathrm{gen}}$ is the generator of translations in a magnetic field. We present it as a sum of the canonical momentum (the generator of ordinary translations) and a complementary field $(e/c)\mathbf{f}(\mathbf{r})$ responsible for the additional gauge transformation. The function $\mathbf{f}$ has to be determined from the commutation relations

$$[\mathbf{p}_{\mathrm{kin}}, \mathbf{p}_{\mathrm{gen}}] = \left[\mathbf{p} + \frac{e}{c}\mathbf{A}, \mathbf{p} + \frac{e}{c}\mathbf{f}\right]. \tag{2.8}$$

Note that this equation is a tensorial one – we have to consider the commutation of all components of the involved vectors; thus, in this sense the kinetic momentum $\mathbf{p}_{\mathrm{kin}}$ does not commute with itself. The equation (2.8) directly implies that $\operatorname{div}\mathbf{f} = 0$ and $\operatorname{curl}\mathbf{f} = -\mathbf{B}$, thus the vector field $-\mathbf{f}$ qualifies as a vector potential of the magnetic field $\mathbf{B}$ in some gauge. The actual components of $\mathbf{f}$ are dependent on the chosen gauge and in each particular case have to be deduced from Eq. (2.8). In the symmetric gauge we find $\mathbf{f} = -\mathbf{A}$, while the use of the Landau gauge with $A_y = Bx$ will lead to $f_x = -By$. Most of the time we work in the symmetric gauge which is convenient for its particular notational simplicity.

When the magnetic field also has an *in-plane* component $\mathbf{B}^{\parallel}$, we find it convenient to describe it in a Landau gauge using z-dependent x and y components

of the corresponding vector potential $A_y^{\parallel} = -B_x^{\parallel} z$ and $A_x^{\parallel} = B_y^{\parallel} z$. Following this choice, we are able to maintain the in-plane components of the $\mathbf{f}$ field unmodified, and isolate the effects of the parallel field $\mathbf{B}^{\parallel}$ on the magnetic translations into the z-component $f_z = -B_x^{\parallel} y + B_y^{\parallel} x$. This modification will manifest itself as the momentum shift of an electron tunneling out of the two-dimensional plane.

2.3 **Properties of magnetic translations**

Concentrating to the symmetric gauge we write the magnetic translations as

$$T_M(\mathbf{R}) = \exp\left[-\frac{i}{\hbar}\mathbf{R}\cdot\left(\mathbf{p} - \frac{e}{c}\mathbf{A}\right)\right], \tag{2.9}$$

and determine the effect on a given wave-function

$$T_M(\mathbf{R})\psi(\mathbf{r}) = \exp\left[\frac{ie}{2\hbar c}\mathbf{r}\cdot(\mathbf{R}\times\mathbf{B})\right]\psi(\mathbf{r}-\mathbf{R}), \tag{2.10}$$

which is indeed a simple translation followed by a gauge-transformation. Using the property of exponentiated operators

$$\begin{aligned} &\mathrm{e}^{A}\mathrm{e}^{B}\mathrm{e}^{-[A,B]/2} = \mathrm{e}^{A+B} = \mathrm{e}^{B}\mathrm{e}^{A}\mathrm{e}^{[A,B]/2} \\ &\text{provided} \quad [A,[A,B]] = [B,[A,B]] = 0 \end{aligned}$$

we calculate the product of two magnetic translators and find

$$\begin{aligned} T_M(\mathbf{R}_1)T_M(\mathbf{R}_2) &= \exp\left[-\frac{ie}{2\hbar c}\mathbf{B}\cdot(\mathbf{R}_1\times\mathbf{R}_2)\right]T_M(\mathbf{R}_1+\mathbf{R}_2) \\ &= \exp\left[-\frac{ie}{\hbar c}\mathbf{B}\cdot(\mathbf{R}_1\times\mathbf{R}_2)\right]T_M(\mathbf{R}_2)T_M(\mathbf{R}_1). \end{aligned} \tag{2.11}$$

We see that a product of two such operators generally equals another operator only up to a phase. Therefore, the group of magnetic translation operators is a *ray* group rather than a conventional vector group. Moreover, the operators (2.9), unlike the ordinary translations, generally do not commute. It is easy to see that the triple product $\mathbf{B}\cdot(\mathbf{R}_1\times\mathbf{R}_2)$ entering Eq. (2.11) equals the magnetic flux penetrating the cell built on the vectors $\mathbf{R}_1$ and $\mathbf{R}_2$. Recalling the expression for the flux quantum $\Phi_0 = ch/e$, we arrive at the conclusion that the magnetotranslation group is Abelian only when the magnetic flux penetrating a unit cell is an integer multiple of Φ_0.

2.4 Group theory

Despite the fact that we deal with a ray group the conventional apparatus of the group theory remains to be applicable. Closely following the analogous developments for ordinary vector groups, one can prove the possibility to work with a unitary representation and the Shur lemmas. These results open the path to the orthogonality relations and the construction of the projection operators which can be used to derive the symmetry-adapted basis consisting of functions transforming according to the irreducible representations of the group. Since this line of thought is developed in the papers in sufficient detail we do not continue it here.

It is appropriate to mention, however, that as anticipated, the irreducible representations and the constructed symmetry-adapted basis functions are sensitive to the ratio of the magnetic flux penetrating a unit lattice cell to the magnetic flux quantum

$$\frac{\Phi}{\Phi_0} = \frac{L}{N}, \quad L, N \in \mathcal{Z}, \tag{2.12}$$

which has to be a rational number. The irreducible representations are labelled by a *magnetic crystal momentum* $\mathbf{q}$ restricted to a single *magnetic Brillouin zone* (MBZ), or to a $1/N \times 1/N$ part of it if $N \neq 1$. The $\mathbf{q}$-th irreducible representation is still related to the 'central' $\mathbf{q} = 0$ one by a familiar relation

$$D^{\mathbf{q}}(\mathbf{R}) = D^0(\mathbf{R})\, \mathrm{e}^{-i\mathbf{q}\cdot\mathbf{R}}. \tag{2.13}$$

However, at this point the close similarity to the group of ordinary translations ends. The irreducible representation matrices are N-dimensional, thus implying the existence of N partner functions. Moreover, there exist L distinct functions transforming according to the same row of the same irreducible representation. These facts indicate that at the dimensionless magnetic flux value L/N the Landau bands will split into L subbands, each of them being N times degenerate. In view of the fact that the size of MBZ also shrinks N^2 times we conclude that the total number of states in a Landau level or a Landau band follows the variations of the magnetic field strength as $\sim L \times N \times 1/N^2 \sim L/N$, i. e. proportionally to the magnetic field strength, as expected.

2.5 Special case: the kq-function

In order to get acquainted with the properties of the basis functions of the group of magnetic translations, we will consider now a special case of $L = N = 1$, i. e. when there is exactly one flux quantum penetrating a unit lattice cell. In this

way, we will be able to concentrate on the properties of the basis functions and distance ourselves from the complications introduced by commensurability which is the topic of the following Chapter 3. Quite interestingly, in just a few pages we will be able to touch the fundamentals of quantum mechanics and rediscover the quantum Hall effect.

In the dimensionless units, the condition $\Phi = \Phi_0$ translates into the requirement that the unit cell area equal 2π. In accordance with this, we consider a rectangular lattice of period a in the x-direction and $2\pi/a$ along y. The group of magnetic translations is now Abelian and thus we need to find the simultaneous eigenfunctions of the two elementary translations along the two axes. Working in the canonical coordinates ξ and η (1.22), we deduce from Eq. (1.25) that

$$\begin{aligned} T_M(a_x) &= \exp\left(-iap_\eta\right), \\ T_M(a_y) &= \exp\left(i\frac{2\pi}{a}\eta\right). \end{aligned} \tag{2.14}$$

The first of the operators (2.14) is an ordinary translation in η, while the second one can be interpreted as a translation in the momentum space. Indeed, in the momentum representation $\eta \to i\partial/\partial p_\eta$, and thus

$$T_M(a_y) = \exp\left(-\frac{2\pi}{a}\frac{\partial}{\partial p_\eta}\right). \tag{2.15}$$

The common eigenfunction of the two operators (2.14) is known under the name of the kq-function. Let us see how this function is constructed. Consider a complete basis set for the η degree of freedom given by $\psi_{\eta_0} = \delta(\eta - \eta_0)$. Each of these functions describes a localized state centered at some given η_0 assuming its values from $-\infty$ to ∞. Let us divide the η axis into cells of length a and agree to specify the position η_0 by naming the number of the cell n and the location within this cell ($0 \le q < a$) so that

$$\eta_0 = na - q. \tag{2.16}$$

Then the basis function of the complete set will be labelled by two indices, a discrete and a continuous one,

$$\psi_{nq}(\eta) = \delta(\eta + q - na), \tag{2.17}$$

At the next step, in a fashion similar to the construction of a Bloch wave from atomic orbitals, we perform a unitary transformation from the discrete 'atomic

site' number n to a continuous Bloch index k restricted to $0 \leq k < 2\pi/a$, and obtain the normalized kq-function as

$$\psi_{kq}(\eta) = \sqrt{\frac{a}{2\pi}} \sum_{n=-\infty}^{\infty} \mathrm{e}^{iknq} \delta(\eta + q - na). \tag{2.18}$$

It is easy to check that the function (2.18) is an eigenfunction of the operators (2.14)

$$\begin{aligned} T_M(a_x)\psi_{kq}(\eta) &= \mathrm{e}^{-ika}\psi_{kq}(\eta), \\ T_M(a_y)\psi_{kq}(\eta) &= \mathrm{e}^{-i(2\pi/a)q}\psi_{kq}(\eta). \end{aligned} \tag{2.19}$$

The two-dimensional vector with the components k and q actually plays the role of the *magnetic crystal momentum*, and the area covered by the allowed values $0 \leq k < 2\pi/a$, $0 \leq q < a$ defines the *magnetic Brillouin zone* for this special case.

2.6 kq-representation

As we all know from the elementary quantum mechanics, for a one-dimensional problem it is sufficient to have one operator in order to define a representation. Two common choices of such an operator are the momentum p and the coordinate x operators. Both of them can be used to classify the electronic states uniquely, while the simultaneous specification of both the coordinate and the momentum is impossible.

The momentum operator is the generator of translations in the real space; it commutes with the Hamiltonian of a free particle and thus makes a suitable choice for the classification of its eigenstates. The eigenvalues of the momentum operator assume all real values from $-\infty$ to ∞. Now, let us suppose that we introduce a periodic potential of a lattice constant a. The correspondingly modified Hamiltonian will not commute with the momentum operator p any longer, however, it will still commute with the exponentiated momentum operator $\exp(-iap)$ which is nothing else but a discrete translation by a lattice constant a. This commutation expresses the surviving invariance with respect to a set of discrete translations, therefore, the exponentiated momentum operator can still be used to classify the eigenstates. The corresponding quantum number k introduced by

$$\exp(-iap)\,\psi(x) = \exp(-iak)\,\psi(x) \tag{2.20}$$

is usually referred to as quasimomentum, and assumes all real values restricted to an interval of the length $2\pi/a$. However, the specification of the quasimomentum quantum number alone does not determine the quantum mechanical state completely. An additional index is needed, and the role of this extra index is usually played by the band number. Alternatively, if we choose to present the energy bands in the extended scheme by drawing each band in a different Brillouin zone, the Brillouin zone number will become this extra index. In other words, by specifying the quasimomentum quantum number alone we determine the exact location of an electronic state within a Brillouin zone only up to a discrete translation into another Brillouin zone.

Exploiting the duality of coordinates and momenta, we can introduce the quasicoordinate quantum number q in a very similar fashion by specifying the exact location of a quantum mechanical state within a unit lattice cell in the real space. Then an extra integer index, namely the cell number, would still be needed for the complete description. This is what we actually did in the previous Section 2.5 arriving at Eq. (2.16).

As a matter of fact, the quantum numbers q and k introduced in the construction of the kq-function (2.18) in Sec. 2.5 play the role of the quasicoordinate and the quasimomentum, respectively, in the one-dimensional η space. Moreover, by constructing the kq-function we proved that besides the commonplace coordinate and momentum representations it is possible to define an alternative representation – for the absence of a better name – the kq-representation. This means that it is possible to define quantum-mechanical states that have both the coordinate and the momentum quantum numbers specified simultaneously, however, only up to a discrete translation in the real and reciprocal space, respectively.

The description of an electron motion in a perpendicular magnetic field is an example of a practical application of the kq-representation. The two components of magnetic crystal momentum $\mathbf{q}$ are the quasicoordinate and the quasimomentum corresponding to the one-dimensional space of the generalized coordinate η.

2.7 Topology of MBZ

In the previous Sections, we defined the *magnetic* translation operators as the proper generalization of the ordinary translations for the case of strong magnetic fields, and introduced the *magnetic* Brillouin zone (MBZ) as the corresponding generalization of the ordinary one. The wave-functions defined in MBZ have some interesting topological properties which we will now consider.

It is well known from the ordinary (non-magnetic) solid state theory that the electronic states are perfectly periodic in the reciprocal space. This means that a state defined on a point on one boundary of the BZ is completely identical to the state belonging to the point on the opposite boundary differing from the first one by a reciprocal lattice vector.

The corresponding situation in the case of MBZ is essentially different. From the expression of the kq-function (2.18), which describes the states in MBZ for the special case $\Phi = \Phi_0$, we deduce that

$$\begin{aligned} k \to k + \frac{2\pi}{a} \qquad & \text{leads to} \qquad \psi_{kq} \to \psi_{kq}, \\ q \to q + a \qquad & \text{leads to} \qquad \psi_{kq} \to \mathrm{e}^{ika}\psi_{kq}. \end{aligned} \tag{2.21}$$

Thus, the states on the opposite edges of MBZ in the k direction are identical, while the states located on the opposite edges along the q directions differ by a k-dependent phase factor. Traveling around the boundary of MBZ and keeping track of the phase of the wave-function one will find a winding number equal to one, i. e. the phase makes one complete cycle from 0 to 2π. Of course, the phases of the wave-functions can be modified by a gauge transformation at each point of MBZ individually, however, the winding number is a topological quantity and will persist. In other words, this means that MBZ, which is topologically a torus, must contain a cut with the phases of the wave-functions changing discontinuously when crossing the cut. By necessity, the total change of the phase accumulated while traveling around the cut and returning to the original point can only equal an integer multiple of 2π.

As a matter of fact, this integer can be proven to be the quantum Hall conductance integer. The above considered electronic states in MBZ represent the states in a Landau level perturbed by a periodic potential whose unit lattice cell is penetrated by a single flux quantum. On the other hand, the electronic states defined in MBZ can also represent the states in an *unperturbed* Landau level classified by their translational properties with respect to an *empty* lattice. Therefore, the foregoing analysis and the conclusion that the quantum Hall integer equals unity actually applies to Landau levels. Indeed, each filled Landau level contributes one conductance quantum to the total Hall conductance of a two-dimensional electron system. On the other hand, the quantum Hall conductance an ordinary Bloch band living in the ordinary (non-magnetic) Brillouin zone is, obviously, zero.

By applying an actual periodic potential modulation on a lattice whose unit cell is penetrated by an arbitrary rational flux, the Landau level is split into an intricate pattern of subbands. Each individual subband may be characterized

by an arbitrary (integer) winding number and thus carry an arbitrary quantized quantum Hall current. However, the net contribution of all subbands within any Landau band will still add up to 1.

CHAPTER 3

Commensurability

Moving in parallel to the general approach of the solid state theory to the electronic structure problem, we discuss the two complementary limiting cases pertaining to the motion of a two-dimensional electron in a periodic potential and a perpendicular magnetic field. The two complementary limits are, of course, the tight-binding approximation and a nearly-free electron modl. Both physical approaches lead to a very similar (actually the same) mathematical description which in a transparent way introduces us to the key concept of *commensurability*. In the present case, by this word we refer to the sensitivity of the energy spectrum of the electron to the ratio of the magnetic flux quantum penetrating a unit lattice cell and the fundamental magnetic flux quantum.

3.1 Tight-binding model

We consider a two-dimensional square lattice (see Figure 3.1) of atomic sites labelled by a set of two integers m and n, in the x and y directions, respectively. Placing a single atomic orbital $|m,n\rangle$ of energy ε_0 on each lattice site, and introducing identical nearest-neighbour hopping matrix elements $t > 0$ we construct the following tight-binding Hamiltonian

$$\begin{aligned} H &= \varepsilon_0 \sum_{mn} c^\dagger_{m,n} c_{m,n} - t \sum_{mn} \Big\{ c^\dagger_{m+1,n} c_{m,n} \\ &+ c^\dagger_{m-1,n} c_{m,n} + c^\dagger_{m,n+1} c_{m,n} + c^\dagger_{m,n-1} c_{m,n} \Big\} . \end{aligned} \tag{3.1}$$

Here $c^\dagger_{m,n}$ and $c_{m,n}$, respectively, are the creation and destruction operators associated with the state $|m,n\rangle$. In the following we use t as the energy unit and adjust the origin of the energy scale origin so that $\varepsilon_0 = 0$. In the absence of a perpendicular magnetic field, the solution of the Hamiltonian (3.1) leads the usual cosine band whose width equals to 4.

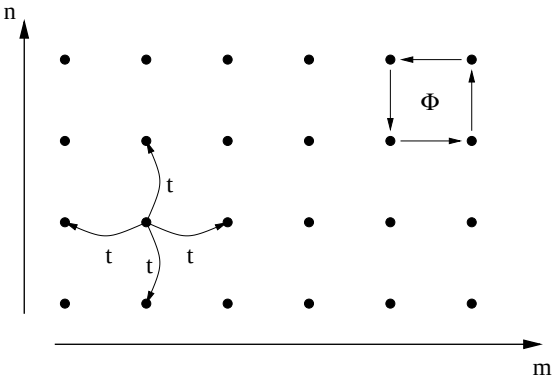

Figure 3.1: A two-dimensional lattice. The nearest-neighbour sites are connected by hopping matrix elements t. In the presence of a magnetic field the "vertical" transitions will be modified by an m-dependent phase.

We include the effects of the perpendicular magnetic field only insofar as the modification of the phase of the hopping matrix elements is concerned, and neglect its localizing effects which would lead to the band narrowing. Thus, working in the Landau gauge we introduce the vector potential according to $A_y = Bx$, and multiply the matrix element describing the hopping in the positive direction of the n axis by an m-dependent phase factor $\exp(-i2\pi\varphi m)$. Tunneling in the opposite direction is, naturally, modified by a phase of the opposite sign, while the hopping in the perpendicular direction is not affected at all. The meaning of the parameter φ is clear from the consideration of the phase acquired by an electron moving along around the unit lattice cell in the counter-clockwise direction. This phase is $-2\pi\varphi$, therefore, φ can be identified with the dimensionless magnetic flux penetrating an elementary cell $\varphi = \Phi/\Phi_0$.

Thus the Hamiltonian under consideration becomes

$$\begin{aligned} H = \; & - \sum_{mn} \Big\{ c^\dagger_{m+1,n} c_{m,n} + c^\dagger_{m-1,n} c_{m,n} \\ & + \; \mathrm{e}^{-i2\pi\varphi m} c^\dagger_{m,n+1} c_{m,n} + \mathrm{e}^{i2\pi\varphi m} c^\dagger_{m,n-1} c_{m,n} \Big\} . \end{aligned} \tag{3.2}$$

We expand the electronic states in the atomic orbitals

$$|\psi\rangle = \sum_{mn} \psi_{mn} |m,n\rangle, \tag{3.3}$$

then the eigenvalue equation $H|\psi\rangle = \varepsilon|\psi\rangle$ leads to the following relation between the expansion coefficients

$$\varepsilon\psi_{mn} = - \left[\psi_{m+1,n} + \psi_{m-1,n} + \mathrm{e}^{i2\pi\varphi m} \psi_{m,n+1} + \mathrm{e}^{-i2\pi\varphi m} \psi_{m,n-1} \right] . \tag{3.4}$$

Since the numerical coefficients in (3.4) depend only on m but not on n we can use an Ansatz based on the plane-wave solutions along the n direction

$$\psi_{mn} = \mathrm{e}^{i2\pi kn}\psi_m, \quad 0 \le k < 1. \tag{3.5}$$

Substituting (3.5) into the difference equation (3.4) we arrive at the relation for the expansion coefficients ψ_m

$$\varepsilon\psi_m = -\left[\psi_{m+1} + \psi_{m-1} + 2\cos(2\pi k + 2\pi\varphi m)\,\psi_m\right]. \tag{3.6}$$

As a matter of fact, Eq. (3.6) describes a one-dimensional tight-binding lattice model with unit nearest-neighbour hopping matrix elements and periodically modulated site energies

$$\varepsilon_0(m) = -2\cos(2\pi k + 2\pi\varphi m). \tag{3.7}$$

The period of this modulation is

$$\Delta m = \frac{1}{\varphi} = \frac{\Phi_0}{\Phi} = \frac{N}{L}, \tag{3.8}$$

here we introduced the rationality condition by expressing the magnetic flux penetrating a unit cell as a rational multiple L/N of the magnetic flux quantum. The integers L and N are mutual primes.

The above analysis shows that the simplest tight-binding model of a two-dimensional electron moving in competing perpendicular magnetic field and a periodic potential can be mapped onto a one-dimensional tight-binding model with two competing periods — the unit spacing of the lattice sites and the modulation period $\Delta m = N/L$. This is the simplest possible model which demonstrates the manifestation of the commensurability related phenomena. The least common integer multiple of 1 and N/L is N, thus, we can join N adjacent lattice cells into larger physically identical supercells which will act as the unit cells of a strictly periodic system. Thus it suffices to solve the difference equation (3.6) in a supercell of N adjacent lattice sites introducing a periodic boundary condition

$$\psi_{m+N} = \mathrm{e}^{i2\pi q}\psi_m, \quad 0 \le q < 1. \tag{3.9}$$

The two introduced parameters $0 \le k, q < 1$ play the role of the components of the magnetic crystal momentum confined to a single MBZ. Using (3.9) the

eigenvalue problem can be represented by a finite $N \times N$ matrix

$$\begin{pmatrix} \varepsilon_0(1) & -1 & \cdots & \cdots & -\mathrm{e}^{-i2\pi q} \\ -1 & \varepsilon_0(2) & -1 & \cdots & 0 \\ \vdots & & & \ddots & \vdots \\ -\mathrm{e}^{i2\pi q} & 0 & \cdots & -1 & \varepsilon_0(N) \end{pmatrix} \tag{3.10}$$

whose eigenvalues specify the energies of the electronic states. Evidently, the resulting energy band originating from a single atomic orbital present in our model and influenced by the commensurate magnetic field will be split into N subbands given by the eigenvalues of the matrix (3.10). We hasten to warn that in this limit of a tight-binding lattice perturbed by the magnetic field the roles of the integers L and N are reversed with respect to those featured in the opposite limit of a Landau level perturbed by a weak periodic potential to be considered in the following Section 3.2.

The spectrum of the eigenvalues of the matrix (3.10) as a function of L/N is displayed in Fig. 3.2. Each black dots corresponds to the energy value of an allowed state, while white areas signify forbidden gaps. The structure of the subbands is rather complicated. At each given rational value of the flux L/N we observe N subbands. When the magnetic flux changes, the denominator N follows a rapidly varying sequence of values, and so does the number of existing subbands. The physical requirement that the subbands evolve continuously as a function of the magnetic flux leads to the clustering of subbands into well defined groups. In panel (b), we display the interval $L/N \in 1/3 \ldots 2/5$ at a larger scale. There are three subbands at $L/N = 1/3$. When the flux value deviates from this simple fraction the subbands proliferate but stay packaged into three clusters. Approaching the flux value $L/N = 2/5$, another simple fraction, we observe the formation of 5 distinct subbands.

3.2 **Weakly perturbed Landau level**

Let us start with perfectly flat Landau levels and write their electronic wavefunctions in the canonical ξ, η coordinates introduced in Eq. (1.22). We choose to work in the basis (1.29)

$$\psi_{n\tilde{k}}(\xi\eta) = \langle \xi\eta | n\tilde{k} \rangle = \chi_n(\xi)\delta(\eta + \tilde{k}), \tag{3.11}$$

and perturb the system with a weak cosine-like potential of a perfect square symmetry

$$v = v_0[\cos(\alpha x) + \cos(\alpha y)] = \frac{v_0}{2}\left(\mathrm{e}^{i\alpha x} + \mathrm{e}^{-i\alpha x} + \mathrm{e}^{i\alpha y} + \mathrm{e}^{-i\alpha y}\right). \tag{3.12}$$

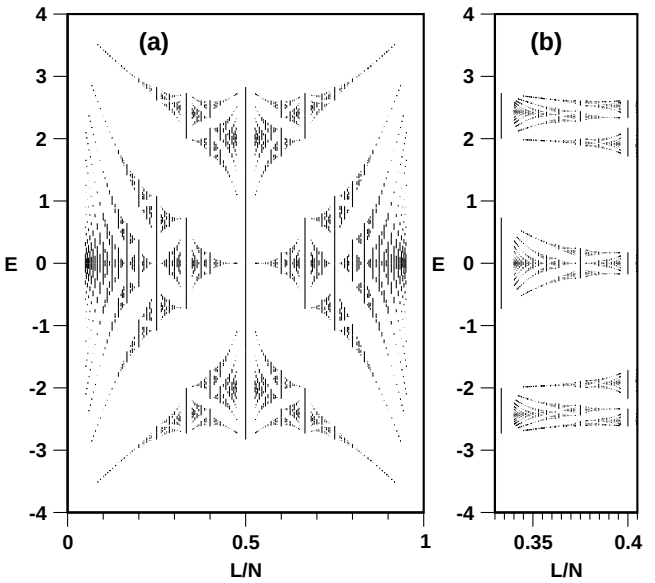

Figure 3.2: The spectrum of an electron in a periodic potential and a commensurate magnetic field L/N. Panel (a) shows the entire spectrum obtained including all values of N up to 20 in combination with all possible L's. Panel (b) displays the fragment of the spectrum $1/3 \leq L/N \leq 2/5$ at a higher resolution obtained by including all possible combinations of L and $N \leq 50$.

The parameter α sets the lattice constant to $a = 2\pi/\alpha$. In view of the fact that in the dimensional units the unit cell area equals 2π times the dimensionless flux we identify

$$\alpha^2 = \frac{2\pi N}{L}. \tag{3.13}$$

We evaluate the matrix elements of the perturbing potential (3.12) between our basis functions assuming that v_0 is sufficiently weak so that the different Landau levels will not be coupled

$$\langle n\tilde{k}|\mathrm{e}^{\pm i\alpha x}|n\tilde{k}'\rangle \quad = \quad \mathrm{e}^{-\alpha^2/4} L_n\left(\frac{\alpha^2}{2}\right) \mathrm{e}^{\mp i\alpha\tilde{k}} \delta(\tilde{k} - \tilde{k}'), \tag{3.14}$$

$$\langle n\tilde{k}|\mathrm{e}^{\pm i\alpha y}|n\tilde{k}'\rangle \quad = \quad \mathrm{e}^{-\alpha^2/4}L_n\left(\frac{\alpha^2}{2}\right)\delta(\tilde{k}-\tilde{k}'\mp\alpha),$$

where L_n is n-th Laguerre polynomial. In evaluating (3.14) we expressed x and y in terms of canonical coordinates (1.22) and used the formula (1.37) derived in Section 1.5. We see, that the periodic perturbation couples only the states whose $\tilde{k}$'s differ by an integer multiple of α. Thus, representing $\tilde{k}$ as

$$\tilde{k} = (k+m)\alpha, \quad 0 \le k < 1,\, m \in \mathcal{Z} \tag{3.15}$$

we express the matrix elements of the perturbation (3.12) as

$$\begin{aligned}\langle nkm|v|nkm'\rangle = \frac{v_0}{2}\mathrm{e}^{-\alpha^2/4}L_n\left(\frac{\alpha^2}{2}\right)\\ \times\left\{\delta_{m,m'+1}+\delta_{m,m'-1}+\delta_{m,m'}2\cos[\alpha^2(k+m)]\right\}.\end{aligned} \tag{3.16}$$

The expression in the curly braces hints again at a one-dimensional tight-binding model with the site energies modulated harmonically with the period

$$\Delta m = \frac{2\pi}{\alpha^2} = \frac{L}{N}. \tag{3.17}$$

Comparing this result to that obtained in the previous Section 3.1, Eq. (3.8) we convince ourselves that the roles of the integers N and L in the formation of the energy spectrum have been reversed. We do not continue the discussion of the internal structure of the Landau levels in the present case for it would very closely parallel that described in the previous Section 3.1. Each Landau band is split into L subbands following the same intricate scheme as that depicted in Fig. 3.2. Instead, we concentrate on the prefactor

$$\mathrm{e}^{-\alpha^2/4}L_n\left(\frac{\alpha^2}{2}\right) = \exp\left(-\frac{\pi N}{2L}\right)L_n\left(\frac{\pi N}{L}\right) \tag{3.18}$$

appearing in Eq. (3.16) which introduces an element of novelty. We see, that due to this prefactor the overall band widths will oscillate in a characteristic manner. In particular, at the zeros of the involved Laguerre polynomial the total band width will be zero. This fact is a manifestation of another type of commensurability. To be more specific, we deal here with the commensurability of the spatial extent of an electronic orbital and the potential modulation period. Obviously, the effect of the perturbing periodic potential on the energy of an electronic state will be determined by its average strength over the extent of

the wave-function. Under the so-called 'flat-band conditions' given by the zeros of the Laguerre polynomial this average is exactly equal to zero. This result, however, is exact only when the periodic potential is of a simple cosine from and we do not take the coupling between different Landau levels into account. The band-width oscillations discussed above manifest themselves in the magnetoresistance measurements where they give rise to the so-called Weiss oscillations in the dependence of the conductance on the magnetic field strength.

References

1. Electrons in a magnetic field:
   (a) R. B. Dingle, Proc. Roy. Soc. A **211**, 500 (1952).
   (b) L. D. Landau and E. M. Lifshitz, *Quantum Mechanics: non-relativistic theory*, (Pergamon, Oxford, 1977), Chap. XV.
   (c) T. Dittrich, P. Hänggi, G.-L. Ingold, B. Kramer, G.Schön, and W. Zwerger, *Quantum Transport and Dissipation*, (Wiley-VCH, Weinheim, 1998), Chap. 2.
2. Integer quantum Hall effect:
   (a) K. von Klitzing, G. Dorda, and M. Pepper, Phys. Rev. Lett. **45**, 494 (1980).
   (b) R. B. Lauglin, Phys. Rev. B **23**, 5632 (1981).
   (c) B. I. Halperin, Phys. Rev. B **25**, 2185 (1982).
3. Topological aspects, quantum Hall effect in periodic systems:
   (a) D. J. Thouless, M. Kohmoto, M. P. Nightingale, M. den Nijs, Phys. Rev. Lett. **49**, 405 (1982).
   (b) M. Kohmoto, Ann. Phys. (NY) **160**, 343 (1985).
   (c) Q. Niu, D. J. Thouless, and Y.-S. Wu, Phys. Rev. B **31**, 3372 (1985).
   (d) I. Dana, Y. Avron, and J. Zak, J. Phys. C: Solid State Phys. **18**, L679 (1985).
   (e) D. J. Thouless, in *The Quantum Hall Effect*, edited by R. Prange and S. M. Girvin (Springer-Verlag, New York, 1987), Chap. 4.
4. Magnetic translations:
   (a) E. Brown, Phys. Rev. **133**, A1038 (1964).
   (b) J. Zak, Phys. Rev. **134**, A1602 (1964).
   (c) J. Zak, Phys. Rev. **134**, A1607 (1964).

5. kq-function, kq-representation:

   (a) J. Zak, Phys. Rev. Lett. **19**, 1385 (1967).

   (b) J. Zak, Phys. Rev. **168**, 686 (1968).

   (c) J. Zak, Physics Today **23** No. 2, 51 (1970).

   (d) J. Zak, J. Phys. A: Math. Gen. **30**, L 549 (1997).

6. The butterfly:

   (a) M. Ya. Azbel', Zh. Eksp. Teor. Fiz. **46**, 929 (1964) [Sov. Phys. JETP **19**, 634 (1964)].

   (b) D. R. Hofstadter, Phys. Rev. B **14**, 2239 (1976).

7. Experimental observation of the butterfly:

   (a) T. Schlösser, K. Ensslin, J. P. Kotthaus, and M. Holland, Semicond. Sci. Technol. **11**, 1582 (1996).

   (b) C. Albrecht, J. H. Smet, K. von Klitzing, D. Weiss, V. Umansky and H. Schweizer, Phys. Rev. Lett. **86**, 147 (2001).

8. Commensurability in transport:

   (a) D. Weiss, K. v. Klitzing, K. Ploog, and G. Weimann, Europhys. Lett. **8**, 179 (1989).

   (b) R. W. Winkler, J. P. Kotthaus, and K. Ploog, *ibid.* **62**, 1177 (1989).

   (c) R. Fleischmann, T. Geisel, R. Ketzmerick, Phys. Rev. Lett. **68**, 1367 (1992).

   (d) É. M. Baskin, G. M. Gusev, Z. D. Kvon, A. G. Pogosov, and M. V. Éntin, JETP Lett. **55**, 678 (1992).

9. Optical experiments:

   (a) K. Kern, D. Heitmann, P. Grambow, Y. H. Zhang, and K. Ploog, Phys. Rev. Lett. **66**, 1618 (1991).

   (b) K. Bollweg, T. Kurth, D. Heitmann, E. Vasiliadou, K. Eberl, and H. Brugger, Phys. Rev. B **52**, 8379 (1995).

Papers

Butterfly-like spectra and collective modes of antidot superlattices in magnetic fields

Egidijus Anisimovas* and Peter Johansson†
Department of Theoretical Physics, University of Lund, Sölvegatan 14 A, S-223 62 Lund, Sweden

We calculate the energy band structure for electrons in an external periodic potential combined with a perpendicular magnetic field. Electron-electron interactions are included within a Hartree approximation. The calculated energy spectra display a considerable degree of self-similarity, just as the "Hofstadter butterfly." However, screening affects the butterfly, most importantly the bandwidths oscillate with magnetic field in a characteristic way. We also investigate the dynamic response of the electron system in the far-infrared (FIR) regime. Some of the peaks in the FIR absorption spectra can be interpreted mainly in semiclassical terms, while others originate from inter(sub)band transitions.

PACS numbers: 73.20.Dx, 73.20.Mf

Recent years have witnessed a considerable amount of research effort directed towards understanding of the physics of two-dimensional electron systems (2DES) whose dimensionality is further restricted by man-made periodic potentials and perpendicular magnetic fields. These include quantum dot arrays and antidot superlattices. Concentrating on the latter ones, one distinguishes two principal directions of experimental work: transport studies and far infrared (FIR) spectroscopy. Some of the transport measurements[1,2] have been performed in search of evidence for a self-similar energy spectrum, the so called Hofstadter butterfly.[3] A main theme in the FIR absorption experiments has been to detect and classify the rich variety of collective modes that occur in these systems.[4–6]

Along with the experimental work, theorists have addressed the same issues.[7–13] The main difficulty lies in the fact that while the superlattice is periodic, the Hamiltonian (including a vector potential) is not. Most recent calculations of superlattice electronic structure have used the Ferrari basis to deal with this matter.[14] We will instead apply ray-group-theoretical techniques[15–18] to effectively reduce the calculational complexity.

With this approach, we are able to go beyond earlier calculations. We find the band structure for *interacting* electrons in general "rational" magnetic fields [i.e., the flux through a unit cell is $(L/N)\Phi_0$, where Φ_0 is a flux quantum and $L, N \in \mathcal{Z}$]. Consequently, we are able to trace even fine-scale features of the butterfly and at the same time study the effects screening has on it. We also explore the FIR response. The resulting spectra are rather rich. Along with absorption peaks caused by collective modes, and known from experiments,[4,5] we find additional ones of mostly quantum-mechanical origin.

The antidot superlattice considered here is of simple square symmetry $\mathbf{R} = n_1\mathbf{a}_1 + n_2\mathbf{a}_2$, with lattice parameter a. The effective one-particle Hamiltonian is

$$H = \frac{1}{2m}\left(\mathbf{p} + \frac{e}{c}\mathbf{A}\right)^2 + \sum_{\mathbf{G}} v(\mathbf{G})\mathrm{e}^{i\mathbf{G}\cdot\mathbf{r}}, \tag{1}$$

where the vector potential $\mathbf{A} = \mathbf{B}\times\mathbf{r}/2$ (symmetric gauge) describes the perpendicular magnetic field $\mathbf{B}$ and $\mathbf{G} = g_1\mathbf{b}_1 + g_2\mathbf{b}_2$, denotes the reciprocal lattice vectors. We use GaAs parameters and work with short-period superlattices with $a = 1000$ Å and electron density $n_s = 1.2\cdot 10^{11}$ cm^{-2}. A typical magnetic field $B = 1.65$ T gives four flux quanta per unit cell, filling factor $\nu = 1.5$, and the cyclotron energy $\hbar\omega_c = 2.86$ meV, where $\omega_c = eB/mc$. The last term in Eq. (1) is a sum of the external superlattice potential, described by a few principal Fourier components,[19] and the Hartree potential. As for electron spin, we keep the twofold degeneracy in mind when counting states, but neglect other effects such as Zeeman splitting and exchange interaction.

The electronic states we set out to solve for will satisfy the modified Bloch conditions

$$\hat{T}_M(\mathbf{a}_{1(2)})\psi_{\mathbf{q}} = \mathrm{e}^{-i\mathbf{a}_{1(2)}\cdot\mathbf{q}}\psi_{\mathbf{q}} \tag{2}$$

when the magnetic flux through a unit cell equals an integer number of flux quanta Φ_0. Here

$$\hat{T}_M(\mathbf{R}) = \exp\left[-\frac{i}{\hbar}\mathbf{R}\cdot\left(\mathbf{p} - \frac{e}{c}\mathbf{A}\right)\right] \tag{3}$$

are magnetic translation operators forming a ray group,[20] and the eigenstates can still be classified by different values of the crystal momentum $\mathbf{q} = q_1\mathbf{b}_1 + q_2\mathbf{b}_2$, in the first Brillouin zone.[15] Actually, one finds sets of L linearly independent functions each transforming according to the same irreducible representation. This manifests itself as the splitting of the Landau band into L subbands. For rational fields with flux $(L/N)\Phi_0$ per unit cell, the

irreducible representations of the group (3) are N-dimensional and the states N-fold degenerate. This calls for a generalized treatment[15,17,21] which we have implemented but do not further describe here.

The next important step towards a solution is a canonical coordinate transformation.[17] We switch to dimensionless units[22] to be used hereafter, and introduce

$$\xi(\eta) = \pm p_y + x/2, \quad p_{\xi(\eta)} = p_x \mp y/2. \tag{4}$$

This preserves the canonical commutators, maps the kinetic energy of the Hamiltonian in the symmetric gauge onto a harmonic oscillator in ξ, and makes the magnetotranslations act only on η,

$$H_0 = \frac{1}{2}\left(\xi^2 + p_\xi^2\right), \; \hat{T}_M(\mathbf{R}) = \exp\left(-iR_x p_\eta + iR_y\eta\right). \tag{5}$$

The periodic potential mixes the ξ and η degrees of freedom (in these coordinates it behaves like a magnetic translation operator)

$$\begin{aligned} H_1 \;=\; & \sum_{\mathbf{G}} v(\mathbf{G})\hat{X}(\mathbf{G}|\xi)\hat{Y}(\mathbf{G}|\eta), \\ & \hat{X}(\mathbf{G}|\xi) = \exp(iG_x\xi - iG_y p_\xi), \\ & \hat{Y}(\mathbf{G}|\eta) = \exp(iG_x\eta + iG_y p_\eta). \end{aligned} \tag{6}$$

Using projection-operator techniques we find the symmetry-adapted η-dependent functions

$$\varphi(\mathbf{q}, l|\eta) = \sum_{m=-\infty}^{\infty} \mathrm{e}^{2\pi i m q_1}\,\delta\left(\eta + \frac{aq_2}{L} - \frac{al}{L} - am\right), \tag{7}$$

labeled by the magnetic crystal momentum $\mathbf{q}$ in the first magnetic Brillouin zone (i.e., $0 \le q_1, q_2 < 1$) and the subband index $l = 0, \ldots, L-1$. Now the Ansatz

$$\psi(\mathbf{q}, l|\xi, \eta) \;=\; \sum_{l=0}^{L-1} \varphi(\mathbf{q}, l|\eta) \sum_{n=0}^{\infty} a_{nl}\chi_n(\xi) \tag{8}$$

for the eigenstates allows for subband mixing, and the ξ-dependence is accounted for by an expansion in harmonic oscillator eigenfunctions χ_n. Inserted

into the Schrödinger equation, the Ansatz yields the eigenvalue problem determining the electron states

$$\sum_{n'l'} \Big\{\delta_{nn'}\delta_{ll'}\left(n+\frac{1}{2}\right) + \sum_{\mathbf{G}} v(\mathbf{G})A_{ll'}(\mathbf{G})B_{nn'}(\mathbf{G})\Big\}a_{n'l'} = Ea_{nl}. \tag{9}$$

The subband and Landau-level mixing coefficients are

$$\begin{aligned} A_{ll'}(\mathbf{G}) &= \mathrm{e}^{2\pi i\left[g_1g_2/2+g_1l+(q_1g_2-q_2g_1)+q_1(l-l')\right]/L}\delta^{(\mathrm{mod}L)}_{l',l+g_2}, \\ B_{nn'}(\mathbf{G}) &= \int_{-\infty}^{\infty}\chi_n(\xi)\hat{X}(\mathbf{G}|\xi)\chi_{n'}(\xi)d\xi. \end{aligned} \tag{10}$$

Equation (9) must be iterated together with the Poisson equation updating the Hartree potential until self-consistency is reached.

Figure 1 shows the splitting of the first four Landau levels as a function of the dimensionless inverse flux $\Phi_0/(Ba^2) = N/L$. With a reasonable computational effort we could treat rational fields with $L \leq 14$ and all possible N's. This is enough to clearly resolve the intricate subband clustering.[3]

It is easy to see that the bandwidths in Fig. 1 decrease with increasing magnetic flux; however, the decrease is not monotonous. Instead they have maxima for flux values 6, 3, and 2, (see the inset) when there are 1, 2, and 3 completely filled Landau levels, respectively. Then the 2DES cannot screen the external potential very effectively, and the Fourier coefficients $v(\mathbf{G})$ are larger than for other flux values. Thus, since the bandwidth is set by a competition between the band-narrowing effects of the magnetic field and the band broadening tendencies of the potential, this leads to a cusped behavior of the band top and bottom at integer filling factors. For the filling factors $\nu \leq 1$ we also observe the same qualitative behavior while quantitative predictions of the Hartree theory in this region may be inaccurate. We note that there exist other (unrelated to electron-electron interaction) mechanisms which also lead to nonmonotonous bandwidths.[13]

Electron-electron interaction also contributes to diminishing the symmetry of the butterfly as strong coupling between different bands does.[11,13] The second and third bands in Fig. 1 which are traversed by the chemical potential μ show reduced regularity if compared to well-separated noninteracting bands in Fig. 3 (a) of Ref. 13, whereas our fourth band, well above μ, would exhibit a considerable resemblance to Hofstadter's one-band picture when properly rescaled.

Turning to the dynamic response of the 2DES, we calculate the density-density response function $R_{\mathbf{GG}'}(\mathbf{k},\omega)$ within the random-phase approximation

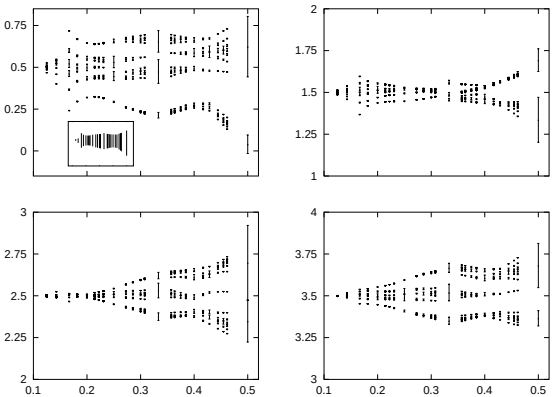

FIG. 1: The width of the four lowest Landau bands (in units $\hbar\omega_c$) plotted versus inverse magnetic flux. The four principal Fourier components of the potential $[v^{\rm ext}(0,\pm1)$ and $v^{\rm ext}(\pm1,0)]$ are set to 1.43 meV, $a = 1000$ Å, and $n_s = 1.2 \cdot 10^{11}$ cm^{-2}. The bands are centered around the limiting Landau level values $n+1/2$ and get broader as the magnetic field decreases. The commensurability phenomena manifest themselves in the intricate splitting of the bands. To underscore the nonmonotonous dependence of broadening on the magnetic field, we also display the overall band widths in the inset of the left upper graph.

(RPA) by solving the set of equations

$$R_{\mathbf{GG}'} = P_{\mathbf{GG}'} + \sum_{\mathbf{G}''} P_{\mathbf{GG}''} V_{\rm ee}(\mathbf{k}+\mathbf{G}'') R_{\mathbf{G}''\mathbf{G}'}. \tag{11}$$

Here $P_{\mathbf{GG}'}$ is the independent particle response function which we can evaluate knowing the electron eigenstates already calculated. The FIR absorption of the long wavelength ($\mathbf{k}$ in the first Brillouin zone) light is proportional to $-\omega {\rm Im} R_{00}(\omega)$.[23]

The so calculated spectra typically exhibit several conspicuous peaks. In Fig. 2 (a), we display spectra calculated for electron densities $n_s = 1.2 \cdot 10^{11}$ cm^{-2} and $1.4 \cdot 10^{11}$ cm^{-2}, respectively, and wave vector $\mathbf{k} = (\pi/10)a^{-1}\hat{x}$. Following the suggestion of Ref. 10 to classify the different peaks by studying the corresponding charge fluctuations; we also trace their development in time to pick out the ones that are stable with respect to changing electron density. Here we try to concentrate on a few of these plots and give a thorough discussion of them. To this end we calculate the time-dependent, induced charge density at the absorption-peak frequencies in four adjacent unit cells, and plot snapshots

thereof in Fig. 2 (b) and (c). The antidots are situated at the intersections of the thick lines and the "+"("-") signs mark the locations of the charge density maxima (minima).

The two spectra shown in Fig. 2 (a) calculated for different electron densities are very similar. At the same time, however, the induced charge densities at the different peaks can in general change quite a lot with changing electron density. There are a few exceptions to this, most notably the peaks marked (H) and (L) and indicated by arrows. As we will see, one can give a clear, semiclassical interpretation to these modes.

Thus, Fig. 2 (b) shows the charge density corresponding to the (H) peak in Fig. 2 (a). One sees a dipole which, looking at a sequence of snapshots, rotates around the center of each lattice cell (i.e., between four antidots) in the direction of cyclotron motion. This mode, which can be anticipated on general grounds, emerges in simple theoretical models[7] and has been detected experimentally.[4,5]

In the low frequency region we find a more complicated collective mode [peak (L) in Fig. 2 (a)] depicted in Fig. 2 (c). A dipolar charge distribution is rotating around each antidot *in* the direction of cyclotron motion, and a "ring" of three charge density maxima and three minima between the antidots is rotating in the *opposite* direction. During each period one sees some small charge transfer between the two structures. We interpret this mode as a pair of coupled (inter)edge magnetoplasmons with angular momenta $l = +1$ and $l = -3$ around an antidot and the center of a cell, respectively. The dynamics of this mode is mainly determined by an equilibrium between the Lorentz force and restoring electrostatic forces. From this follows that the magnetoplasmon propagates in opposite directions around a charge density maximum (a cell center) and a minimum (an antidot).[24] Note also that this mode is an example of mixing of states with angular momenta differing by a multiple of four in a square lattice.

Both peaks, (H) and (L), show absorption of light polarized in the direction of the cyclotron resonance in agreement with experiment.[5] The existing theoretical explanation,[7] however, is based on a model with circularly symmetric unit cells and cannot describe the interplay of modes centered at different places of the unit cell. Besides the modes discussed until now the 2DES absorbs energy at a number of other frequencies. The corresponding induced charge distributions are more complex than the ones displayed in Figs. 2 (b) and (c). These excitations are to a large extent of a quantum-mechanical nature, i.e., the result of intersubband and inter-Landau-level transitions (see also Ref. 9). In this context, it is also clear that our spectra obtained for short-period superlattices are not completely comparable to the ones found experimentally. There are two main reasons for this, the potential has a stronger influence on electron motion, and we have not treated disorder broadening.

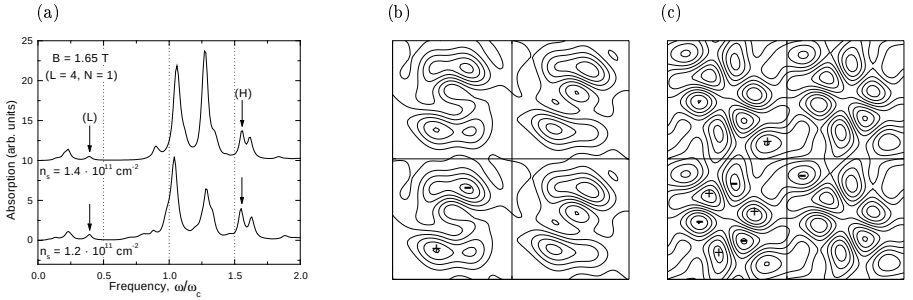

FIG. 2: Absorption spectra (panel a) and the oscillating charge-density distributions associated with the peaks indicated by arrows (H $\leftrightarrow$ panel b) and (L $\leftrightarrow$ panel c), respectively. The upper curve in (a) is offset by 10. The external potential has Fourier components $v^{\rm ext}(0,\pm1) = v^{\rm ext}(\pm1,0) = \hbar\omega_c = 2.86$ meV and $v^{\rm ext}(0,\pm2) = v^{\rm ext}(\pm2,0) = \hbar\omega_c/4$. For the high-frequency mode one sees in (b) a dipole rotating around the center of each lattice cell. For the low-frequency mode one can in (c) observe a dipole centered on each of the antidots and a hexagonal pattern between the antidots. One structure of each kind is marked with signs.

In conclusion, we have developed a theory that makes it possible to study the electronic structure of a 2DES in a combined periodic potential and strong magnetic field in a detailed fashion treating electron-electron interactions at the mean-field level. The so calculated energy spectra show clear traces of a self-similar structure like the Hofstadter butterfly, however, considerably modified by screening effects. The dielectric response of the 2DES in the FIR regime reveals a rich spectrum of excitations. Some of the peaks in these spectra can be interpreted in terms of semiclassical collective excitations, while others mainly are of a quantum-mechanical origin.

We thank Carlo Canali, Carl-Olof Almbladh, and Koung-An Chao for valuable discussions. One of us (P.J.) is supported by the Swedish Natural Science Research Council (NFR).

REFERENCES

* Electronic address: `egidijus@teorfys.lu.se`
† Electronic address: `epj@teorfys.lu.se`

[1] R. R. Gerhardts, D. Weiss, and U. Wulf, Phys. Rev. B **43**, 5192 (1991).
[2] K. Ensslin and P. M. Petroff, Phys. Rev. B **41**, 12 307 (1990); A. Lorke, J. P. Kotthaus, and K. Ploog, *ibid.* **44**, 3447 (1991); D. Weiss, M. L. Roukes, A. Menschig,

P. Grambow, K. von Klitzing, and G. Weimann Phys. Rev. Lett. **66**, 2790 (1991); R. Fleischmann, T. Geisel, and R. Ketzmerick, *ibid.* **68**, 1367 (1992).
[3] D. R. Hofstadter, Phys. Rev. B **14**, 2239 (1976); M. Ya. Azbel', Zh. Eksp. Teor. Fiz. **46**, 929 (1964) [Sov. Phys. JETP **19**, 634 (1964)].
[4] K. Kern, D. Heitmann, P. Grambow, Y. H. Zhang, and K. Ploog, Phys. Rev. Lett. **66**, 1618 (1991).
[5] K. Bollweg, T. Kurth, D. Heitmann, E. Vasiliadou, K. Eberl, and H. Brugger, Phys. Rev. B **52**, 8379 (1995).
[6] A. Lorke, I. Jejina, and J. P. Kotthaus, Phys. Rev. B **46**, 12 845 (1992).
[7] G. Y. Wu and Y. Zhao, Phys. Rev. Lett. **71**, 2114 (1993).
[8] D. Huang and G. Gumbs, Phys. Rev. B **47**, 9597 (1993).
[9] V. Gudmundsson and R. R. Gerhardts, Phys. Rev. B **54**, 5223 (1996).
[10] V. Gudmundsson, Phys. Rev. B **57**, 3989 (1998).
[11] G. Petschel and T. Geisel, Phys. Rev. Lett. **71**, 239 (1993).
[12] V. Gudmundsson and R. R. Gerhardts, Phys. Rev. B **52**, 16 744 (1995).
[13] D. Springsguth, R. Ketzmerik, and T. Geisel, Phys. Rev. B **56**, 2036 (1997).
[14] R. Ferrari, Phys. Rev. B **42**, 4598 (1990).
[15] E. Brown, Phys. Rev. **133**, A1038 (1964).
[16] J. Zak, Phys. Rev. **136**, A1647 (1964).
[17] H.-J. Schellnhuber, Phys. Rev. B **25**, 2358 (1982).
[18] H.-J. Schellnhuber and G. Obermair, Phys. Rev. Lett. **45**, 276 (1980); G. M. Obermair and H.-J. Schellnhuber, Phys. Rev. B **23**, 5185 (1981); H.-J. Schellnhuber, G. M. Obermair, and A. Rauh, *ibid.* **23**, 5191 (1981).
[19] In the FIR calculations we use $v^{\rm ext}(0,\pm1) = v^{\rm ext}(\pm1,0) = \hbar\omega_c$ and make the potential profile steeper and, most likely, more realistic by setting $v^{\rm ext}(0,\pm2) = v^{\rm ext}(\pm2,0) = \hbar\omega_c/4$, with $\hbar\omega_c = 2.86$ meV. Plotting the butterfly we reduce the potential to $v^{\rm ext}(0,\pm1) = v^{\rm ext}(\pm1,0) = 1.43$ meV in order to prevent the bands from overlapping since this is known to reduce the self similarity.[11]
[20] M. Hamermesh, *Group Theory and its Application to Physical Problems*, (Dover, New York, 1989), Chap. 12.
[21] Rational fields increase the analytic but not the numerical complexity of the problem.
[22] Distances are measured in terms of the magnetic length $l_c = \sqrt{\hbar c/eB}$, momenta in $\hbar l_c^{-1}$, and energies in $\hbar\omega_c$.
[23] C. Dahl, Phys. Rev. B **41**, 5763 (1990).
[24] P. K. H. Sommerfeld, P. P. Steijaert, P. J. M. Peters, and R. W. van der Heijden, Phys. Rev. Lett. **74**, 2559 (1995).

Electronic structure of antidot superlattices in commensurate magnetic fields

Egidijus Anisimovas[1,*] and Peter Johansson[1,2]
[1] *Division of Solid State Theory, Department of Physics, University of Lund, Sölvegatan 14 A, S-223 62 Lund, Sweden*
[2] *Department of Natural Sciences, University of Örebro, S-701 82 Örebro, Sweden*

We present a treatment of an interacting two-dimensional electron system moving in a bidirectionally periodic potential and a perpendicular magnetic field. Employing symmetry considerations based on the ray-group of magnetotranslation operators and a canonical coordinate transformation, we derive an efficient scheme for calculating energy levels and states in arbitrary "rational" magnetic fields. Applying this scheme to a superlattice of strongly localized antidots we reveal the possibility to split off an isolated and sufficiently broad cluster of subbands from a Landau band. The implications of existence of such subbands to the experimental detection of the subband structure and in particular quantum Hall effect measurements in periodic superlattices are discussed.

PACS numbers: 73.20.Dx, 03.65.-w

I. INTRODUCTION

Inspired by advances in submicron technology, recently there has been a considerable amount of both theoretical and experimental work aimed at understanding of the physics which governs the behaviour of realistic quasi-two-dimensional electron systems (2DES) subjected to perpendicular magnetic fields and man-made lateral periodic confinements. Such systems have been prepared and investigated covering a wide range of periodic modulation strength. In weakly perturbed 2DES, a main pursuit was the commensurability-related magnetoresistance oscillations[1] explained by the broadening of Landau levels into bands. When the superlattice potential is applied in both lateral directions,[2–4] an additional aspect, namely the splitting of a Landau band into a complicated system of subbands[5,6] arises. Posing a real challenge for experimentalists, only recently some indications of such splitting were observed in magnetoresistance oscillations of small-period lateral superlattices.[7]

The splitting of a Landau band into a number of subbands also leads to the redistribution of the quantum Hall (QH) current among them. While the total current in a band is conserved, and the QH conductance associated with each subband is still an integer (in units e^2/h), this integer need not equal unity.[8,9] The detection of nontrivial, that is different from 0 or 1, QH conductances is of great experimental interest, however, the complexity of such a measurement (at least, in smooth periodic potentials) is even greater than that of the detection of subbands themselves. The reason for this lies in the fact that the subbands tend to arrange themselves into a hierarchical structure[5,6] by forming clusters separated by large gaps, while inside each cluster smaller sub-clusters separated by smaller subgaps are formed. Having resolved the cluster structure at the coarsest level one would find that one cluster is carrying the total band's current while the others do not contribute at all. Thus, trying to access higher integers in the QH current distribution one is facing an immensely difficult task of resolving at least the second order sub-splittings. A recent experiment[10] considered the situation where the partial contributions of three subbands to the total QH current follow the pattern 1, -1, 1, so that the net conductance would show oscillations between 0 and 1. Due to the smallness of the minigaps the QH conductances did not fully attain the expected values, however, the indicative nonmonotonicity was clearly visible. In the present paper, we show that if the periodic potential is not smooth but rather composed of steep antidots, the distribution of band-widths among the subbands can be made very different thus increasing the feasibility of experimental access to the subbands carrying nontrivial QH currents. Moreover, we find that sufficiently steep potential profiles are not smoothened away by the screening charge of electrons.

Attempts to address the complicated topic of electron motion in a periodic potential and a competing magnetic field theoretically date back to the 1950's. The simplest descriptive model, known as Harper's equation,[11] was derived in two limiting cases: (i) that of a weak perturbative periodic potential imposed upon otherwise flat Landau levels,[12,13] and (ii) that of a single tight-binding band subjected to a weak magnetic field.[11,12] The efforts culminated in Hofstadter's calculation[6] of splitting and clustering of subbands into a complicated pattern depending on the ratio of the magnetic flux through a unit cell to the magnetic flux quantum. This treatment was based on the so-called Peierls substitution[14] and had a fairly limited range of validity,[15] however it gave a qualitatively correct visualization of the phenomenon.

Later on, the technological advances have renewed the theoretical interest in the field calling for a more realistic treatment. Harper's equation was generalized[16] to include interband coupling and thus properly accounted for predominant chaotic trajectories[17] in the near-classical regime. The electron-

electron interaction was still not addressed. Its study was initiated[18] by introducing a self-consistency procedure using the Ferrari basis[19] into the band structure calculations. In this method one explicitly constructs translationally invariant states thus taking the crystal symmetry into account. In practice, however, the method turned out to be computationally demanding and provided answers only for a set of special (integer) magnetic fields and unusually low electron densities.[18] Thus, a new effort to address a dense set of (rational) magnetic fields and Coulomb repulsion between electrons was clearly needed.

In the present paper, we put forward a computational scheme capable of dealing with both integer and rational magnetic fluxes at the same level of complexity. We base on the treatment of crystal symmetry in magnetic fields,[20] and its application by Schellnhuber and co-workers[21,22] to calculations of diamagnetic band structure in three-dimensional solids. In a previous publication[23] we treated the energy spectra of 2DES in the case of integer fluxes and smooth potentials.

After the original investigation by Thouless et al.,[8] the problem of the distribution of QH currents among subbands in a single band approximation was recently discussed by Chang and Niu[24] from the point of view of semiclassical electron dynamics. The changes induced by coupling between several Landau bands were addressed in Ref. 25. In the present paper we extend the previous investigations by (i) showing that superlattices composed of steep antidots provide a systematic way of increasing the widths of interesting (from the point of view of QH measurement) subgaps and (ii) including and discussing the role of the electron-electron interactions.

The paper has the following structure. In Sec. II the model is formulated and in Sec. III the symmetry-based analytical scheme is derived. In Sec. IV we discuss some limiting cases and carry out a calculation of the band structure of antidot superlattices paying particular attention to the appearance of an isolated cluster of subbands that splits off from a Landau band. Such subbands (we refer to them as "levitating"), being considerably broad and isolated from the other ones by large gaps, increase our hopes that they (or even their internal structure) can be more easily resolved in an experiment and reveal some nontrivial QH numbers. We conclude with a summarizing Section V, while some of matters are relegated to the Appendices.

II. MODEL

We consider a 2D antidot superlattice and its reciprocal counterpart spanned by the respective vectors $\mathbf{R} = n_1\mathbf{a}_1 + n_2\mathbf{a}_2$ and $\mathbf{G} = g_1\mathbf{b}_1 + g_2\mathbf{b}_2$ with

$n_{1(2)}, g_{1(2)} \in \mathcal{Z}$ and $\mathbf{a}_i \cdot \mathbf{b}_j = 2\pi\delta_{ij}$. While no special restrictions on the point symmetry are imposed, it is convenient to choose $\mathbf{a}_2 \parallel y$ so that $\mathbf{b}_1 \parallel x$. In a non-orthogonal lattice, $\mathbf{a}_1$ will also have a component along y, so we introduce the lattice "skewness" parameter $s = a_{1y}/a_{2y}$ for this case. The independent-particle Hamiltonian of an electron moving in the crystal potential of such a lattice and a perpendicular magnetic field reads

$$H = \frac{1}{2m}\left(\mathbf{p} + \frac{e}{c}\mathbf{A}\right)^2 + \sum_{\mathbf{G}} v(\mathbf{G}) e^{i\mathbf{G}\cdot\mathbf{r}}. \tag{1}$$

Here, the periodic potential is given in terms of its Fourier components $v(\mathbf{G})$ and the magnetic field is expressed via its symmetric-gauge vector potential $\mathbf{A}(\mathbf{r}) = \frac{1}{2}[\mathbf{B} \times \mathbf{r}]$. Our method can treat all so-called rational fields, i.e. such that the magnetic flux per unit cell equals a rational number of magnetic flux quanta $\Phi_0 = ch/e$:

$$\Phi/\Phi_0 = L/N, \quad L, N \in \mathcal{Z}. \tag{2}$$

Concentrating on the physics that is not crucially influenced by the electron spin, we neglect the exchange interaction and Zeeman splitting but do take the degeneracy due to spin into account.

The electrons are described in the effective-mass approximation using $m = 0.067\, m_0$ moving in a medium of dielectric constant $\kappa = 12.4$. We concentrate on short-period superlattices. In the calculation we set the lattice constant to $a = 1000$ Å; then a moderate magnetic field $B = 1.65$ T produces a commensurate flux equal to 4 flux quanta per unit cell. The Coulomb repulsion is included at the mean-field level. Thus, the periodic potential entering (1) is a sum of the "external" antidot potential and the Hartree term

$$v(\mathbf{G}) = v^{\text{ext}}(\mathbf{G}) + \frac{2\pi}{|\mathbf{G}|}\frac{e^2}{\kappa} n_s(\mathbf{G})(1 - \delta_{\mathbf{G},0}), \tag{3}$$

where $n_s(\mathbf{G})$ is the Fourier transformed electron density constructed from the eigenfunctions of the Hamiltonian in Eq. (1), and the Kronecker delta indicates that the $\mathbf{G} = 0$ contribution is cancelled by the positive background charge. Thus, the energy spectrum of Hamiltonian (1) has to be calculated self-consistently by convergent iterations together with equation (3).

In order to make use of the symmetry with respect to discrete translations in a uniform magnetic field we introduce the group of magnetotranslation operators. Their generator is defined so as to commute with the kinetic momentum $\mathbf{p}_{\text{kin}} = \mathbf{p} + \frac{e}{c}\mathbf{A}$, and in the symmetric gauge reads $\mathbf{p}_{\text{gen}} = \mathbf{p} - \frac{e}{c}\mathbf{A}$. Therefore, we have

$$T_M(\mathbf{R})\psi(\mathbf{r}) \;=\; \exp\left[-\frac{i}{\hbar}\mathbf{R}\cdot\left(\mathbf{p} - \frac{e}{c}\mathbf{A}\right)\right]\psi(\mathbf{r})$$

$$= \exp\left(\frac{ie}{2\hbar c}\mathbf{r}\cdot[\mathbf{R}\times\mathbf{B}]\right)\psi(\mathbf{r}-\mathbf{R}). \tag{4}$$

The operators T_M appearing in Eq. (4) commute with the Hamiltonian (1) thus allowing for a classification of its eigenstates by their translational symmetry properties. Note, however, that a product of two magnetotranslations equals another member of the group only up to a phase

$$T_M(\mathbf{R}_1)T_M(\mathbf{R}_2) = T_M(\mathbf{R}_1+\mathbf{R}_2)e^{-(ie/2\hbar c)\mathbf{B}\cdot[\mathbf{R}_1\times\mathbf{R}_2]} \tag{5}$$

indicating that one deals here with a ray group[26] rather than a conventional vector group. Nevertheless, the conventional framework of group-theoretical treatment remains applicable.[20]

III. THEORY

Having spelled out all the definitions in full in the preceding Sec. II, we now switch to natural dimensionless units. We use the cyclotron frequency and the magnetic length

$$\omega_c = \frac{eB}{mc}, \quad l_c = \sqrt{\frac{\hbar c}{eB}} \tag{6}$$

as the defining quantities, and from now on measure all lengths in l_c, momenta in $\hbar l_c^{-1}$, and energies in $\hbar\omega_c$. The rationality condition (2) is cast into a relation for the unit-cell area

$$\Omega = a_{1x}a_{2y} = 2\pi L/N \tag{7}$$

to be extensively used in algebraic manipulations hereafter.

Further, we perform a canonical coordinate transformation[22] to a new set of variables ξ and η

$$\begin{aligned} \xi &= p_y + x/2, \quad p_\xi = p_x - y/2, \\ \eta &= -p_y + x/2, \quad p_\eta = p_x + y/2, \end{aligned} \tag{8}$$

which maps the kinetic-energy part of the Hamiltonian (denoted H_0) onto that of a harmonic oscillator in ξ

$$H_0 = \frac{1}{2}\left(p_\xi^2 + \xi^2\right). \tag{9}$$

Moreover, the translations (4) are now found to act only on the η coordinate

$$T_M(\mathbf{R}) = \exp(-iR_x p_\eta + iR_y \eta). \tag{10}$$

Thus, the complexity has been isolated into the periodic potential term which has become a function of both the new coordinates and momenta. Its Fourier components behave like magnetic translation operators

$$\begin{aligned} H_1 &= \sum_{\mathbf{G}} v(\mathbf{G}) \hat{X}(\mathbf{G}|\xi) \hat{Y}(\mathbf{G}|\eta), \\ & \hat{X}(\mathbf{G}|\xi) = \exp(iG_x \xi - iG_y p_\xi), \\ & \hat{Y}(\mathbf{G}|\eta) = \exp(iG_x \eta + iG_y p_\eta) \end{aligned} \tag{11}$$

and will mix the ξ and η degrees of freedom.

The transformation of states between (x, y) and (ξ, η) representations is given by

$$\langle xy|\psi\rangle = \int_{-\infty}^{\infty} d\xi \int_{-\infty}^{\infty} d\eta \, \langle xy|\xi\eta\rangle \langle \xi\eta|\psi\rangle \tag{12}$$

with the kernel $\langle xy|\xi\eta\rangle$ obtained by solving the eigenvalue equations for ξ and η

$$\begin{aligned} \left(\frac{x}{2} - i\frac{\partial}{\partial y} - \xi\right) \langle xy|\xi\eta\rangle &= 0, \\ \left(\frac{x}{2} + i\frac{\partial}{\partial y} - \eta\right) \langle xy|\xi\eta\rangle &= 0 \end{aligned} \tag{13}$$

with the result

$$\langle xy|\xi\eta\rangle = \frac{1}{\sqrt{2\pi}} e^{iy(\xi-\eta)/2} \delta(x - \xi - \eta). \tag{14}$$

A. Symmetry adapted basis

In order to take full advantage of the symmetry properties of the system, the next step towards a solution is the decomposition of the functional space $\mathcal{F}(\xi, \eta)$ of all functions of ξ and η into invariant subspaces of the symmetry group. Since the different subspaces are not coupled by the Hamiltonian, the effort needed to diagonalize it is reduced. Moreover, thanks to the canonical transformation

the magnetotranslations now act only on the η degree of freedom, so the task narrows to a construction of a symmetry-adapted basis that spans $\mathcal{F}(\eta)$. As we will see, the dimensionality of the invariant subspaces equals L, therefore the Ansatz for the states will involve a linear combination of L η-dependent functions multiplied by a suitable expansion of the ξ-dependent part.

The construction of the symmetry-adapted basis for the η degree of freedom proceeds by employing the projection-operators technique. We use the irreducible representations of the magnetotranslation group given in Ref. 20. They are labelled by the magnetic crystal momentum vector $\mathbf{q} = q_1\mathbf{b}_1 + q_2\mathbf{b}_2$ and relate to the "central" ($\mathbf{q} = 0$) one as

$$D^{\mathbf{q}}(\mathbf{R}) = e^{-i\mathbf{q}\cdot\mathbf{R}} D^0(\mathbf{R}) = e^{-2\pi i(n_1 q_1 + n_2 q_2)} D^0(\mathbf{R}). \tag{15}$$

The $N \times N$ matrix D^0 for any translation vector $\mathbf{R}$ is generated from those corresponding to the primitive lattice vectors[20,27]

$$D^0_{jk}(\mathbf{a}_1) = \delta_{jk} e^{2\pi i(j-1)L/N}, D^0_{jk}(\mathbf{a}_2) = \delta^{\bmod N}_{j,k-1} \tag{16}$$

and the ray-group multiplication law (5) yielding

$$D^0_{jk}(\mathbf{R}) = \delta^{\bmod N}_{j,k-n_2} \exp\left\{ i\pi \frac{L}{N} n_1 [n_2 + 2(j-1)] \right\}. \tag{17}$$

Note that increasing any of q_1 or q_2 by $1/N$ produces an equivalent representation. Thus the values of $\mathbf{q}$ have to be restricted to a single magnetic Brillouin zone (MBZ) which we choose as $0 \le q_1, q_2 < 1/N$. The rank of the matrices implies the existence of N partner functions (indexed by $t = 1, \ldots, N$) transforming according to different rows of the same irreducible representation $D^{\mathbf{q}}$. However, in the subsequent analysis we concentrate only on one ($t = 1$) of the partners for the others can be easily obtained from it by means of a translation parallel to $\mathbf{a}_2$. This and other transformation properties of the states are discussed in Appendix A.

In order to construct the principal partner function we introduce the projection operator projecting onto the first row of the $\mathbf{q}$-th representation

$$P^{\mathbf{q}}_{11} = \sum_{\mathbf{R}} [D^{\mathbf{q}}_{11}(\mathbf{R})]^* T_M(\mathbf{R}). \tag{18}$$

After a number of straightforward algebraic steps (see Appendix B for some details and comments) we arrive at the following expressions for the normalized basis functions labelled by a new subband index ($l = 0, 1, \ldots, L-1$) introduced

to account for the presence of L linearly independent basis functions of the same symmetry

$$\begin{aligned}\varphi_l(\mathbf{q}|\eta) &= \sqrt{\frac{2\pi}{a_{2y}}} \sum_{m=-\infty}^{\infty} \exp\left[2\pi i m\left(q_1 - s q_2\right) + i\pi s \frac{m^2 L + 2ml}{N}\right] \\ &\times \delta\left(\eta + N q_2 \frac{a_{1x}}{L} - a_{1x}\frac{l + Lm}{L}\right). \end{aligned} \tag{19}$$

These functions together with the other partner functions constitute a complete orthonormal set in $\mathcal{F}(\eta)$. By construction, the Hamiltonian is diagonal with respect to the quantum numbers q_1, q_2 and t but can mix different subbands l.

B. Eigenvalue problem

Turning to the ξ-dependent part of the wave-function, we see that it can be expanded in any suitable basis independent of the symmetry. Working in the strong magnetic field limit, the harmonic oscillator eigenfunctions $\chi_n(\xi)$ are an appropriate choice. In this case the kinetic energy H_0 is immediately diagonal and the task is to diagonalize H_1. In simple terms, this means that one deals with perturbed Landau levels.

Specializing to this approach, we formulate the following Ansatz for the states

$$\psi(\mathbf{q}|\xi,\eta) = \sum_{n=0}^{\infty} \chi_n(\xi) \sum_{l=0}^{L-1} a_{nl} \varphi_l(\mathbf{q}|\eta), \tag{20}$$

which allows for mixing of different Landau levels and subbands. Upon insertion into the Hamiltonian, one sees that the effect of the operator $\hat{Y}(\mathbf{G}|\eta)$ can be expressed as

$$\hat{Y}(\mathbf{G}|\eta)\varphi_{l'}(\mathbf{q}|\eta) = \sum_{l=0}^{L-1} A_{ll'}(\mathbf{q};\mathbf{G})\varphi_l(\mathbf{q}|\eta), \tag{21}$$

where $A_{ll'}$ is a phase factor whose calculation is straightforward and yields

$$\begin{aligned} A_{ll'}(\mathbf{q};\mathbf{G}) &= \exp\left(i\pi g_1 g_2 \frac{N}{L}\right) \exp\left(2\pi i g_1 \frac{l}{L}\right) \exp\left[2\pi i \frac{N}{L}(q_1 g_2 - q_2 g_1)\right] \\ &\times \exp\left[2\pi i\left(q_1 - s q_2\right)\frac{l - l'}{L}\right] \exp\left(i\pi s \frac{l^2 - l'^2}{NL}\right) \delta_{l', l + N g_2}^{\bmod L}. \end{aligned} \tag{22}$$

Similarly, the effect of $\hat{X}(\mathbf{G}|\xi)$ on a harmonic oscillator function can be written

$$\hat{X}(\mathbf{G}|\xi)\chi_{n'}(\xi) = \sum_{n=0}^{\infty} B_{nn'}(\mathbf{G})\chi_n(\xi), \tag{23}$$

thus mixing Landau levels. Using the defining Eq. (11) we express the ξ-dependent matrix element (23) as

$$\begin{aligned} B_{nn'}(\mathbf{G}) &= e^{-iG_xG_y/2}\int_{-\infty}^{\infty}\chi_n(\xi)\chi_{n'}(\xi - G_y)e^{iG_x\xi}d\xi \qquad (24)\\ &= \sqrt{\frac{2^{n'}n'!}{2^n n!}}e^{-(G_x^2+G_y^2)/4}(G_y + iG_x)^{n-n'}L_n^{n-n'}\left(\frac{G_x^2+G_y^2}{2}\right) = B^*_{n'n}(-\mathbf{G}) \end{aligned}$$

for $n \geq n'$.

The result of the above manipulations is the following eigenvalue problem

$$\begin{aligned} \sum_{n'=0}^{\infty}\sum_{l'=0}^{L-1}\mathcal{M}_{nl;n'l'}a_{n'l'} &= \epsilon a_{nl},\\ \mathcal{M}_{nl;n'l'} = \delta_{nn'}\delta_{ll'}\left(n+\frac{1}{2}\right) &+ \sum_{\mathbf{G}} v(\mathbf{G})A_{ll'}(\mathbf{q};\mathbf{G})B_{nn'}(\mathbf{G}), \end{aligned} \tag{25}$$

whose solutions specify the single particle states and energies. Transforming the symmetry-adapted basis functions $\psi_{nl}(\mathbf{q}|\xi\eta) = \chi_n(\xi)\varphi_l(\mathbf{q}|\eta)$ into the x and y coordinates according to (14) and we obtain

$$\begin{aligned} \psi_{nl}(\mathbf{q}|xy) &= \frac{1}{\sqrt{a_{2y}}}e^{ixy/2}\sum_{m=-\infty}^{\infty}e^{2\pi im(q_1-sq_2)}\\ &\times\ e^{i\pi s(m^2+2ml)/N}e^{-i\kappa_{lm}y}\chi_n(x-\kappa_{lm}),\\ \kappa_{lm} &= a_{1x}\left(-\frac{Nq_2}{L}+\frac{l+mL}{L}\right). \end{aligned} \tag{26}$$

The chosen normalization

$$\int_{-\infty}^{\infty}dx\int_{-\infty}^{\infty}dy\,\psi^*_{n'l'}(\mathbf{q}'|xy)\psi_{nl}(\mathbf{q}|xy) = \delta(q_1-q_1')\delta(q_2-q_2')\delta_{nn'}\delta_{ll'} \tag{27}$$

implies that the states are normalized to N over N adjacent cells along $\mathbf{a}_2$.

We express the eigenstates in real space as

$$\psi^{(\nu)}(\mathbf{q}|xy) = \sum_{n=0}^{\infty} \sum_{l=0}^{L-1} a_{nl}^{(\nu)} \psi_{ln}(\mathbf{q}|xy), \tag{28}$$

where ν numbers the different solutions of Eq. (25). The Fourier components of electron charge density are obtained by Fourier transforming

$$n_s(\mathbf{r}) = 2 \sum_{\mathbf{q},\nu,t} |\psi^{(\nu)}(\mathbf{q}, t|\mathbf{r})|^2 f[\epsilon_\nu(\mathbf{q}) - \mu], \tag{29}$$

where 2 is for spin, $f(\epsilon - \mu)$ denotes the Fermi distribution function and μ is the chemical potential determined by equating the integral of (29) over a unit cell to the average number of electrons per cell. In order to improve the numerical stability, we perform the calculations at several small but finite values of the temperature and then extrapolate to $T = 0$.[28]

It has been shown that the quantized value of QH current carried by a given subband is determined by the total vorticity of the wave-function in MBZ.[8,29] Therefore, the knowledge of energy levels and eigenstates will also specify the QH conductances obtained whenever the chemical potential lies in a gap thus separating the completely filled subbands from the empty ones. A practical way of computing the QH integers σ_H in a gap is given by the thermodynamic Středa formula[9]

$$\frac{e^2}{h}\sigma_H = ec\left[\frac{\partial N(E)}{\partial B}\right], \quad \sigma_H \in \mathcal{Z} \tag{30}$$

which expresses the conductance in terms of the dependence of the number of electronic states below the gap on the magnetic field strength. Being able to handle a dense set of rational fields, we obtain σ_H directly from the band-structure calculations at two sufficiently close values of magnetic flux that share the gap.

IV. RESULTS

Let us now turn to the results obtained applying the above formalism to antidot superlattices. We begin our presentation by contrasting the essential features of the energy spectra of non-interacting electrons for two distinct choices of the periodic potential: (i) smooth potentials described by a few lowest Fourier components and (ii) potentials created by very narrow and steep antidots whose

Fourier spectrum includes many high-**G** components. In the extreme limits of the two cases we deal with a cosine-like modulation and a lattice of δ-functions, respectively, and obtain some analytical results. In the second case, we record the property of the energy spectrum to contain split-off levitating subbands and proceed to consider realistic antidots of finite radius and include the effects of electron-electron interaction.

A. Weak cosine modulation

We now concentrate on the lattices of perfect square symmetry and describe the potential modulation by setting the four lowest Fourier components to equal strength $v(0,\pm1) = v(\pm1,0) \equiv v$. When the potential is also weak, the different Landau levels are not coupled ($B_{nn'} \propto \delta_{nn'}$) and all four non-vanishing coefficients $B_{nn}(\mathbf{G})$ are equal and evaluate to

$$b_n \equiv B_{nn}(0,\pm1) = B_{nn}(\pm1,0) = e^{-\pi N/(2L)} L_n\left(\frac{\pi N}{L}\right). \tag{31}$$

Consequently, b_n can be moved outside the sum over **G** in the potential-energy term of Eq. (25) as a prefactor, and thus it will influence only the overall band widths. The internal subband structure within each band will be given by the rest of the summation which we carry out explicitly. For the sake of convenience, we redefine the phases of the wave functions according to $\varphi_l(\mathbf{q}) \to \varphi_l(\mathbf{q})\exp(2\pi i q_1 l/L)$. Then the potential energy term reduces to $v b_n \delta_{nn'} \Xi_{ll'}$, the matrix Ξ containing the following non-zero matrix elements

$$\begin{aligned} \Xi_{ll} &= 2\cos\left[\frac{2\pi}{L}(l - Nq_2)\right], \\ \Xi_{lm} &= \Xi^*_{ml} = \exp\left(2\pi i \frac{N}{L} q_1\right) \delta^{\bmod L}_{l+N,m}. \end{aligned} \tag{32}$$

Renumbering the rows and columns of this matrix according to[30] $l = N\lambda \bmod L$ it can be cast into the form

$$\begin{aligned} \Xi_{\lambda\lambda} &= 2\cos\left[2\pi \frac{N}{L}(\lambda - q_2)\right] \\ \Xi_{\lambda\mu} &= \Xi^*_{\mu\lambda} = \exp\left(2\pi i \frac{N}{L} q_1\right) \delta^{\bmod L}_{\lambda+1,\mu} \end{aligned} \tag{33}$$

allowing for the following interpretation. As depicted in Fig. 1, one deals with a 1D chain of lattice sites whose energies are modulated by a cosine function

of period L/N. Neighbouring sites are coupled by hopping matrix elements of unit absolute magnitude and incorporating a phase $\Delta = 2\pi N q_1/L$.

The matrix Ξ embodies the simplest model describing commensurability-related phenomena equivalently to the Harper's equation. In the present case we encounter the commensurability between the unit lattice site spacing and L/N site energy modulation period which leads to the splitting of each Landau band into L subbands. This observation completes the demonstration of how our model reduces to previously known simple models.[6] For the sake of reference, we also need to quote some results. Thus, in Fig. 2 we show the relative widths of the subbands together with the QH currents carried by each of them for a few flux values close to $L/N = 3$. The important point to note is that the physical requirement for the bands to evolve continuously as a function of magnetic field leads to the clustering of the subbands into closely packed groups denoted by 'A', 'B' and 'C' whose net QH conductances equal $0, 1$ and 0, respectively. When the commensurate flux deviates from the value $L/N = 3/1$, the three clusters develop a fine structure of subbands carrying QH currents different from 0 or 1. We note that these subbands and subgaps separating them are narrow and thus difficult to resolve. However, the subband structure can be quite different in a periodic lattice whose potential is steep and thus possesses a broad Fourier spectrum.

B. δ-function antidot lattice

We start by considering integer fluxes L (i. e. $N = 1$), while the discussion of the general case of rational fluxes follows later. The periodic lattice is composed of antidots modelled by δ-functions, thus

$$v(\mathbf{r}) = v_0 \Omega \sum_{\mathbf{R}} \delta(\mathbf{r} - \mathbf{R}), \quad v(\mathbf{G}) \equiv v_0 \tag{34}$$

in the real and reciprocal space, respectively. Here v_0 is the strength of an antidot and Ω is the unit-cell area. Calculating the matrix elements of potential (34) in the symmetry-adapted basis (26) we find

$$\begin{aligned} &\int_{-\infty}^{\infty} dx \int_{-\infty}^{\infty} dy\, \psi^*_{nl}(\mathbf{q}|\mathbf{r}) v(\mathbf{r}) \psi_{n'l'}(\mathbf{q}'|\mathbf{r}) \\ &= v_0 \Omega \delta(q_1 - q_1') \delta(q_2 - q_2') \psi^*_{nl}(\mathbf{q}|0) \psi_{n'l'}(\mathbf{q}|0). \end{aligned} \tag{35}$$

Thus we see that at each point in MBZ the matrix of the potential energy factorizes into an outer product of a vector with itself. Such a matrix has only one non-zero eigenvalue.

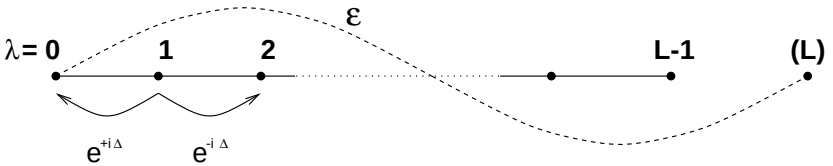

FIG. 1: A 1D chain of L lattice sites with periodic boundary conditions. The site energies are modulated according to the law $\varepsilon_\lambda = 2\cos[2\pi N(\lambda - q_2)/L]$ so that one has an integer number (N) of full periods per L sites. The hopping matrix elements include a phase $\Delta = 2\pi N q_1/L$.

In the limit of weak potentials v_0 the coupling between different Landau levels can be neglected. Then we find the energies of the states with respect to the common energy $n + 1/2$ in the n-th level[31] by diagonalizing just the $L \times L$ potential energy matrix $v_{ll'} = v_0 \Omega\, \psi^*_{nl}(\mathbf{q}|0)\psi_{nl'}(\mathbf{q}|0)$. In view of its special structure all but one of its eigenvalues equal zero and the only nonvanishing one is obtained as the trace

$$\varepsilon_n(\mathbf{q}) = v_0 \Omega \sum_{l=0}^{L-1} |\psi_{nl}(\mathbf{q}|0)|^2. \tag{36}$$

Thus we conclude that in the perturbative regime the lattice of δ-antidots will split off exactly one subband from each Landau band containing L subbands in total. This in turn implies that the degenerate subband wave-functions rearrange themselves in such a way that $L - 1$ of them have their zeros at the locations of antidots so that they are not affected by the zero-range antidot potential. Therefore, even beyond the perturbative regime one will still observe only one split-off subband, however, its energy will not scale linearly with the potential strength but rather level off. We display both the linear dispersion in the perturbative regime and the cross-over to the "saturation" region of the band energies in the panel (a) of Fig. 3 for a magnetic flux $L = 4$.

Another interesting feature shown in Fig. 3 (a) is that the lower edge of the levitating subband in the third ($n = 3$) Landau band stays pinned exactly at the value $\varepsilon = 3.5$ regardless of the potential strength. This is a consequence of the fact that in the present case at the centre of MBZ (which corresponds to the band minimum) *all four* subband functions have their zeros at the exact locations of the antidots and thus are not affected by the potential at all. On the contrary, at the corner of MBZ ($q_1 = q_2 = 1/2$, top of the band) all four unperturbed functions place their maxima at the locations of the antidots.

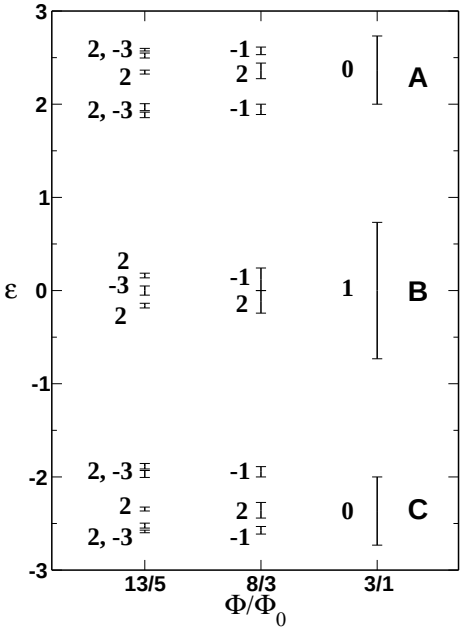

FIG. 2: The structure of the energy spectrum and distribution of quantum Hall currents among the subbands for several magnetic flux values close to $L/N = 3$. The continuity of the subbands leads to the "hiding" of nontrivial QH integers in deep levels of the recursive subband structure.

Therefore, the resulting energy (36) is large, and the band is broad.

However, panel (b) displays the behaviour of the same bands when the potential strength and the magnetic flux penetrating a unit cell are kept fixed at the respective values $v_0 = 0.15$ and $L = 4$, but the shape of the lattice is varied by continuously distorting it into a rectangular (rather than square) one. We observe that at some given ratio of the two lattice constants the width of the third band shrinks down to zero. On the contrary, the width of the levitating subband originating from the lowest Landau level increases quite substantially starting from what was a very narrow band in a square lattice. In conclusion, the subband wave-functions exhibit a certain rigidity and thus the effect of a periodic δ-function lattice on the energy spectrum depends on the relative distribution of the lattice sites, on one hand, and maxima and nodes of the states, on the other.

The levitating subbands contain a magnetic field independent number of states and therefore carry no net QH current. However, for rational fluxes ($N \neq 1$) each of these bands splits into N smaller subbands. Being able to resolve such splittings inside a levitating band one would detect some interesting

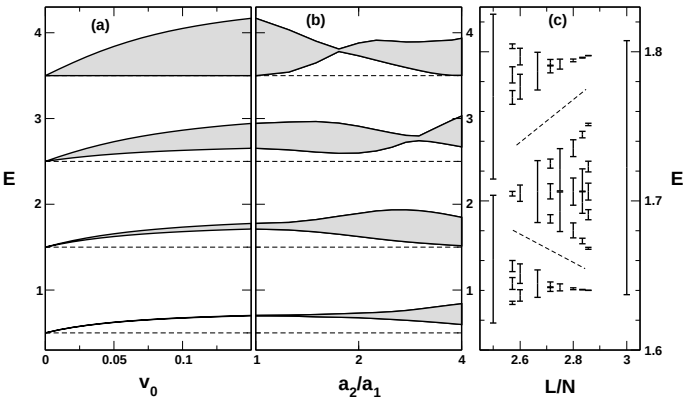

FIG. 3: The structure of the energy spectrum in a δ-antidot lattice. Panel (a) shows the evolution of the split-off levitating subbands at a fixed integer magnetic flux $\Phi = 4\Phi_0$ as a function of potential strength. The energies are measured in units $\hbar\omega_c = 2.86$ meV. The rest 3 subbands in each Landau band have zero widths and are positioned at the unperturbed energies $n + 1/2$ denoted by dashed lines. In (b) we display the band-widths as a function of the ratio of two lattice constants (logarithmic scale) at fixed values of $v_0 = 0.15$ and $L = 4$. (c) shows the dispersion against the magnetic field of the levitating subband belonging to the $n = 1$ Landau level for a fixed value of the potential $v_0 = 0.125$ in a square lattice. We look at the vicinity of $L/N = 3/1$ and correspondingly measure energies in units $\hbar\omega_c = 2.14$ meV.

QH currents. In Fig. 3 (c), we show the fine structure of a levitating subband in the vicinity of commensurate flux $L/N = 3$. The three most conspicuous clusters separated by large gaps (denoted by dashed lines) carry QH currents equal to $-1, 2, -1$.

Comparing the discussed structure of the spectrum to that found in the limit of smooth potentials we can describe it as the magnification of the energy scale of the topmost cluster of subbands denoted by 'A' in Fig. 2 while the widths of clusters 'B' and 'C' shrink down to zero. This redistribution of band-widths can be used as a way to *systematically* increase the widths of certain subbands and gaps in the "butterfly"-like bandstructure when trying to detect them experimentally, in particular, in a QH measurement. We suggest that broad levitating subbands could be most easily detected in moderate ($L/N \approx 3 - 6$) magnetic fields. In weaker fields, the electronic states are poorly localized and thus they are averaging the potential landscape over a large area of a unit cell. Therefore,

even very narrow antidots will fail to differentiate between various degenerate subband states in a Landau level. On the other hand, in stronger magnetic fields the states in a levitating subband become too strongly localized and have vanishingly small overlaps with their neighbours in adjacent cells which results in very small band-widths. Moreover, as we discussed above, the widths and positions of the levitating subbands may be very sensitive to the geometry of the lattice.

C. Realistic antidot superlattices

With the discussion of limiting cases in the background, we proceed to the consideration of superlattices of finite-radius antidots and also include the electron-electron interaction. We set the electron density to $n_s = 10^{11}\mathrm{cm}^{-2}$. The lattice is chosen to be of perfect square symmetry, and the antidots are modelled by gaussians of effective radius b. Thus, in the real and reciprocal space, respectively,

$$v(\mathbf{r}) = \sum_{\mathbf{R}} v_0\, e^{-(\mathbf{r}-\mathbf{R})^2/b^2}, \quad v(\mathbf{G}) = v_0 \alpha e^{-\alpha\pi g^2}, \tag{37}$$

here $g = (g_1^2 + g_2^2)^{1/2}$ and $\alpha = \pi b^2/a^2$ denotes the fraction of a cell area occupied by an antidot.

The panels (a) and (b) of Fig. 4 show the subband structure in the first ($n = 1$) Landau band for the magnetic flux $L/N = 3$. We plot the allowed energy values in the three resulting subbands as a function of the effective electron-electron interaction strength λ which is "turned on" from 0 (free electrons) to 1 (actual value). The two panels compare the spectra obtained for two different sizes of antidots: $\alpha = 0.1$ and 0.2 in the panels (a) and (b), respectively.

We see that the bands become narrower as the interaction strength increases. The reason for this lies in the fact that the band-widths are set by a competition between the band-narrowing effect due to the magnetic field and the broadening of the bands by the periodic potential. The electronic screening effectively reduces the strength of the periodic potential and consequently leads to narrower bands. The importance of the screening can be judged upon from the fact that the band-widths change ≈ 4 times.

However, in a lattice composed of narrow antidots ($\alpha \leq 0.1$) the strong screening effects fail to introduce qualitative changes into the structure of the energy spectrum since the Coulomb potential in reciprocal space behaves as $\propto |\mathbf{G}|^{-1}$ and becomes inefficient at high $\mathbf{G}$'s. Thus, in Fig. 4 (a) we see that even in the presence of electron-electron interaction the nature of the spectrum retains

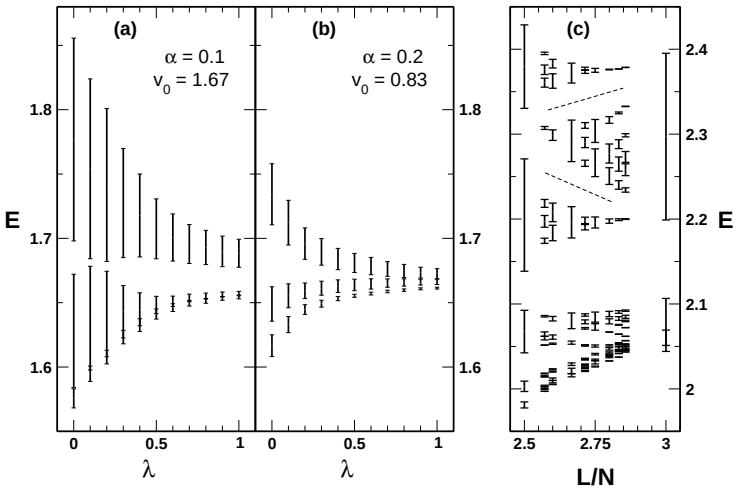

FIG. 4: The energy spectra of interacting electrons in units $\hbar\omega_c = 2.14$ meV. The panels (a) and (b) show the behaviour of the subbands in the first Landau band as a function of effective interelectron interaction strength λ for two different choices of periodic potential (see parameter values in the figure). The panel (c) shows the subband structure versus magnetic flux for fully interacting electrons and $\alpha = 0.1$, $v_0 = 6.67$.

features characteristic of a narrow-antidot lattice. At $\lambda \approx 0.15$ we find a closing and reopening of the gap separating the levitating subband from the other two. However, it does not lead to redistribution of QH currents; the net current in the topmost band always equals 0. In panel (c), we plot the energy bands versus the commensurate magnetic flux for the interacting electrons ($\lambda = 1$). Here the value of v_0 is 4 times larger than that in panel (a) in order to maintain the overall width of the bands. As in Fig. 3, the three most conspicuous clusters of subbands (delimited by dashed lines) within the levitating band carry QH currents equal to $-1, 2, -1$ and are still separated by sufficiently broad gaps.

When the size of the antidots is increased to $\alpha = 0.2$ [panel (b)] the electronic screening becomes capable of transforming the steep bare periodic potential into a rather smooth self-consistent potential. Thus, we see that at the effective interaction around $\lambda \approx 0.3$ the nature of the subband structure cross-over to that characteristic of smooth potentials, i. e. the wide gap separating a levitating subband disappears.

The inclusion of exchange and correlation effects beyond the mean-field level would introduce certain *quantitative* modifications into the details of the self-consistent potential and the exact positions of the calculated bands, however, the essential conclusions regarding the nature of the energy spectrum and its stability with respect to strong electron-electron interactions follow from the inefficiency of screening of high Fourier components of the external potential and would remain unaltered.

V. SUMMARY

In summary, we developed a theory to describe electrons moving in competing periodic potentials and magnetic fields which enabled us to treat interacting electrons at a dense set of magnetic field values. Considering the electron spectra in superlattices composed of steep antidots we identified a cluster of sufficiently broad and well isolated subbands. Such subbands can be more easily resolved in a measurement, moreover, their internal structure may reveal a rich spectrum of QH integers.

ACKNOWLEDGMENTS

We acknowledge valuable discussions with Prof. Algirdas Matulis and Dr. Carl-Olof Almbladh. One of us (P.J.) was supported by the Swedish Natural Science Research Council (NFR).

APPENDIX A: SYMMETRY PROPERTIES OF THE STATES

The transformation properties of the states with respect to translations are derived by commuting the magnetic-translation operators (4) and a general projection operator

$$P^{\mathbf{q}}_{jk} = \sum_{\mathbf{R}} [D^0_{jk}(\mathbf{R}) e^{-i\mathbf{q}\cdot\mathbf{R}}]^* T_M(\mathbf{R}), \tag{A1}$$

which projects out the component belonging to the k-th row of the representation $\mathbf{q}$ and then generates the partner belonging to the j-th row. After some straightforward algebra we obtain

$$\begin{aligned} T_M(-\mathbf{a}_1) P^{\mathbf{q}}_{jk} &= e^{2\pi i [q_1 - (L/N)(j-1)]} P^{\mathbf{q}}_{jk}, \\ T_M(-\mathbf{a}_2) P^{\mathbf{q}}_{jk} &= e^{2\pi i q_2} P^{\mathbf{q}}_{j+1,k}. \end{aligned} \tag{A2}$$

The first line in Eq. (A2) defines the equivalent of the usual Bloch condition, while the second one equips us with a rule for generation of all partner functions from the first one

$$\psi_j(\mathbf{q}) = e^{-2\pi i q_2 (j-1)} T_M[-(j-1)\mathbf{a}_2]\psi_1(\mathbf{q}). \tag{A3}$$

Joining N adjacent cells along the $\mathbf{a}_2$ direction one constructs a supercell enclosing an *integer* flux and recovers a Bloch-like relation

$$T_M(N\mathbf{a}_2)\psi_j(\mathbf{q}) = e^{-2\pi i N q_2}\psi_j(\mathbf{q}). \tag{A4}$$

APPENDIX B: ON THE PROJECTION OPERATORS

We start by inserting the expression of irreducible representation (17) and the magnetotranslation operator (10) into the definition of the projection operator (18). In the resulting sum over lattice sites, the summations over the indices n_1 and n_2 decouple. The latter one can be carried out explicitly thus transforming a sum of exponentials into a series of δ-functions. The answer reads

$$\begin{aligned} P_{11}^{\mathbf{q}} &= \frac{a_{1x}}{L} \sum_{m=-\infty}^{\infty} \delta\left[\eta + (Nq_2 - m)\frac{a_{1x}}{L}\right] \\ &\times \sum_{n=-\infty}^{\infty} e^{2\pi i n q_1} e^{-i a_{1x} a_{1y} n^2/2} e^{i a_{1y} n \eta} T_\eta(n a_{1x}). \end{aligned} \tag{B1}$$

Consider first the case $L = 1$. Acting on a given seed function the translation operator T_η will produce its shifted replicas of period a_{1x} which will be subsequently filtered through a series of δ-functions of the same spacing. Thus, in order to be able to project out nonvanishing components for any subspace it suffices to choose a seed function that is non-zero (we set it equal to a constant) only in an interval of length a_{1x}. Consequently, the final expression for the states (19) contains just a single sum and not double series.

In the case $L \neq 1$ the spacing between δ-functions in (B1) becomes L times finer and leads to the appearance of L distinct basis functions of the same symmetry.

Our procedure of constructing the symmetry-adapted basis bears some resemblance to that due to Ferrari.[19] The "double series" in Ferrari's Eq. (45) is the equivalent of our projection operator. However, the corresponding expression for the states given in Eq. (46) of Ref. 19 still involves a double sum. Moreover, our approach based on group theory handles the cases $L \neq 1, N \neq 1$ in a uniform way without any need for introduction of a finer paving inside a lattice cell or explicit construction of supercells.

REFERENCES

* Electronic address: egidijus@teorfys.lu.se

[1] D. Weiss, K. v. Klitzing, K. Ploog, and G. Weimann, Europhys. Lett. **8**, 179 (1989); R. R. Gerhardts, D. Weiss, and K. v. Klitzing, Phys. Rev. Lett. **62**, 1173 (1989); R. W. Winkler, J. P. Kotthaus, and K. Ploog, *ibid.* **62**, 1177 (1989).

[2] D. Weiss, K. von Klitzing, K. Ploog, and G. Weimann, Surf. Sci. **229**, 88 (1990).

[3] R. R. Gerhardts, D. Weiss, and U. Wulf, Phys. Rev. B **43**, 5192 (1991).

[4] D. Pfannkuche D and R. R. Gerhardts Phys. Rev. B **46**, 12 606 (1992).

[5] M. Ya. Azbel', Zh. Eksp. Teor. Fiz. **46**, 929 (1964) [Sov. Phys. JETP **19**, 634 (1964)].

[6] D. R. Hofstadter, Phys. Rev. B **14**, 2239 (1976).

[7] T. Schlösser, K. Ensslin, J. P. Kotthaus, and M. Holland, Semicond. Sci. Technol. **11**, 1582 (1996).

[8] D. J. Thouless, M. Kohmoto, M. P. Nightingale, M. den Nijs, Phys. Rev. Lett. **49**, 405 (1982); M. Kohmoto, Ann. Phys. (NY) **160**, 343 (1985).

[9] P. Středa, J. Phys. C: Solid State Phys. **15**, L717 (1982); P. Středa, *ibid* L1299 (1982).

[10] C. Albrecht, J. H. Smet, K. von Klitzing, D. Weiss, V. Umansky and H. Schweizer, Phys. Rev. Lett. **86**, 147 (2001).

[11] P. G. Harper, Proc. Phys. Soc. London Sect. A **68**, 874 (1955).

[12] D. Langbein, Phys. Rev. **180**, 633 (1969).

[13] A. Rauh, Phys. Status Solidi B **69**, K9 (1975).

[14] R. E. Peierls, Z. Phys. **80**, 763 (1933).

[15] A. S. Alexandrov and H. Capellmann, Phys. Rev. Lett. **66**, 365 (1991).

[16] G. Petschel and T. Geisel, Phys. Rev. Lett. **71**, 239 (1993).

[17] D. Weiss, M. L. Roukes, A. Menschig, P. Grambow, K. von Klitzing, and G. Weimann, Phys. Rev. Lett. **66**, 2790 (1991); R. Fleischmann, T. Geisel, and R. Ketzmerick, *ibid.* **68**, 1367 (1992).

[18] V. Gudmundsson and R. R. Gerhardts, Phys. Rev. B **52**, 16 744 (1995); V. Gudmundsson, *ibid.* **57**, 3989 (1998).

[19] R. Ferrari, Phys. Rev. B **42**, 4598 (1990). For an example of application of the Ferrari basis see H. Silberbauer J. Phys. C **4**, 7355 (1992).

[20] E. Brown, Phys. Rev. **133**, A1038 (1964); J. Zak, *ibid.* **134**, A1602 (1964); J. Zak, *ibid.* A1607 (1964).

[21] H.-J. Schellnhuber and G. Obermair, Phys. Rev. Lett. **45**, 276 (1980); G. M. Obermair and H.-J. Schellnhuber, Phys. Rev. B **23**, 5185 (1981); H.-J. Schellnhuber, G. M. Obermair, and A. Rauh, *ibid.* **23**, 5191 (1981).

[22] H.-J. Schellnhuber, Phys. Rev. B **25**, 2358 (1982).

[23] E. Anisimovas and P. Johansson, Phys. Rev. B **60**, 7744 (1999).

[24] M.-C. Chang and Q. Niu, Phys. Rev. B **53**, 7010 (1996).

[25] D. Springsguth, R. Ketzmerick, and T. Geisel, Phys. Rev. B **56**, 2036 (1997).

[26] M. Hamermesh, *Group Theory and its Application to Physical Problems*, (Dover, New York, 1989), Chap. 12.

[27] From here on we use the notation $\delta_{ij}^{\mathrm{mod}\ p}$ to denote a "modulo Kronecker delta" which equals 1 if i and j are equal or differ by a multiple of p, and vanishes otherwise.

[28] C.-O. Almbladh, private communication. Different variations of this technique are commonly used in band-structure calculations.

[29] I. Dana, Y. Avron, and J. Zak, J. Phys. C: Solid State Phys. **18**, L679 (1985); Q. Niu, D. J. Thouless, and Y.-S. Wu, Phys. Rev. B **31**, 3372 (1985).

[30] Since N and L are mutual primes, such a renumbering is always possible. Note also that in this subsection we number the matrix indices from 0 to $L-1$.

[31] We number Landau levels starting with zero for the lowest one.

Tunneling spectroscopy of modulated two-dimensional electron systems

Egidijus Anisimovas*
Division of Solid State Theory, University of Lund, Sölvegatan 14A, S-223 62 Lund, Sweden

We calculate the tunneling current between two parallel modulated two-dimensional electron systems in tilted magnetic fields. Magnetic crystal momentum is used to enumerate the electronic states in the layers, and the effect of the *in-plane* component of the magnetic field is described in terms of a magnetic crystal momentum shift during the tunneling transition. The results indicate a possibility to perform a spectroscopic investigation of the electronic states by means of electron tunneling. In particular, we discuss the measurement of the miniband dispersions, the shape of the Fermi area and the density of states in the layers.

I. INTRODUCTION

The study of the physics of two-dimensional electron gases and laterally structured two-dimensional electron systems (2DES), often placed into strong magnetic fields, has now evolved into a broad subfield of condensed matter physics.[1] During the last few decades the research on effectively two-dimensional systems, both at the theoretical and the experimental level, has diversified into many subbranches and led to a number of major discoveries. Among them, the study of quantum transport[2] resulted in the observation of conductance quantization[3] and the integer quantum Hall effect.[4]

In particular, much attention has been devoted to extended 2DES whose potential landscape is periodically modulated in one or both lateral directions. Such systems set an example of an artificial solid possessing an artificial bandstructure. In the presence of a commensurate perpendicular magnetic field, the structure of the energy spectrum of an electron moving in a bidirectionally periodic potential displays a highly intricate self-similar pattern of subbands resembling a butterfly which has long intrigued theorists' mind.[5,6] Only a few years ago, transport experiments have succeeded in delivering the evidence of the formation of the butterfly-like subband structure. Schlösser and co-workers[7] observed a splitting of the Shubnikov-de Haas maximum in the longitudinal magnetoresistance oscillations revealing the underlying splitting of a Landau

band into a number of subbands. More recently, the subband structure was identified in the integer quantum Hall effect measurement.[8]

Another encounter of novel physics discovered in modulated 2DES is the Weiss oscillations resulting from the commensurability of the electron cyclotron radius and the potential modulation period.[9] The widths of the broadened Landau bands depend on the average potential seen by an electron over the extension of its wave-function. This fact results in $1/B$-periodic oscillations of the magnetoresistance thus directly reflecting the bandstructure features in a measurement.

Unfortunately, a direct observation of the bandstructure in an optical experiment, paralleling the usual means of investigation in conventional solid state physics, is not feasible. Most of the optical experiments have been performed closer to the semiclassical regime[10] and concentrated on the collective modes rather than the electronic structure measurements.

However, a possible way of accessing the bandstructure properties of 2DES is offered by a 2D-2D tunneling between two parallel two-dimensional electronic layers. Since a number of involved technological complications have been successfully overcome more than a decade ago,[11] the tunneling between parallel layers has become a handy tool of investigation of electronic properties of 2D electron systems. It has been shown[12] that the tunneling current directly probes the spectral function of a 2D electron, and the electronic life-times have been investigated.[12,13] The data obtained by this technique is often complementary to that available from measurements of in-plane transport properties. In particular, it delivers valuable information on the electron-electron collision rate which is very difficult to extract from the in-plane transport data due to the total momentum conservation during such collisions.[13]

The electronic layers used in the experimental work usually possess a high degree of uniformity; therefore, the tunneling events can be described in the momentum space. The presence of an in-plane magnetic field component provides a means of tuning the relative momenta of the final and initial states connected by the transition.

Recent theoretical work considered tunneling between two unmagnetized[14] and magnetized[15] uniform two-dimensional electron gases. The latter work was based on the description of the electronic states in terms of the usual Landau-gauge solutions and the effect of the in-plane magnetic field was interpreted in terms of shifts of the centroid of the electronic wave-function. The obtained results revealed quantum oscillations in the tunneling conductance. In the present paper, we introduce the description of the electron states and tunneling process in terms of the magnetic crystal momentum defined in a magnetic Brillouin zone (MBZ). This allows us to treat both uniform and modulated in one or two

lateral directions 2DES using a unified approach. In particular, we concentrate on the possibilities to use the data provided by a tunneling conductance measurement to reveal the information about the underlying electronic structure of a modulated electron system.

The paper is organized in the following way. In Sec. II, we present a review of the description of the electron states in a periodic potential an a *perpendicular* magnetic field in terms of the magnetic crystal momentum. Sec. III discusses the modifications of the electronic states due to the presence of an *in-plane* component of the magnetic field, and Section IV deals with the description of electron tunneling in this language. The two following Sections, V and VI, present the results obtained for the tunneling between two parallel electronic layers modulated in one and two lateral directions, respectively. We conclude with a summarizing Sec. VII.

II. ELECTRONIC STATES IN THE LAYERS

We describe the individual electronic layers as systems of interacting two-dimensional electrons moving in a periodic superlattice potential $v(\mathbf{r})$ and a perpendicular uniform magnetic field $\mathbf{B}$ given in terms of its symmetric-gauge vector potential $\mathbf{A} = \mathbf{B} \times \mathbf{r}/2$. It is convenient to work in the dimensionless units set by the magnetic field strength. Thus, we use the cyclotron energy and the magnetic length

$$\hbar\omega_c = \frac{\hbar eB}{mc}, \quad l_c = \sqrt{\frac{\hbar c}{eB}} \tag{1}$$

as the energy and length units, respectively. The single-particle Hamiltonian in these units reads

$$H = \frac{1}{2}\left[\left(p_x - \frac{y}{2}\right)^2 + \left(p_y + \frac{x}{2}\right)^2\right] + v(\mathbf{r}), \quad v(\mathbf{r}) = v(\mathbf{r} + \mathbf{R}), \tag{2}$$

here the potential $v(\mathbf{r})$ stands for the self-consistent effective single-particle potential which we calculate in the Hartree approximation. The periodic lattice is spanned by the vectors $\mathbf{R} = n_1\mathbf{a}_1 + n_2\mathbf{a}_2$, and its reciprocal counterpart by $\mathbf{G} = g_1\mathbf{b}_1 + g_2\mathbf{b}_2$. The vectors $\mathbf{a}_{1,2}$ and $\mathbf{b}_{1,2}$ are related in the usual fashion $\mathbf{a}_i \cdot \mathbf{b}_j = 2\pi\delta_{ij}$, and $n_{1,2}$ and $g_{1,2}$ are integer indices. We represent the periodic potential in terms of its Fourier decomposition

$$v(\mathbf{r}) = \sum_{\mathbf{G}} v(\mathbf{G}) \mathrm{e}^{i\mathbf{G}\cdot\mathbf{r}}. \tag{3}$$

The scope of the present paper is restricted to rectangular lattices so that $\mathbf{a}_1$ and $\mathbf{b}_1$ are parallel to the x-axis, while $\mathbf{a}_2$ and $\mathbf{b}_2$ point along the y direction. We also confine our attention to *integer* magnetic fields, i. e. such that the magnetic flux penetrating a unit cell is an integer multiple of the magnetic flux quantum $\Phi_0 = ch/e$. In the dimensionless units, this condition translates into the following relation for the unit-cell area

$$a_1 a_2 = 2\pi L, \quad L \in \mathcal{Z}. \tag{4}$$

The above description is tailored to the needs of bidirectionally modulated 2DES; when the potential modulation is applied only in one (say, x) direction we artificially introduce an *empty* lattice in the other direction with the period a_2 chosen so that the unit cell encloses exactly one flux quantum, thus setting $L = 1$ in Eq. (4).

Since the Hamiltonian (2) is invariant with respect to discrete translations by a lattice vector $\mathbf{R}$, we classify its states according to their symmetry properties. The magnetic translation operator in the symmetric gauge is given by[20,21]

$$\begin{aligned} T_M(\mathbf{R}) &= \exp\left[-in_1 a_1 \left(p_x + \frac{y}{2}\right) + in_2 a_2 \left(p_y - \frac{x}{2}\right)\right], \\ \text{for} \quad \mathbf{R} &= n_1 \mathbf{a}_1 + n_2 \mathbf{a}_2. \end{aligned} \tag{5}$$

The electronic states satisfy the magnetic Bloch condition

$$T_M(\mathbf{a}_{1(2)})\psi_{\mathbf{q}} = \mathrm{e}^{-i\mathbf{a}_{1(2)}\cdot\mathbf{q}}\psi_{\mathbf{q}} \tag{6}$$

with the values of the magnetic crystal momentum $\mathbf{q} = q_1\mathbf{b}_1 + q_2\mathbf{b}_2$ restricted to the first magnetic Brillouin zone (MBZ) chosen as $0 \le q_1, q_2 < 1$.

It is convenient to perform a canonical coordinate transformation[20–22] to a new set of degrees of freedom – the generalized coordinates ξ and η, and the respective conjugate momenta

$$\begin{aligned} \xi &= p_y + x/2, \quad p_\xi = p_x - y/2, \\ \eta &= -p_y + x/2, \quad p_\eta = p_x + y/2. \end{aligned} \tag{7}$$

In the new variables the Hamiltonian and the magnetic translation operator become

$$H_0 = \frac{1}{2}\left(p_\xi^2 + \xi^2\right) + \sum_{\mathbf{G}} v(\mathbf{G})\mathrm{e}^{i(G_x\xi - G_y p_\xi)}\mathrm{e}^{i(G_x\eta + G_y p_\eta)}, \tag{8}$$

$$T_M(\mathbf{R}) = \exp(-iR_x p_\eta + iR_y\eta), \tag{9}$$

thus making the role of the new degrees of freedom apparent. The kinetic energy part is transformed into a harmonic oscillator in ξ corresponding to the "fast" motion quantized into the Landau levels, while the magnetic translations now act only on η. The periodic potential mixes the two degrees of freedom thus leading to the broadening of Landau levels into bands.

We solve the Hamiltonian by expanding electronic states $\psi(\mathbf{q}|\xi\eta)$ in terms of the symmetry-adapted basis functions[20–22]

$$\psi(\mathbf{q}|\xi,\eta) = \sum_{n=0}^{\infty}\sum_{l=0}^{L-1} a_{nl}\psi_{nl}(\mathbf{q}|\xi,\eta), \tag{10}$$

$$\psi_{nl}(\mathbf{q}|\xi,\eta) = \chi_n(\xi)\varphi_l(\mathbf{q}|\eta), \tag{11}$$

constructed as a product of the n-th harmonic oscillator function in ξ and a basis function of the $\mathbf{q}$-th irreducible representation of the magnetotranslation group in η

$$\varphi_l(\mathbf{q}|\eta) = \sqrt{\frac{2\pi}{a_2}} \sum_{m=-\infty}^{\infty} \mathrm{e}^{2\pi i m q_1}\delta\left(\eta - ma_1 + a_1\frac{q_2-l}{L}\right). \tag{12}$$

The subband index $l = 0,\ldots,L-1$ accounts for the presence of L linearly independent basis functions of the same symmetry. This fact manifests itself as the splitting of a Landau band into L subbands.

In the basis (11) the Schrödinger equation is transformed into an eigenvalue problem for each $\mathbf{q}$

$$\sum_{n'=0}^{\infty}\sum_{l'=0}^{L-1}\mathcal{M}_{nl;n'l'}a_{n'l'} = \epsilon a_{nl},$$

$$\mathcal{M}_{nl;n'l'} = \delta_{nn'}\delta_{ll'}\left(n+\frac{1}{2}\right) + \sum_{\mathbf{G}} v(\mathbf{G})B_{nn'}(\mathbf{G})A_{ll'}(\mathbf{q};\mathbf{G}), \tag{13}$$

whose solutions specify the state energies and the expansion coefficients a_{nl}. The product $B_{nn'}A_{ll'}$ denotes the matrix element of the product of exponential operators in (8). We find it convenient to separate the ξ- and η-dependent contributions. The expression for $B_{nn'}$ reads (for $n \geq n'$)

$$\begin{aligned} B_{nn'}(\mathbf{G}) &= B^*_{n'n}(-\mathbf{G}) = \int_{-\infty}^{\infty}\chi_n(\xi)\hat{X}(\mathbf{G}|\xi)\chi_{n'}(\xi)\,d\xi \\ &= e^{-iG_xG_y/2}\int_{-\infty}^{\infty}\chi_n(\xi)\chi_{n'}(\xi-G_y)e^{iG_x\xi}\,d\xi \end{aligned} \tag{14}$$

$$= \sqrt{\frac{2^{n'}n'!}{2^n n!}} e^{-(G_x^2+G_y^2)/4} (G_y + iG_x)^{n-n'} L_n^{n-n'} \left(\frac{G_x^2+G_y^2}{2} \right),$$

while $A_{ll'}$ is just a phase factor

$$A_{ll'}(\mathbf{q};\mathbf{G}) \;=\; \mathrm{e}^{(2\pi i/L)\left[g_1 g_2/2 + g_1 l + (q_1 g_2 - q_2 g_1) + q_1(l-l')\right]} \delta_{l',l+g_2 \bmod L}. \qquad (15)$$

III. IN-PLANE MAGNETIC FIELD

The above description of the electronic states in the layers is developed assuming that the magnetic field $\mathbf{B}$ is applied perpendicularly to the 2DES plane. We now consider the modifications arising from the presence of an additional in-plane component $\mathbf{B}^{\parallel}$. Still working in the same dimensionless units set by the strength of the perpendicular component, we describe the effects of the parallel component of the field by introducing an extra contribution to the vector potential $\mathbf{A}^{\parallel}$. We choose to write it in a Landau gauge chosen in such a way that the vector $\mathbf{A}^{\parallel}$ lies in the xy-plane, that is, $A_x^{\parallel} = -B_y^{\parallel} z$ and $A_y^{\parallel} = B_x^{\parallel} z$.

By virtue of this choice, the presence of the parallel magnetic field component does not affect the in-plane magnetic translations, and leads to the following modification of the single-particle Hamiltonian

$$H = \frac{1}{2}(p_\xi + \beta_y z)^2 + \frac{1}{2}(\xi - \beta_x z)^2 + v(\xi,\eta) + \frac{1}{2}p_z^2 + V(z) \quad \text{with} \quad \beta_{x,y} = \frac{B_{x,y}^{\parallel}}{B}. \qquad (16)$$

Here we make an explicit reference to the motion along the z direction leading to the formation of subbands. From Eq. (16) we see that, in view of its dependence on the z coordinate, the parallel magnetic field will couple the in-plane electronic motion to the z degree of freedom. The strength of this coupling is given by the matrix elements of the term $\beta_{x,y} z$ between the subband wave functions. As we will see later, in order to cover the whole area of MBZ in a tunneling measurement the maximum values of $B^{\parallel}$ have to be a few times larger than B. The matrix elements of z typically equal a fraction of the electron-layer thickness (of order 100 Å), let us remind it again, measured in the magnetic lengths $l_c \approx 250$ Å for $B \sim 1$ T. Thus we see that only for the highest values of the in-plane magnetic fields of interest the perturbation strength is threatening to reach values of order of unity, that is, comparable to the energy scale of the in-plane motion. Moreover, if the quantum well is symmetric the diagonal matrix elements of z will vanish due to symmetry and thus βz will have no effect in the first-order perturbation. Thus we conclude that the in-plane magnetic fields in the symmetric quantum wells can be assumed to have no effect on the

electronic states in the layers for most cases of interest. Therefore, we take $\mathbf{B}^{\parallel}$ into account only to the extent of the modification of the tunneling process.

Mathematically speaking, our approximation amounts to the assumption that the electronic layers are infinitesimally thin. Therefore, in the kinetic energy term of the Hamiltonian (16), it is legitimate to replace the variable z with its constant value z_0 at the exact location of the electronic layer. In the following, we will assume that the two electronic layers involved in the tunneling setup are placed at $z_0 = 0$ ('left') and $z_0 = \Delta z$ ('right'), respectively. Thus, the Hamiltonian of the left 2DES is not affected by the in-plane magnetic field at all, while the right one is modified by a *constant* vector potential $\mathbf{A}^{\parallel}(\Delta z)$. Thus the effect of the in-plane magnetic field on the electronic states in the right layer amounts to a gauge transformation

$$\psi(\mathbf{r})\Big|_{\mathbf{B}^{\parallel}} = \psi(\mathbf{r})\Big|_{0} \mathrm{e}^{-i\Delta\mathbf{k}\cdot\mathbf{r}}, \quad \Delta\mathbf{k} = \frac{e}{c\hbar}\mathbf{A}^{\parallel}(\Delta z). \tag{17}$$

IV. TUNNELING

We describe the electron tunneling between two parallel modulated 2DES using the usual stationary Hamiltonian approach.[16–18] The electron states in the two subsystems that are weakly coupled by a tunneling link are first calculated neglecting the presence of the link. Thus one introduces two sets of eigenstates – one for the 'left' Hamiltonian $H_L = K + V_L$, and another for the 'right' one $H_R = K + V_R$; here K is the kinetic energy operator, and $V_{L,R}$ denote the potential energies in the respective subsystems. The introduction of a tunneling link allows an electron to move in the potential of both subsystems. The full Hamiltonian $H = K+V_L+V_R$ is now not diagonal in the set of original 'left' and 'right' unperturbed states. It is common to represent the resulting non-diagonal Hamiltonian in the form[16]

$$H = \sum_r \epsilon_{rL} c^{\dagger}_{rL} c_{rL} + \sum_s \epsilon_{sR} c^{\dagger}_{sR} c_{sR} + \left\{ \sum_{rs} t_{sR,rL} c^{\dagger}_{sR} c_{rL} + \text{H. c.} \right\}, \tag{18}$$

where the indices r and s enumerate the states in the two subsystems. Assuming the approximate orthogonality[17] of the 'left' and 'right' states, it is customary to express the off-diagonal matrix elements in terms of the kinetic energy, subsequently converting them into matrix elements of the current operator.[18] However, we choose to work in terms of the potential energy matrix elements, thus evaluating the hopping terms in the tunneling Hamiltonian (18) as

$$t_{sR,rL} = \langle sR|V_R|rL\rangle \equiv \langle sR|V_L|rL\rangle. \tag{19}$$

The standard linear response calculation[19] leads to the following expression for the tunneling conductance at zero temperature

$$G = \frac{e^2}{\pi\hbar^3} \sum_{rs} |t_{rL,sR}|^2 A_{rL}(\mu) A_{sR}(\mu). \tag{20}$$

Here A denotes the single-particle spectral function and μ is the chemical potential. In this paper, we approximate A with a Lorentzian of a certain phenomenological width Δ, and postpone a microscopic calculation of the spectral properties of the 2DEG to a subsequent publication.

As discussed in the previous Section III, we assume that the electronic layers are infinitesimally thin on the scale of the relevant lengths. Therefore, the hopping matrix elements in the presence of an in-plane component of the magnetic field are given by

$$t_{sR,rL}(\Delta\mathbf{k}) = \langle sR|V_R\, \mathrm{e}^{i\Delta\mathbf{k}\cdot\mathbf{r}}|rL\rangle \equiv \langle sR|V_L\, \mathrm{e}^{i\Delta\mathbf{k}\cdot\mathbf{r}}|rL\rangle, \tag{21}$$

The extra gauge-transformation exponent in Eq. (21) depends only on x, y coordinates, while the quantum well potentials $V_{L,R}$ are functions of z. Thus, writing our states in the layers as a product of an in-plane part and a z-dependent form factor we arrive to the conclusion that the $\Delta\mathbf{k}$-dependence of the tunneling matrix element is of the form

$$t_{sR,rL}(\Delta\mathbf{k}) = t_0\, \langle \psi_R^{\nu}(\mathbf{q}) | \mathrm{e}^{i\Delta\mathbf{k}\cdot\mathbf{r}} | \psi_L^{\nu'}(\mathbf{q}') \rangle, \tag{22}$$

here t_0 is a constant resulting from the overlap of z-dependent form factors and the well potential; in our approximation, it does not depend on the parallel magnetic field. The notation $\psi_{L,R}^{\nu}(\mathbf{q})$ describes the lateral part of the electronic wave-function in terms of its magnetic crystal momentum $\mathbf{q}$, band number ν and the layer index L, R. As we will see later, the allowed values of momenta $\mathbf{q}$ and $\mathbf{q}'$ and the shift $\Delta\mathbf{k}$ are constrained by a selection rule.

The evaluation of the matrix element (22) is most easily carried out in the ξ, η coordinates. We use the expansion of the electronic states in the basis functions (11) and obtain

$$t_{sR,rL}(\Delta\mathbf{k}) = t_0 \sum_{nn'} \sum_{ll'} a_{nl,R}^{\nu *} a_{n'l',L}^{\nu'} \langle \psi_{nl,R}(\mathbf{q}) | \mathrm{e}^{i\Delta\mathbf{k}\cdot\mathbf{r}} | \psi_{n'l',L}(\mathbf{q}') \rangle. \tag{23}$$

Expressing

$$\Delta\mathbf{k}\cdot\mathbf{r} = \Delta k_x x + \Delta k_y y = \Delta k_x(\xi+\eta) + \Delta k_y(p_\eta - p_\xi) \tag{24}$$

the evaluation of the tunneling matrix element between the basis functions (11) closely parallels the calculation of the matrix elements $A_{ll'}$ and $B_{nn'}$ in (15) and (14). We separate the ξ- and η-dependent parts. The former introduces quantum-mechanical oscillations in $\Delta\mathbf{k}$, while the latter leads to a selection rule

$$\mathbf{q}' + \Delta\mathbf{k} = \mathbf{q} + \mathbf{\Gamma}, \quad \mathbf{\Gamma} = \gamma_1\mathbf{b}_1 + \gamma_2\mathbf{b}_2, \tag{25}$$

showing that the tunneling event takes place between two states in MBZ whose crystal momenta differ (up to a reciprocal lattice vector $\mathbf{\Gamma}$) by $\Delta\mathbf{k}$, the momentum shift due to the in-plane magnetic field. Collecting all the different contributions together we get

$$\begin{aligned}\langle\psi_{nl,R}(\mathbf{q})|\mathrm{e}^{i\Delta\mathbf{k}\cdot\mathbf{r}}|\psi_{n'l',L}(\mathbf{q}')\rangle &= B_{nn'}(\Delta\mathbf{k}) \\ \times\ & \mathrm{e}^{i\Delta k_x\Delta k_y/2}\mathrm{e}^{-i\Delta k_x a_1 q_2/L}\mathrm{e}^{i\Delta k_x a_1 l/L}\mathrm{e}^{-2\pi i\kappa q_1} \\ \times\ & \delta^{\mathrm{mod}\,L}_{l,l'+\gamma_2}\delta\left(q_1' + \frac{a_1}{2\pi}\Delta k_x - q_1 - \gamma_1\right)\delta\left(q_2' + \frac{a_2}{2\pi}\Delta k_x - q_2 - \gamma_2\right),\end{aligned} \tag{26}$$

where the coefficient $B_{nn'}(\Delta\mathbf{k})$ is identical to that given in (14) under the replacement $\mathbf{G} \to \Delta\mathbf{k}$. The two δ-functions express the conservation of the crystal momentum, and the modulo-Kronecker δ gives the selection rule for the subband indices. We see that the umklapp processes introduce shifts in l, and since the values of l are defined in an interval of length L this selection rule is also given up to a shift by a multiple of L. When such a shift is present it is also reflected in the last exponential on the second line of (26); here the integer κ is defined by $l' + \gamma_2 = l + \kappa L$. The last two exponential factors reflect the properties of the subband functions in MBZ, while the first two are inessential and can be dropped. When substituted into Eq. (23) they will not depend on the summation indices and give an overall phase which has no effect on the physical current.

V. UNIDIRECTIONALLY MODULATED SYSTEMS

Let us begin by discussing the tunneling conductance between two 2DES modulated along the x direction only. The unidirectional modulation potential is modeled by setting its Fourier components to $v(g1, g2) = \delta_{g_2,0}v(g_1)$. We introduce an empty lattice in the y direction so that the unit cell encloses one flux quantum, thus setting $L = 1$ and $l = 0$ in the equations of the previous Sections. As a result, the only subband function (12) becomes[23]

$$\varphi(\mathbf{q}|\eta) = \sqrt{\frac{2\pi}{a_2}}\sum_{m=-\infty}^{\infty}\mathrm{e}^{2\pi i m q_1}\delta(\eta - ma_1 + a_1 q_2), \tag{27}$$

and the subband mixing coefficient (15) now reads

$$A_{00}(\mathbf{q};\mathbf{G}) = \exp\left(-2\pi i q_2 \frac{g_1}{L}\right) \tag{28}$$

indicating that no dependence on q_1 enters the bandstructure problem. Therefore, the resulting bands will show dispersion only along q_2, while the quantum number q_1 will serve to enumerate distinct degenerate states. The correspondingly modified eigenvalue problem (13) will not show any dependence on l and q_1; its solution will provide us with the state expansion coefficients $a_n^\nu(q_2)$. Consequently, the tunneling matrix element given by Eqs. (23) and (26) will be modified to read

$$\begin{aligned} t_{sR,rL}(\Delta\mathbf{k}) &= t_0 \sum_{nn'} a_{n,R}^{\nu *} a_{n',L}^{\nu'} \langle \psi_{n,R}(\mathbf{q}) | \mathrm{e}^{i\Delta\mathbf{k}\cdot\mathbf{r}} | \psi_{n',L}(\mathbf{q}') \rangle, \\ \langle \psi_{n,R}(\mathbf{q}) | \mathrm{e}^{i\Delta\mathbf{k}\cdot\mathbf{r}} | \psi_{n',L}(\mathbf{q}') \rangle &= B_{nn'}(\Delta\mathbf{k})\, \mathrm{e}^{i\Delta k_x \Delta k_y/2} \mathrm{e}^{-i\Delta k_x a_1 q_2} \mathrm{e}^{-2\pi i \gamma_2 q_1} \\ &\times \delta\left(q_1' + \frac{a_1}{2\pi}\Delta k_x - q_1 - \gamma_1\right) \delta\left(q_2' + \frac{a_2}{2\pi}\Delta k_x - q_2 - \gamma_2\right). \end{aligned} \tag{29}$$

To illustrate the results, we first consider a double-layer system composed of two *identical* layers. We set the superlattice period to $a_1 = 2\,000$ Å, the interlayer separation to $\Delta z = 250$ Å, and the electron density in each of the layers to $n_s = 10^{11}\,\mathrm{cm}^{-2}$. Applying a perpendicular magnetic field of the strength 0.86 T we set the magnetic length to $l_c = 276$ Å and the cyclotron energy to 1.49 meV. The commensurate lattice constant in the y direction equals $a_2 = 240$ Å, and the Landau-level filling factor is $\nu_L = 2.4$. Then the in-plane magnetic field strength needed to induce a crystal momentum shift by a half of the extension of MBZ in the interesting q_2 direction will equal $B_y^{\parallel} = 3.43$ T, that is $\beta_y = 4$.

Since the energy bands show dispersion only in one, q_2, direction, the resulting Fermi area (the part of MBZ covered by the occupied electronic states in the partially filled second Landau band) is a stripe parallel to the $\mathbf{b}_1$ direction. The tunneling of electrons is constrained by the energy and momentum conservation and thus can only occur between the states lying on the boundaries of the Fermi area. Whenever the displacement of the Fermi areas of the two layers relative to each other by the in-plane magnetic field is such that their boundaries are brought into correspondence, one is expecting to observe a bandstructure-related peak in the conductance.

Figure 1 shows the dependences of the tunneling current on the strength of the in-plane magnetic field. Panel (a) presents the results obtained in the case when the magnetic field is applied in the x direction and thus shifts the q_1 component of the electron crystal momentum. The bands are dispersionless in this direction, therefore, there are no bandstructure induced effects in the

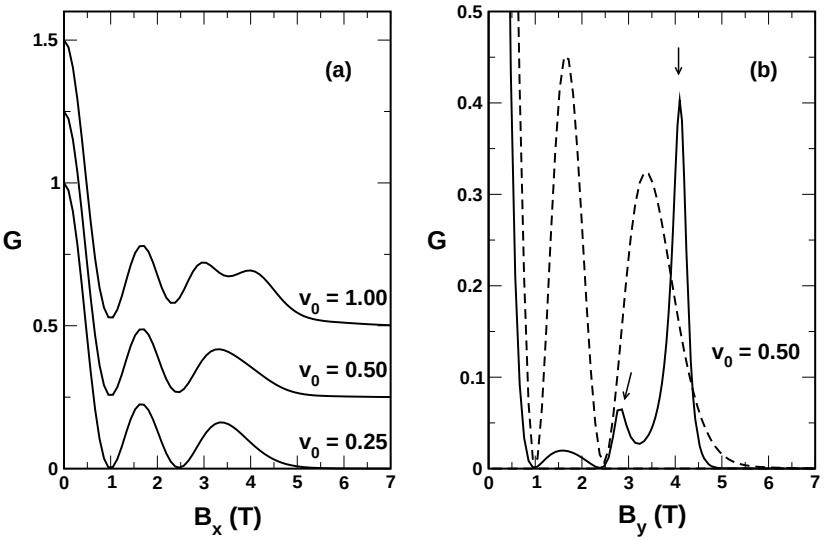

FIG. 1: The dependences of the tunneling conductance (in arbitrary units) as functions of the in-plane magnetic field strength. Panels (a) and (b) correspond to the magnetic field applied in the x and y direction, respectively. For the sake of clarity, the three curves pertaining to different potential modulation strengths in panel (a) are displaced relative to each other by 0.25 units. The full line in panel (b) shows the tunneling conductance with the peaks originating from the bandstructure effects indicated by arrows. Their observation is hampered by the presence of the oscillating prefactor (30) whose behaviour is depicted by the dashed line.

plots. The three curves are offset by 0.25 units for clarity and correspond to three different strengths of the externally applied potential modulation which is assumed to be of a simple cosine shape. We model the potential by setting the two principal Fourier components to equal strength

$$v(\pm 1, 0) = v_0 = 0.25,\ 0.50, \text{ and } 1.00,$$

respectively, measured in the cyclotron energies. The electronic screening, taken into account at the mean field level, reduces the amplitude of the potential modulation approximately three times and also leads to the appearance of a few higher non-vanishing Fourier components.

The lowermost curve in Fig. 1 (a) corresponds to a rather weak potential which does not effectively mix different Landau levels. Thus, since the chemical

potential is located in the second Landau band, the most of the structure in the G versus $B_x^{\parallel} \sim \Delta k_x$ dependence comes from the oscillating prefactor [see Eqs. (14) and (26)]

$$B_{22}(\Delta k_x) = \mathrm{e}^{-\Delta k_x^2/4} L_2\left(\frac{\Delta k_x^2}{2}\right). \tag{30}$$

Similar oscillations were previously predicted in the tunneling conductance of uniform 2D electron gases.[15] As the potential modulation increases so does the coupling between different Landau levels. In Fig. 1 (a), we see that for higher values of v_0, the shape of the curve develops an additional oscillation thus indicating an appreciably strong admixture of the third Landau level to the states in the second Landau band.

In panel (b), we display the dependence of the tunneling conductance on the in-plane magnetic field applied in the y direction for the case when the potential modulation strength is set to $v_0 = 0.5$. Since the filling factor equals $\nu_L = 2.4$, the Fermi area in the second band is a stripe along q_1 covering 40% of MBZ. Therefore, when the in-plane magnetic field displaces the two MBZ's by 0.4 or 0.6 of their extension along q_2 relative to each other we expect to observe bandstructure-induced peaks in G. The full curve gives the calculated conductance as a function of $B_y^{\parallel}$ with the two expected peaks denoted by arrows, while the dashed line refers to the quantum oscillations (30) inevitably modulating the obtained results. We see that the direct observation of the bandstructure effects is made difficult by the presence of such oscillations since the typical scale of the rapid oscillations of the Laguerre polynomial in Eq. (30) coincides with the scale of momentum shifts of interest. For example, the second zero of the Laguerre polynomial occurs very close to the first interesting peak in Fig. 1 (b) thus strongly suppressing its height. On the other hand, the tunneling conductance shows a shallow maximum between 1 and 2 Tesla resulting from the modulating prefactor (30) and not from the bandstructure effects. Therefore, one concludes that the direct use of these conductance peaks as a probe of the Fermi area is, in the general case, rather unjustified.

However, the situation can be salvaged by measuring the tunneling conductance not as a function of the parallel magnetic field strength but of its *direction*. Most of the oscillatory contributions to the tunneling current unrelated to the underlying bandstructure (26) depend on the absolute value of $\mathbf{B}^{\parallel}$, or $\Delta\mathbf{k}$, but not on its direction. Therefore, their presence will only set the absolute scale of the resulting tunneling currents but will not contribute any oscillations, and thus one will be able to interpret all the peaks as originating from the coincidence of certain boundaries of the Fermi areas.

In Figure 2, we schematically show the different transitions leading to the

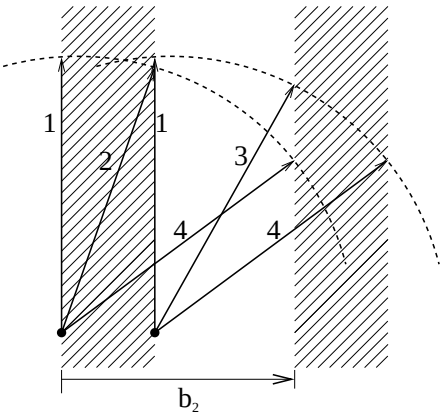

FIG. 2: Schematic diagram of electronic transitions leading to the appearance of peaks in the conductance vs. the magnetic field direction dependences. The hatched area corresponds to the occupied electronic states; the initial and final states of a tunneling transition must be situated on its boundaries. The peaks will appear whenever the crystal momentum of the tunneling electrons is shifted by an amount needed to reach a boundary of the Fermi area or its repetition in a neighbouring MBZ.

peaks in the tunneling conductance. The hatched area corresponds to the Fermi area, that is, the occupied electron states. As discussed above, the Fermi area is a stripe extending uniformly in the $\mathbf{b}_1$ direction and repeating itself periodically in the perpendicular $\mathbf{b}_2$ direction. The two dots in Fig. 2 denote two 'initial' electronic states located on the two opposite boundaries of the Fermi area. The possible 'final' states for a tunneling transition are located on the two circles of radius equal to the crystal momentum shift due to the in-plane magnetic field and centered on the 'initial' states. Here we choose the momentum shift to exceed slightly the length of the reciprocal lattice vector $\mathbf{b}_2$. Starting with the magnetic field directed along the stripes, we will observe a peak "1" corresponding to electrons jumping along the stripe borders. Later, rotating the direction of the magnetic field clockwise we will encounter peak "2" attributed to the electrons jumping across the stripe, and peak "3" due to those jumping across the white area separating the stripes. If more than one half of the band is filled the peaks "2" and "3" will show up in the opposite order. Finally, there comes peak "4" associated with the electron transitions into a neighbouring MBZ.

In Figure 3, we show the calculated dependences of the tunneling conductance G as a function of the y component of the *rotated* in-plane magnetic field. The strength of the field is kept fixed at $B = 7.62\,\mathrm{T}$ and only its direction is varied. The peaks appearing in the plot correspond to those labelled by "1", "2", "3" and "4" in the foregoing discussion. The four curves are obtained for four different strengths of the modulation, and are offset by 5 units for clarity. Comparing these curves we observe that the increasing strength of the external potential leads to a redistribution of the peak strengths. Thus the height of the second peak, close to $B_y = 3$ T, decreases with the increasing modulation

strength and for $v_0 = 1.00$ almost vanishes altogether. The reason for such behaviour can be traced to the expression of the overlap integral $B_{nn'}$ (14) connecting different Landau levels, $n \neq n'$. In this case, the expression of $B_{nn'}$ contains a factor

$$\begin{aligned} (\Delta k_y + i\Delta k_x)^{n-n'} \quad & \text{if } n > n' \\ (-\Delta k_y + i\Delta k_x)^{n'-n} \quad & \text{if } n < n' \end{aligned} \tag{31}$$

leading to an anisotropic contribution to the tunneling current whose impact is increasing proportionally to the degree of mixing of the different Landau levels. While this rather structureless dependence (31) of the tunneling matrix element on the direction of the magnetic field can not lead to the appearance of any extra peaks it can, nevertheless, hamper the observation of some of the present ones.

Figure 4 presents an investigation of the broadening effects. All the previous dependences were obtained assuming a phenomenological width of the Lorentzian spectral function set to a few percent of the total miniband width, that is to around ten percent of its filled part. In Fig. 4 we show how the curve corresponding to $v_0 = 0.5$ is affected by increasing Δ two and four times. The disorder present in any real system would make the observability of the bands in the tunneling experiment more difficult.

Finally, in Figure 5 we present the typical dependence of the tunneling conductance on the y component of the in-plane magnetic field of constant magnitude involving a double-layer setup with *non-identical* layers. As before, we apply an external potential modulated along the x direction of equal strength $v_0 = 0.5$ to both layers, however, we also apply a uniform bias so that the electron density in one of the layers is reduced and the filling factor is lowered to $\nu'_L = 2.2$. Thus, the electrons fill only 20% of the third Landau band in this layer. We note in Fig. 5 that the central peak at $B_y = 0$ T disappears since the two MBZ are no longer aligned. The two left peaks in the Figure 5 correspond to the relative displacement of the two Fermi areas by 0.1 and 0.3 of the extension of MBZ in the dispersion direction, that is by the difference and the sum of the half-widths of the two Fermi stripes. The two right peaks occur at the displacements equal to 0.7 and 0.9 of the MBZ extension, i. e. when a displaced Fermi stripe of one layer meets the repetition of the Fermi stripe of the other layer in a neighbouring MBZ.

This example demonstrates the practical scheme of how one can measure the bandstructures in unidirectionally modulated 2DES. The relative shift of the peaks as a function of the constant bias voltage between the two layers provides the complete information about the band dispersions, that is the energy dependence on q_2.

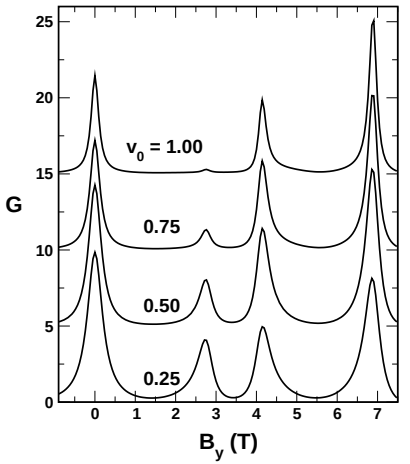

FIG. 3: Tunneling conductance (in arbitrary units) as a function of the y component of the rotated in-plane magnetic field. The four curves corresponding to the different values of the potential modulation strength are offset by 5 units relative to each other. The four peaks occur at the $B_y^{\parallel}$ values corresponding to the shift of the q_2 component of the crystal momentum by 0, 0.4, 0.6 and 1.0 of the extension of MBZ. The height of the second peak reduces with increasing modulation potential v_0.

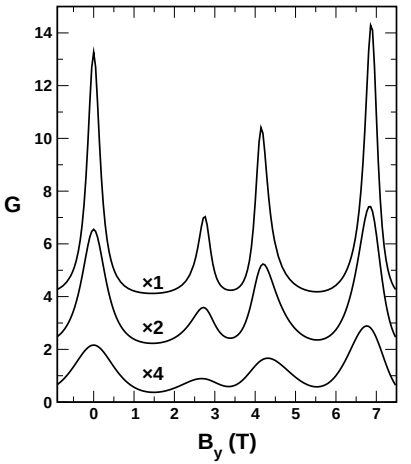

FIG. 4: The influence of the spectral function broadening on the tunneling conductance. The three dependences are offset by 2 units relative to each other. The topmost curve corresponds to the broadening $\Delta = 0.004$, used in obtaining the results presented in the previous Fig. 3, while the other two are obtained by increasing the broadening two and four times, respectively.

VI. BIDIRECTIONAL MODULATION

When the periodic potential modulation is applied in both lateral directions the resulting energy bands become dispersive in both directions in MBZ. Consequently, the possible geometries of the Fermi areas are no longer restricted to parallel stripes, and can assume arbitrarily complicated shapes. These facts make the corresponding analysis of a tunneling conductance measurement aimed at the determination of the underlying artificial bandstructure much more complicated, but on the other hand, also more interesting. As before, scanning the two dimensional phase space of crystal momentum shifts $\{\Delta k_x, \Delta k_y\}$ along

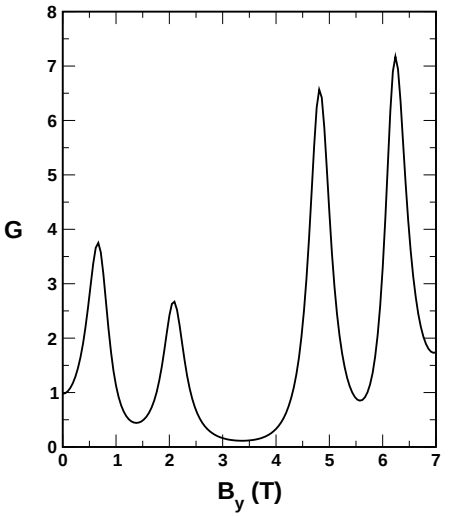

FIG. 5: The tunneling conductance between two non-identical two-dimensional electron layers. The peak positions correspond to the crystal momentum shifts equal to the difference or the sum of the half-widths of the two involved Fermi stripes.

circular paths one would be able to identify peaks corresponding to the displacements of the Fermi areas relative to each other that make their boundaries intersect, thus allowing for a certain tunneling rate. Even larger tunneling rate would result from the displacements that make certain fragments of the Fermi area boundaries to be aligned nearly parallel to each other. However, the heights of the resulting peaks in the tunneling conductance are strongly modulated by the oscillatory factors that enter the expression of the tunneling matrix element (26) and do not directly reflect the tunneling rate, thus obscuring the bandstructure effects.

Further complications arise from the fact that in a commensurate magnetic field the Landau bands will be split into a set of closely spaced subbands. Then, the Fermi area may develop a complicated multilayered shape provided that more than one of these subbands is partially filled.

Instead of pursuing these complications and trying to develop an analysis of the tunneling data for some special cases, we concentrate on the possibility to perform a simpler, and less informative measurement, of the density of states (DOS). Such a measurement can be realized if the miniband widths in one of the layers are much smaller than in their counterparts in the other layer and the width of the spectral function. Then, trapping the chemical potential inside the flat band one effectively transforms one of the layers into a controllable probe. In this case, the tunneling events are equally likely to originate from *any* point in MBZ of this layer and the net tunneling current is set by the available

phase space in the other one, given mainly by DOS at the chemical potential smeared by the width of the spectral function. Such a measurement would be performed at a fixed value of the in-plane magnetic field tuning the displacement of subband energies instead.

The key question to be answered is how one can realize such a double-layer system that the minibands are sufficiently broad in order to be observable in one of the layers while at the same time maintaining sufficiently small widths in the other one. Any periodic potential modulation created in one of the layers would inevitably affect the electron motion and broaden the energy bands in both layers. A possible way to achieve the desired situation is to use the so-called flat-band condition. As can be seen from Eq. (14) a cosine-like square-symmetric external potential, sufficiently weak so as not to couple the different Landau levels, will modulate the overall width of the Landau band evolving from the n-th Landau level according to the factor

$$B_{nn} = \exp\left(-\frac{\pi}{2L}\right) L_n\left(\frac{\pi}{L}\right). \tag{32}$$

Here we used Eq. (4) to express the length of the shortest reciprocal lattice vector of a square lattice. If the value π/L falls close to a zero of the Laguerre polynomial of a certain index n, the resulting width of the n-th band will be small.

A fortunate situation arises when $L = 3$. Then the value of $\pi/3$ is indeed very close to the zero of the first Laguerre polynomial which occurs at the value of its argument equal to 1. At the same time, the second Landau band will be sufficiently broad since it stays fairly far away from the flat-band conditions given by the zeros of the second Laguerre polynomial $2 \pm \sqrt{2}$.

We consider a square lattice of a lattice constant $a_1 = a_2 = 1200\,\text{Å}$. Then a perpendicular magnetic field of the same strength as before $B = 0.86$ T will create a commensurate flux of $L = 3$ flux quanta per unit cell, and the electron concentration $n_s = 0.833{\cdot}10^{11}$ cm^{-2} or $n_s = 1.25{\cdot}10^{11}$ cm^{-2} will fill two or three Landau levels, respectively, thus making the tuning of the filling factor around the interesting values feasible. We model the external potential by setting the four lowest Fourier components to equal strength

$$v(\pm 1, 0) = v(0, \pm 1) = v_0,$$

and perform calculations for two values of $v_0 = 0.33$ and 0.83. The electronic screening in this regime is capable of reducing the potential modulation amplitude approximately 4.5 times.

Figure 6 shows the typical dependences of the tunneling conductances obtained when the chemical potential is trapped in the middle of the first Landau

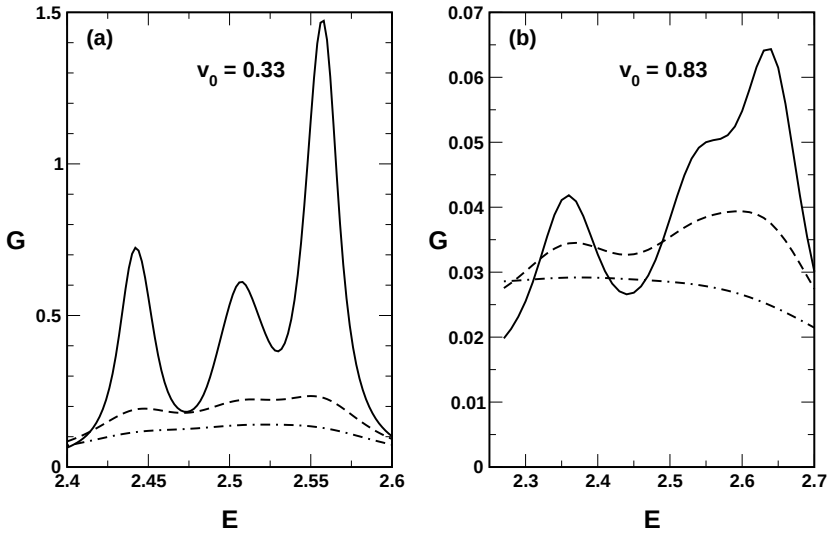

FIG. 6: The spectroscopic density of states of a modulated 2DES in the second Landau band centered at $E_0 = 2.5$. Panel (a) shows the results obtained using a fairly weak potential modulation $v_0 = 0.33$, while in panel (b) the modulation strength is increased to $v_0 = 0.83$. The full, dashed, and dot-dashed lines belong to three different values of spectral function width Δ.

band at $\mu = 1.5$ in one of the layers, and scans the second Landau band (situated around $E_0 = 2.5$) in the other layer. Panel (a) corresponds to a relatively weak modulation; in this case we are able to resolve the splitting of DOS into $L = 3$ peaks. The full curve is obtained by setting the spectral function broadening to $\Delta = 0.02$ roughly corresponding to the width of the narrow first Landau band, thus smaller than the width of the broader second Landau band. The dashed and dot-dashed curved are obtained by increasing Δ to 0.033 and 0.05, respectively. In these cases the DOS oscillations indicating the subband structure can not be resolved any more. Panel (b) corresponds to a much stronger external potential. The full line is obtained by setting the broadening to $\Delta = 0.05$ in order to ensure a fairly uniform tunneling from the entire area of the MBZ in the first Landau band; the dashed and dot-dashed lines correspond to $\Delta = 0.10$ and 0.20, respectively. In this case, we are not able to clearly resolve the expected three peaks in the DOS of the second Landau band. The reason is that the modulating potential is sufficiently strong to be able to couple different Lan-

dau levels, thus rendering the realization of the flat-band condition inefficient leading to inability to maintain the widths of the probing first Landau band sufficiently narrower than the probed second.

VII. SUMMARY

In summary, we developed a description of tunneling between two parallel electronic layers in tilted magnetic fields basing on the formalism of magneto-translational symmetry group. The tunneling transitions of electrons are interpreted as occurring between points in the magnetic Brillouin zone displaced with respect to each other by a magnetic crystal momentum shift induced by an in-plane magnetic field. This leads us to a possibility to investigate the artificially created magnetic bandstructure in the layers similarly to the optical experiments in conventional 3D solids.

ACKNOWLEDGMENTS

The author is grateful to Drs. Peter Johansson and Carlo M. Canali for valuable comments on the manucript and their general interest in this work.

REFERENCES

* Electronic address: egidijus@teorfys.lu.se

[1] T. Ando, A. B. Fowler, and F. Stern, Rev. Mod. Phys. **54**, 437 (1982); *Physics of Low-Dimensional Semiconductor Structures*, edited by P. Butcher, N. H. March, and M. P. Tosi (Plenum, New-York, 1993).

[2] C. W. J. Beenakker and H. van Houten, in *Solid State Physics*, edited by H. Ehrenreich and D. Turnbull (Academic Press, Boston, 1991), Vol. 44, p. 1.

[3] B. J. van Wees, H. van Houten, C. W. J. Beenakker, J. G. Williamson, L. P. Kouwenhoven, D. van der Marel, and C. T. Foxon, Phys. Rev. Lett. **60**, 848 (1988); D. A. Wharam, T. J. Thornton, R. Newbury, M. Pepper, H. Ahmed, J. E. F. Frost, D. G. Hasko, D. C. Peacock, D. A. Ritchie, and G. A. C. Jones, J. Phys. C **21**, L209 (1988).

[4] K. v. Klitzing, G. Dorda, and M. Pepper, Phys. Rev. Lett. **45**, 494 (1980); *The Quantum Hall Effect*, edited by R. Prange and S. M. Girvin (Springer-Verlag, New York, 1987).

[5] M. Ya. Azbel', Zh. Eksp. Teor. Fiz. **46**, 929 (1964) [Sov. Phys. JETP **19**, 634 (1964)].
[6] D. R. Hofstadter, Phys. Rev. B **14**, 2239 (1976).
[7] T. Schlösser, K. Ensslin, J. P. Kotthaus, and M. Holland, Semicond. Sci. Technol. **11**, 1582 (1996).
[8] C. Albrecht, J. H. Smet, K. von Klitzing, D. Weiss, V. Umansky, and H. Schweizer, Phys. Rev. Lett. **86**, 147 (2001).
[9] D. Weiss, K. v. Klitzing, K. Ploog, and G. Weimann, Europhys. Lett. **8**, 179 (1989); R. R. Gerhardts, D. Weiss, and K. v. Klitzing, Phys. Rev. Lett. **62**, 1173 (1989); R. W. Winkler, J. P. Kotthaus, and K. Ploog, *ibid.* **62**, 1177 (1989).
[10] K. Kern, D. Heitmann, P. Grambow, Y. H. Zhang, and K. Ploog, Phys. Rev. Lett. **66**, 1618 (1991); K. Bollweg, T. Kurth, D. Heitmann, E. Vasiliadou, K. Eberl, and H. Brugger, Phys. Rev. B **52**, 8379 (1995); M. Hochgräfe, R. Krane, Ch. Heyn, and D. Heitman, Phys. Rev. B **60**, 10 680 (1999).
[11] J. P. Eisenstein, T. J. Gramila, L. N. Pfeiffer, and K. W. West, Phys. Rev. B **44**, 6511 (1991).
[12] S. Q. Murphy, J. P. Eisenstein, L. N. Pfeiffer, and K. W. West, Phys. Rev. B **52**, 14 825 (1995).
[13] N. Turner, J. T. Nicholls, E. H. Linfield, K. M. Brown, G. A. C. Jones, and D. A. Ritchie, Phys. Rev. B **54**, 10 614 (1996).
[14] L. Zheng and A. H. MacDonald, Phys. Rev. B **47**, 10 619 (1993).
[15] S. K. Lyo, Phys. Rev. B **57**, 9114 (1998).
[16] M. H. Cohen, L. M. Falicov, and J. C. Phillips, Phys. Rev. Lett. **8**, 316 (1962).
[17] R. E. Prange, Phys. Rev. **131**, 1083 (1963).
[18] J. Bardeen, Phys. Rev. Lett. **6**, 57 (1961).
[19] B. D. Josephson, *in D. Parks, Superconductivity*, 423 (1969); G. D. Mahan, *Many Particle Physics* 2nd ed. (Plenum, New York, 1990), Chap. 9.
[20] E. Anisimovas and P. Johansson, Phys. Rev. B **60**, 7744 (1999).
[21] E. Anisimovas and P. Johansson, J. Phys.: Condens. Matter **13**, 3365 (2001).
[22] H.-J. Schellnhuber, Phys. Rev. B **25**, 2358 (1982).
[23] J. Zak, Phys. Rev. Lett. **19**, 1385 (1967).

Hydrodynamics of antidot superlattices

Egidijus Anisimovas*
Division of Solid State Theory, University of Lund, Sölvegatan 14A, S-223 62 Lund, Sweden

We present a calculation of collective modes and absorption spectra in lateral antidot superlattices based on a semiclassical "hydrodynamic" approach. An explicit Thomas-Fermi-von Weizsäcker kinetic energy functional is introduced and used to derive the equations describing the static and dynamical properties of antidot superlattices in terms of its charge density. We discuss the formation of the collective excitation spectrum, the magnetic-field dispersions and the nature of the collective modes.

PACS numbers: 73.21.Cd, 78.67.Hc

I. INTRODUCTION

During the last decade the study of laterally structured systems of two-dimensional electrons has attracted much physicists' attention. Besides confined geometrical setups, such as quantum dots[1] or dot arrays,[1,2] systems in which a periodic potential modulation allows an extended electronic motion have been studied. Such artificial setups can be prepared using a variety of techniques, such as carrier density modulation by the persistent photoconductivity effect,[3] application of a voltage bias on patterned gates, inducing an internal lattice strain or by etching holes[4,5] through the layer of two-dimensional electrons, thereby creating an ordered array of antidots.

Since these systems typically feature large lattice constants $a \approx 300 - 800\,\mathrm{nm}$, to be compared to the typical Fermi wavelength of order of 30 nm in GaAs, the motion of electrons lies closer to the semiclassical regime. Thus, the magnetoresistance measurements[4] in antidot superlattices revealed low-magnetic-field anomalies which were successfully explained in terms of classical electron pinball trajectories.[6]

The optical experiments conducted on antidot superlattices have succeeded in measuring the far infra-red transmission spectra and identifying a number of characteristic absorption minima[5] which indicate the presence of underlying collective modes of the corresponding frequencies. The frequency dispersions versus the magnetic field strength have been measured[5,7] and, besides

the cyclotron resonance, revealed two other distinct branches showing a characteristic anticrossing behaviour. At low frequencies, one observes the edge magnetoplasmon[8] excitation whose frequency decays as $1/B$ in strong magnetic fields. The other – high frequency – mode starts from some finite frequency value at the zero magnetic field and approaches the cyclotron-resonance line asymptotically from above in the high-field limit. Both modes are polarized in the cyclotron direction.[7] More recent investigations succeeded in discovering collective modes polarized in the anti-cyclotron direction as well as additional high-energy modes.[9] Experiments involving a double-layer setup with holes etched through both layers reported a rearrangement of the modes of the individual layers into coupled acoustic and optical branches.[10]

A number of theoretical approaches treating the collective excitations in antidots from the classical point of view and dealing with the periodicity of the system in one or another approximate way have been put forward. They include a variational calculation based on the Wigner-Seitz approach[11] which replaced the square unit lattice cell with a circular one. The geometry effects and the electron-electron interaction were treated in an approximate fashion still successfully predicting a few of the major trends in the dispersions of the lowest-energy modes. A theory based on the classical electrodynamics has also been proposed.[12,13] In this approach, the electron density in an antidot superlattice was not calculated but assumed to be of a simple step-like shape, and the superlattice potential was interpreted as a grating coupler. The various collective modes of antidot superlattices were thus mapped onto those of the bulk magnetoplasmon folded into a single unit cell of the reciprocal lattice. The frequencies of the collective excitations in antidots were found to be close to the bulk magnetoplasmon frequencies corresponding to the reciprocal lattice vectors. A quantum-mechanical calculation[14] based on the random-phase approximation has also been reported. This work has addressed superlattices of a rather short period and besides the collective modes revealed a rich spectrum of single-particle excitations.

In the present paper, we discuss the spectrum of the collective excitations in large-period antidot superlattices from the point of view of a semiclassical approximation based on an explicit representation of the total-energy functional. The origins of the employed method lie in the early work of Thomas,[15] Fermi[16] and von Weizsäcker,[17] and its extension to the dynamical regime by Bloch.[18] Some of the recent applications include calculations of magnetoplasmons in quantum wells,[19] quantum rings[20] and wires.[21] While this approach is usually introduced with no intent to maintain theoretical rigour, especially in describing the time-dependent phenomena, a sufficient work has been done to insure its justification. The kinetic energy correction proposed by von Weizsäcker[17] has

later been related to the construction of the gradient expansions for the kinetic energy functional.[22,23] From the point of view of the time-dependent density functional theory,[24] the dynamical regime of the present approach can be viewed as the construction of an explicit functional[25] governing the time evolution of the current density,[24] and has recently been successfully applied to describe the optical response of small metallic clusters.[26]

The present paper is organized in the following way. In Section II, we outline the theoretical formalism, and devote the following Section III to the main results and conclusions. The paper ends with a summarizing Section IV.

II. THEORY

We describe the two-dimensional electron fluid moving in an external potential $w(\mathbf{r})$ by introducing its total energy functional

$$E_w[n] = T_s[n] + \int d^2r\, w(\mathbf{r})n(\mathbf{r}) + \frac{1}{2}\int d^2r \int d^2r'\, \frac{n(\mathbf{r})n(\mathbf{r}')}{|\mathbf{r}-\mathbf{r}'|} + E_{\rm xc}[n]. \quad (1)$$

The two middle terms on the right-hand side of Eq. (1) represent the classical contributions of the potential energy of the electrons in the external field and their mutual Coulomb repulsion. The other two terms are the kinetic energy of *noninteracting* electrons $T_s[n]$ and the exchange-correlation energy $E_{\rm xc}[n]$, respectively. These terms are of a quantum mechanical origin, and are given by universal (and not known explicitly) functionals of the electron density $n(\mathbf{r})$ alone. Note, that we use the "effective atomic" units defined by setting

$$\hbar = m^* = \frac{e^2}{\kappa} = 1. \quad (2)$$

Here m^* is the effective electron mass in the medium and κ is the static dielectric constant. Using the values of GaAs, $m^* = 0.067\, m_e$ and $\kappa = 12.4$, we find that the corresponding length unit (the effective Bohr radius) equals $a_0 \approx 10\,\text{nm}$ and the energy unit (the effective Rydberg) is approximately 6 meV.

The chief virtue of the density functional theory[23,27] related methods is the ability to treat the largest contributions to the total energy exactly, while the less important terms are approximated in a reasonably accurate and simple way. In most applications, however, the kinetic energy term is among the largest and the necessity of its accurate treatment leads to the solution of microscopic Kohn-Sham equations.[28] The artificially structured low-dimensional systems, such as large-period lateral superlattices, often operate in a regime where the contribution of the kinetic energy is less significant and one can think of its reasonable

approximation by an *explicit* functional, thus formulating equations directly in terms of the electronic density. Following other authors,[19–21] we choose to work within the two-dimensional version of the local (Thomas-Fermi[15,16]) approximation supplemented by the leading gradient-expansion (von Weizsäcker[17]) term

$$T_s[n] = T_{\rm TF}[n] + \lambda T_{\rm W}[n] = \frac{\pi}{2}\int d^2r\, n^2(\mathbf{r}) + \frac{\lambda}{8}\int d^2r\, \frac{|\nabla n(\mathbf{r})|^2}{n(\mathbf{r})}, \qquad (3)$$

with the value of λ set to 0.25. The exchange-correlation energy is approximated by a local exchange-only term

$$E_{\rm x} = -\frac{4}{3}\sqrt{\frac{2}{\pi}}\int d^2r\, [n(\mathbf{r})]^{3/2}. \qquad (4)$$

According to the variational Hohenberg-Kohn principle[27] the total energy is stationary with respect to density fluctuations around the exact ground-state density n_0. This leads to the Euler equation

$$\left.\frac{\delta E_w[n]}{\delta n(\mathbf{r})}\right|_{n_0} = \mu \qquad (5)$$

which has to be solved for the ground-state density. Evaluating the functional derivatives of (1), (3) and (4) and expressing them in terms of the square root of the density $\psi(\mathbf{r}) = \sqrt{n(\mathbf{r})}$ we arrive at the following equation for the function $\psi(\mathbf{r})$

$$\left[-\frac{\lambda}{2}\nabla^2 + u(\mathbf{r}) - \mu\right]\psi(\mathbf{r}) = 0. \qquad (6)$$

This equation resembles the Schrödinger equation for a particle of mass λ^{-1} moving in an effective potential

$$u(\mathbf{r}) = w(\mathbf{r}) + \int d^2r'\, \frac{\psi^2(\mathbf{r}')}{|\mathbf{r}-\mathbf{r}'|} + \pi\psi^2(\mathbf{r}) - \sqrt{\frac{8}{\pi}}\psi(\mathbf{r}) \qquad (7)$$

which consists of the usual terms representing the external and Hartree potentials supplemented by the extra Thomas-Fermi and exchange contributions. We note, that since the effective potential in Eq. (7) depends on $\psi(\mathbf{r})$, the equations (6) and (7) have to be solved self-consistently by convergent iterations. As a matter of fact, the equation (6) for the square root of the density is in principle exact,[29] however, the explicit expression of $u(\mathbf{r})$ is not known. Our formula (7)

is the approximation corresponding to, and resulting from, the approximations made for the kinetic and exchange-correlation energies in Eqs. (3) and (4).

The internal restoring force arising in an electron fluid when its density deviates from the exact ground-state density can be obtained by evaluating a functional derivative similar to (5)

$$\left.\frac{\delta E_w[n]}{\delta n(\mathbf{r})}\right|_{n_0+n_1} \tag{8}$$

at the modified density value, which we choose to represent as $n_0 + n_1$, with n_0 being the correct ground state density for the external potential $w(\mathbf{r})$ and n_1 expressing the small deviation. Indeed, assuming that the disturbed density n_0+n_1 is v-representable, and thus is a ground state for some modified potential $w+w_1$, and taking into account the fact that the total-energy functional depends on the external potential only through the potential energy term, we have

$$\left.\frac{\delta E_w[n]}{\delta n(\mathbf{r})}\right|_{n_0+n_1} = \left[\frac{\delta}{\delta n}\left(E_{w+w_1}[n] - \int d^2r\, w_1(\mathbf{r})n(\mathbf{r})\right)\right]_{n_0+n_1} = \mu - w_1(\mathbf{r}) \tag{9}$$

Since w_1 is the additional external potential needed to keep the density $n_0 + n_1$ in the equilibrium, its gradient equals the internal restoring force, thus

$$\mathbf{F}_{\rm int} = \nabla w_1(\mathbf{r}) = -\nabla\left\{\frac{\delta}{\delta n(\mathbf{r})}E_w[n(\mathbf{r})]\right\}_{n_0+n_1} = -\nabla\Phi(\mathbf{r}). \tag{10}$$

Here we expressed the internal force $\mathbf{F}_{\rm int}$ via its scalar potential Φ. Writing the density fluctuation as $n_1 = 2\psi_0\psi_1$ and carrying out the functional derivation we obtain

$$\begin{aligned}\Phi(\mathbf{r}) &= 2\pi\psi_0\psi_1 - \frac{\lambda}{2}\psi_0^{-2}[\psi_0\nabla^2\psi_1 - \psi_1\nabla^2\psi_0] \\ &+ 2\int d^2r'\,\frac{\psi_0(\mathbf{r}')\psi_1(\mathbf{r}')}{|\mathbf{r}-\mathbf{r}'|} - \sqrt{\frac{8}{\pi}}\psi_1(\mathbf{r})\end{aligned} \tag{11}$$

to the linear order in ψ_1.

The result (11) is used to describe the dynamics of a two-dimensional electron fluid under the effect of external time-dependent forces $\mathbf{F}_{\rm ext}$. In addition to the density field, we introduce the velocity field $\mathbf{v}$ governed by the continuity equation and the equation of motion

$$\begin{aligned}\frac{\partial}{\partial t}n + \nabla\cdot(n\mathbf{v}) &= 0, \\ \left(\frac{\partial}{\partial t} + \mathbf{v}\cdot\nabla\right)\mathbf{v} &= \mathbf{F} - \mathbf{v}\times\vec{\omega}_c - \eta\mathbf{v}.\end{aligned} \tag{12}$$

Here $\mathbf{F}$ stands for the net force $\mathbf{F}(\mathbf{r}) = \mathbf{F}_{\rm ext}(\mathbf{r}) - \nabla\Phi(\mathbf{r})$, η is a phenomenological damping parameter, and the vector $\vec{\omega}_c$ is given by

$$\vec{\omega}_c = \frac{e\mathbf{B}}{mc}.$$

Its absolute value equals the cyclotron frequency, and its direction is perpendicular to the layer of the two-dimensional electrons, consequently also to the velocity field. Linearizing the hydrodynamic equations (12) around the equilibrium density and assuming the harmonic temporal dependence $\mathrm{e}^{-i\omega t}$ of the dynamic quantities we obtain

$$\begin{aligned} -i\omega\psi_1 \;&+\; \frac{1}{2}\psi_0\nabla\cdot\mathbf{v} + \mathbf{v}\cdot\nabla\psi_0 = 0, \\ -i\tilde{\omega}\mathbf{v} \;&=\; \mathbf{F} - \mathbf{v}\times\vec{\omega}_c. \end{aligned} \tag{13}$$

here $\tilde{\omega} = \omega + i\eta$. The second equation in (13) is readily solved with the result

$$(\tilde{\omega}^2 - \vec{\omega}_c^2)\mathbf{v} = \mathbf{F}\times\vec{\omega}_c + i\tilde{\omega}\mathbf{F}, \tag{14}$$

and when substituted into the first line of Eq. (13) yields

$$\begin{aligned} \omega(\tilde{\omega}^2 - \vec{\omega}_c^2)\,\psi_1 \;&+\; \frac{1}{2}\tilde{\omega}\psi_0\nabla^2\Phi - i\vec{\omega}_c\cdot(\nabla\psi_0\times\nabla\Phi) + \tilde{\omega}(\nabla\psi_0\cdot\nabla\Phi) \\ &=\; -i\vec{\omega}_c\cdot(\nabla\psi_0\times\mathbf{F}_{\rm ext}) + \tilde{\omega}\,(\nabla\psi_0\cdot\mathbf{F}_{\rm ext}). \end{aligned} \tag{15}$$

Note, that in Eq. (15) the scalar potential of internal forces Φ is a functional of ψ_0 and ψ_1 given by (11). While the final equation describing the electron-fluid dynamics (15) looks quite complicated algebraically it can be solved straightforwardly by expanding the unknown density fluctuation ψ_1 in any suitable set of basis functions. Working in the linear regime we will obtain a coupled set of equations for the expansion coefficients. Following the suggestion of Ref. 19 we used the complete set of solutions to (6) as the basis; an alternative choice is the plane-wave basis. We obtain the power absorption in the system by numerically calculating the Joule heat generated in a unit cell of the antidot lattice. The positions of peaks in the absorption power dependences on the frequency will indicate the presence of a collective excitation of the given frequency.

III. RESULTS

We consider a square antidot superlattice of a lattice constant $a = 300\,\mathrm{nm}$ in both lateral directions. The external potential is assumed to be of a simple

cosine-like shape and is described by setting the four lowest Fourier components to equal strength w_0, thus

$$w(\mathbf{r}) = 2w_0 \left[\cos\left(\frac{2\pi x}{a}\right) + \cos\left(\frac{2\pi y}{a}\right) \right].$$

The electron concentration is set to $n = 10^{11}\,\mathrm{cm}^{-2}$.

A. Evolution of plasmon modes

We begin by considering the evolution of the plasma modes of a nearly uniform two-dimensional electron system in a zero magnetic field into those of an antidot superlattice by gradually turning on the underlying superlattice potential. It is well known that in a uniform 2D electron gas one observes a gapless plasma mode[30] whose classical frequency depends on length of the the wave-vector q as

$$\omega_{\mathrm{2D}} = \sqrt{2\pi n q}, \tag{16}$$

in the atomic units. At higher q's this expression is modified by the contributions from the quantum-mechanical terms in Eq. (1). In the presence of a weak external potential, the plasmon dispersion curve (16) will be folded into the central Brillouin zone of the reciprocal lattice. Concentrating on the long-wavelength limit and considering only the modes that occur at $q = 0$, we should observe a set of plasma oscillations at the frequencies corresponding to reciprocal lattice vectors

$$\omega_{k,l}^2 = 2\pi n \frac{2\pi}{a} \sqrt{k^2 + l^2}, \quad k, l \in \mathcal{Z}. \tag{17}$$

The results of a numerical calculation are presented in Figure 1. Indeed, as the external potential strength increases we detect the power absorption peaks at the expected frequency values starting from $\omega_{1,0} = 0.366$. As a matter of fact, the stars of the reciprocal lattice vectors lying on one of the axes or on the diagonal, e. g. $(k, l) = (1, 0), (1, 1)$ or $(2, 0)$, contain four equivalent vectors, however, in a square lattice at zero magnetic field the degeneracy is not lifted. On the contrary, as can be seen in Fig. 1 (a) we find a splitting of the mode $(2, 1)$, whose star of equivalent vectors contains eight elements, into two peaks.

The oscillator strength of these modes, especially the higher-energy ones, in weak potentials is rather low. As one can see in Fig. 1 (b), the strength of the most conspicuous mode $(1, 0)$ just barely reaches $2\,\%$ as the potential modulation approaches $w_0 = 0.4$. Most of the oscillator strength is contained

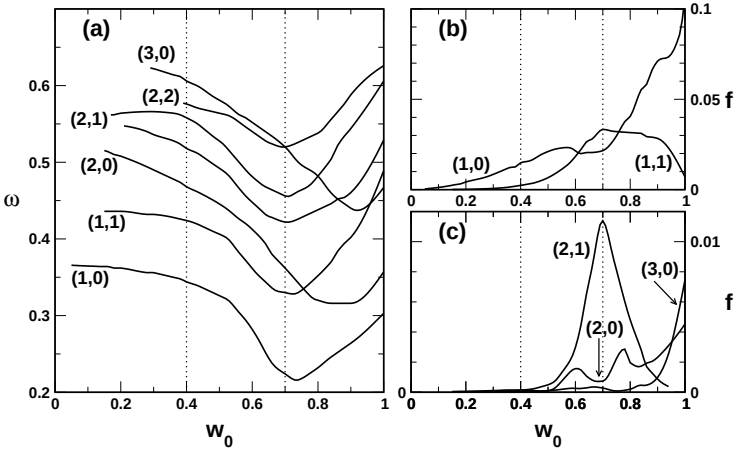

FIG. 1: The evolution of the plasmon modes into the collective modes of an antidot lattice. Panel (a) shows the frequencies of the seven lowest modes as a function of the external potential strength w_0; panels (b) and (c) display the dependences of the oscillator strengths. The unit of frequency equals $9.12 \cdot 10^{12}\,\mathrm{s}^{-1}$, and that of the potential strength is 6 meV. The oscillator strengths are given as the fraction of the total strength contained in *both* possible light polarizations. The vertical dotted lines delimit the three distinct regimes: the perturbative regime $w_0 \leq 0.4$, the formation of antidots in the range $0.4 \leq w_0 \leq 0.7$, and the expansion of the depleted areas for $w_0 \geq 0.7$.

in the zero-frequency mode. We hasten to add that total oscillator strength of all modes observed in each of the two possible light polarizations adds up to 50 %.

The regime defined by $w_0 \leq 0.4$ can be classified as perturbative. In this range of the potential modulations, the electron density is also modulated but stays finite at the locations of the potential maxima. The modes (k, l) are relatively dispersionless, and their frequencies stay close to the values given by (17). By directly inspecting the shape of the fluctuating charge densities associated with these modes we verified that the modes do not mix strongly between themselves. The Fourier analysis of the shape of charge density fluctuations of a given mode labelled by certain indices (k, l) shows that it is dominated by the corresponding mode of a uniform system of the same indices with only minor admixtures of the others.

The situation changes when we cross-over to the range of modulations

$0.4 \leq w_0 \leq 0.7$. In this regime the actual antidots are formed by depleting the electron density at their locations to nearly zero values. Therefore, the eigenfrequency spectrum and the nature of density oscillations is correspondingly modified. The frequencies of the system modes tend to shift towards the lower values. The oscillating charge densities tend to concentrate around the locations of the antidots rather than be spread nearly uniformly over the entire lattice cell. Naturally, the Fourier decomposition of the collective modes into the modes of a uniform system typically contains a number of constituents of appreciable strength. Therefore, while we still can trace the evolution of a certain density oscillation back to its predecessor of well-defined indices (k, l), the modes themselves are substantially modified.

In the range of modulation strengths $w_0 \geq 0.7$ we find a third distinct regime associated with the growth of the area where the electron density is depleted by the antidots. We note, that the dispersion curves reverse their behaviour and move towards the higher frequencies. It is interesting to observe, that the modes with one of the indices equal to zero tend to end up below the other ones. We find a number of crossings between the modes, and the oscillator strength dependencies show a rich set of features. The strengths of the modes $(1, 1)$ and $(2, 1)$ decline sharply having risen considerably at $w_0 \leq 0.7$. Instead, most of the oscillator strength is concentrating in the three lowest modes $(1, 0)$, $(2, 0)$ and $(3, 0)$. The curves corresponding to these modes shoot up rapidly in Fig. 1 (b) and (c).

In conclusion, we can judge that neither the mode frequencies nor the nature of density oscillations in a realistic antidot lattice are straightforwardly related to the spectrum of pure modes of a uniform system folded into a single Brillouin zone.

B. Spectra of antidot lattices

Having traced the evolution of the modes of antidot superlattices at zero magnetic field, we now proceed to the analysis of the magnetic-field dispersions. We set the external potential strength to $w_0 = 1.0$ (the highest value considered in the previous subsection) so that the diameter of the depleted charge density area approximately equals 40 % of the lattice constant.

The magnetic-field dispersions of the lowest-energy modes are shown in Figure 2. In panel (a) we show the spectrum obtained in the cyclotron polarization; the cyclotron resonance line ("CR") is clearly visible at all magnetic fields. The other modes either concentrate in the low-frequency part of the spectrum or start from a finite ω value at zero magnetic field and asymptotically approach

the "CR" line at high magnetic fields. We are able to resolve four distinct modes in the low-frequency regime, however, one of them (denoted "1^+") carries most of the oscillator strength. Likewise, mode "2^+" is the strongest mode in the upper part of the spectrum. We plot the oscillator strengths of these three modes in the panel (a) of Figure 3. It is clearly seen that, as the magnetic field strength increases, there is an oscillator strength transfer from the mode "1^+" to the mode "2^+" indicating a strong coupling between these modes.[5] On the other hand, the oscillator strength contained in "CR" is nearly independent of the magnetic field strength. The three modes discussed above nearly exhaust the oscillator strength sum rule at magnetic fields $B \geq 0.1$. The next few excitations lying just above the "2^+" line also carry an appreciable part (up to 0.7 – 2.0 % each) of the total absorption power and can be observed.[9] Most of the other collective oscillations of this polarization are almost inactive.

Panel (b) of Fig. 2 shows the modes active in the anti-cyclotron polarization. The general structure of the spectrum resembles that of the cyclotron polarization. Naturally, the cyclotron resonance line is missing. The two modes in the lower part of the high-frequency set show an interesting anticrossing behaviour. The lower of these modes (see the right panel of Fig. 3) is active in a very narrow range of magnetic fields close to zero and has been detected experimentally.[9] In the low-frequency regime we also find an active mode carrying a few percent of the net oscillator strength.

In order to achieve a better understanding of the collective excitations in antidot superlattices we also look at the fluctuating charge density distributions corresponding to the three strongest modes of the cyclotron polarization. Panels (a), (b) and (c) of Fig. 4 show the contour plots of the modes "1^+", "CR" and "2^+", respectively, within a single unit cell. The antidots are situated at the corners of the displayed area.

One can see that in all cases most of the oscillating density is concentrated in the area surrounding the antidots and the oscillations have a clear (coupled) dipole structure. It is interesting to compare these charge density plots to their analogues obtained in a previous attempt to investigate the structure of excitations closer to the quantum-mechanical regime.[14] We conclude that all the plots obtained in the present semiclassical simulation show a more clean cut and well-defined pattern of motion of the charge density maxima and minima relative to each other. On the contrary, the plots resulting from a microscopic random-phase calculation involve a considerable contribution of single-particle excitations and are typically more difficult to analyze. In that case the appearance of a clearer density pattern can be used to tell a collective mode from the electron-hole background.[14]

While the fluctuating density profiles depicted in the three panels of Fig. 4

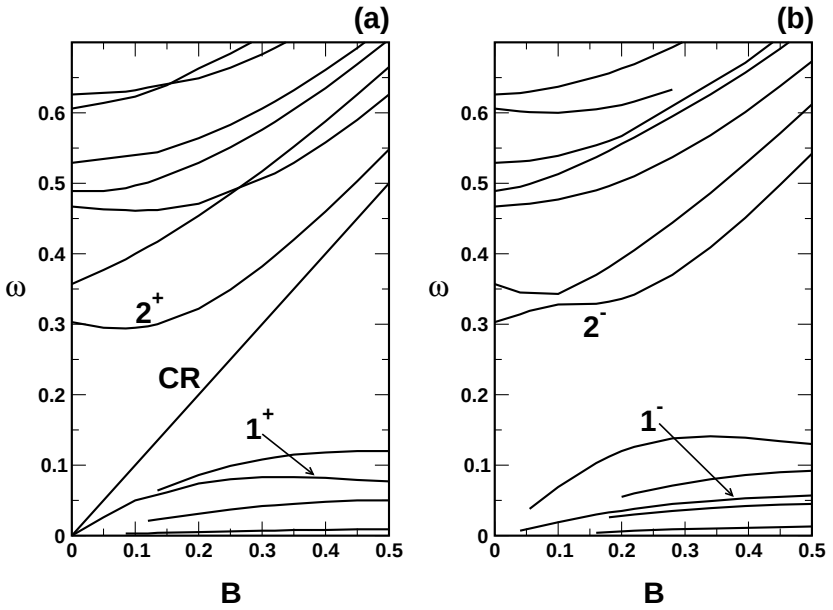

FIG. 2: The magnetic-field dispersions of the lowest-energy modes of the cyclotron [(panel (a)] and anti-cyclotron [(b)] polarization. Frequencies are measured in the units $9.12 \cdot 10^{12}\,\mathrm{s}^{-1}$, while the magnetic field strength unit equals 3.47 T. The label "CR" denotes the cyclotron resonance, "1" and "2" label the strongest modes whose oscillator strengths are depicted in a separate figure. The superscripts "+" and "−" refer, respectively, to the cyclotron and anti-cyclotron polarizations.

possess a large degree of similarity, there are notable differences. We see that the modes "1^+" and "2^+" involve an intricate pattern of coupled dipoles. The strongest one is situated around the antidots while the area between the antidots is occupied by a number of smaller charge density maxima and minima. In the case of "CR" the inter-antidot oscillations are few and not strongly pronounced. On the other hand, we note that in the low-frequency mode the maximum and the minimum of the dipole oscillating around an antidot are split by the strong interaction with the other oscillations into three near extrema.

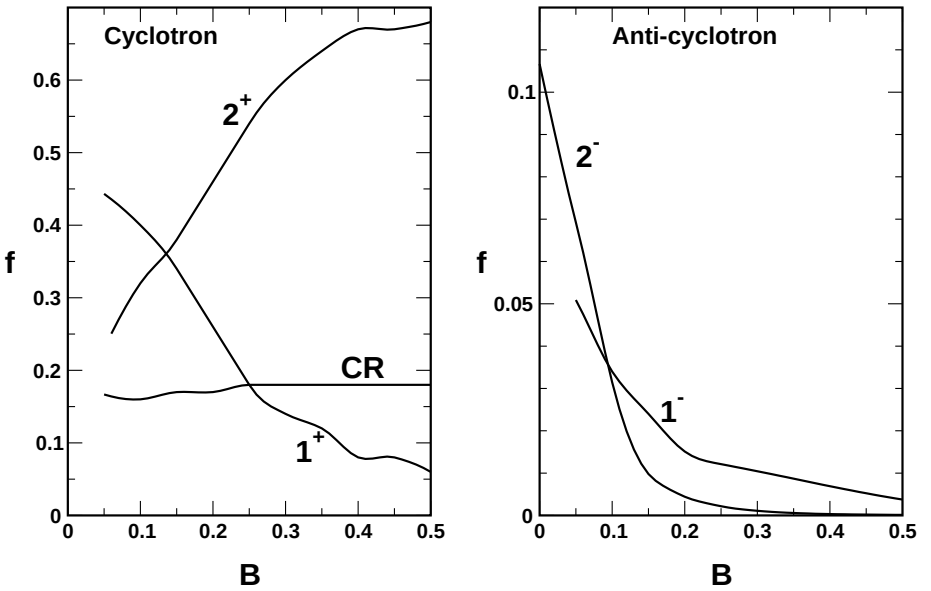

FIG. 3: The oscillator strengths of the most conspicuous modes presented in Figure 2 plotted versus the magnetic field strength.

IV. SUMMARY

In summary, we considered the dynamical properties of antidot superlattices using a semiclassical formulation of a method derived from the density functional theory. We analyzed the formation of the collective excitation spectra of the antidot lattices and their dispersions versus the magnetic field strength. The spectra display the presence of a large number of collective excitations in the system, however, only a few of them have an appreciable oscillator strength and can be detected experimentally.

ACKNOWLEDGMENTS

The author would like to thank Dr. Peter Johansson and Prof. Tsin-Fu Jiang for their interest and valuable discussions.

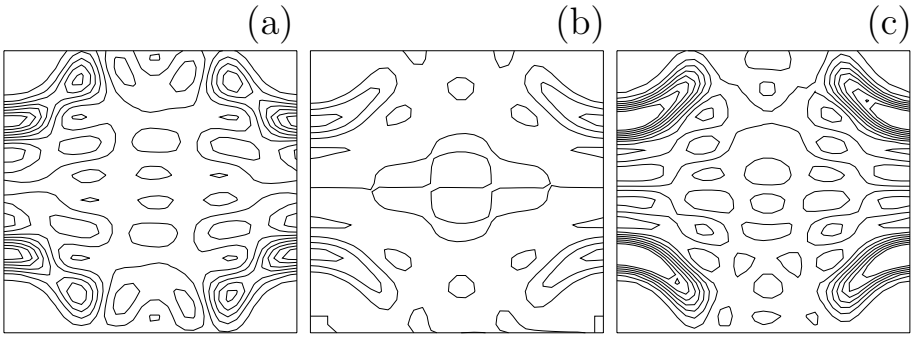

FIG. 4: The contour plots of the fluctuating charge densities of the three principal modes polarized in the cyclotron direction. The panels (a), (b) and (c) correspond to the modes "1^+", CR, and "2^+", respectively. One elementary lattice cell is shown with the antidots occupying the corners.

REFERENCES

* Electronic address: egidijus@teorfys.lu.se

[1] L. Jacak, P. Hawrylak, and A. Wójs, *Quantum Dots*, (Springer, Berlin, 1998).
[2] T. Demel, D. Heitmann, P. Grambow, and K. Ploog, Phys. Rev. Lett. **64**, 788 (1990); A. Lorke, J. P. Kotthaus, and K. Ploog, Phys. Rev. Lett. **64**, 2559 (1990).
[3] D. Weiss, K. von Klitzing, K. Ploog, and G. Weimann, Europhys. Lett. **8**, 179 (1989).
[4] D. Weiss, M. L. Roukes, A. Menschig, P. Grambow, K. von Klitzing, and G. Weimann, Phys. Rev. Lett. **66**, 2790 (1991).
[5] K. Kern, D. Heitmann, P. Grambow, Y. H. Zhang, and K. Ploog, Phys. Rev. Lett. **66**, 1618 (1991).
[6] R. Fleischmann, T. Geisel, R. Ketzmerick, Phys. Rev. Lett. **68**, 1367 (1992); É. M. Baskin, G. M. Gusev, Z. D. Kvon, A. G. Pogosov, and M. V. Éntin, JETP Lett. **55**, 678 (1992).
[7] K. Bollweg, T. Kurth, D. Heitmann, E. Vasiliadou, K. Eberl, and H. Brugger, Phys. Rev. B **52**, 8379 (1995).
[8] P. K. H. Sommerfeld, P. P. Steijaert, P. J. M. Peters, and R. W. van der Heijden, Phys. Rev. Lett. **74**, 2559 (1995).
[9] M. Hochgräfe, R. Krane, Ch. Heyn, and D. Heitmann, Phys. Rev. B **60**, 10 680 (1999).

[10] K. Bollweg, T. Kurth, D. Heitmann, E. Vasiliadou, P. Grambow, and K. Eberl, Surf. Sci. **361-362**, 766 (1996).
[11] G. Y. Wu, Y. Zhao, Phys. Rev. Lett. **71**, 2114 (1993).
[12] S. A. Mikhailov and V. A. Volkov, Phys. Rev. B **52**, 17 260 (1995).
[13] S. A. Mikhailov, Phys. Rev. B **54**, 14 293 (1996).
[14] E. Anisimovas and P. Johansson, Phys. Rev. B **60**, 7744 (1999).
[15] L. H. Thomas, Proc. Cambridge Philos. Soc. **23**, 542 (1927).
[16] E. Fermi, Z. Phys. **48**, 73 (1928).
[17] C. F. von Weizsäcker, Z. Phys. **96**, 431 (1935).
[18] F. Bloch, Z. Phys. **81**, 363 (1933).
[19] E. Zaremba and H. C. Tso, Phys. Rev. B **49**, 8147 (1994).
[20] E. Zaremba, Phys. Rev. B **53**, 10 512 (1996).
[21] B. P. van Zyl and E. Zaremba, Phys. Rev. B **59**, 2079 (1999).
[22] W. Jones and W. H. Young, J. Phys. C: Solid St. Phys. **4**, 1322 (1971).
[23] R. M. Dreizler and E. K. U. Gross, *Density Functional Theory*, (Springer, Berlin, 1990), Chap. 5.
[24] E. Runge and E. K. U. Gross, Phys. Rev. Lett. **52**, 997 (1984).
[25] M. K. Harbola, Phys. Rev. A **58**, 1779 (1998).
[26] A. Banerjee and M. K. Harbola, J. Chem. Phys. **113**, 5614 (2000).
[27] P. Hohenberg and W. Kohn, Phys. Rev. **136**, B 864 (1964).
[28] W. Kohn and L. J. Sham, Phys. Rev. **140**, A 1133 (1965).
[29] M. Levy, J. P. Perdew, and V. Sahni, Phys. Rev. A **30**, 2745 (1984).
[30] R. H. Ritchie. Phys. Rev. **106**, 874 (1957).

Tip geometry effects in circularly polarized light emission from a scanning tunneling microscope

Egidijus Anisimovas* and Peter Johansson†
Department of Theoretical Physics, University of Lund, Sölvegatan 14 A, S-223 62 Lund, Sweden

We present a calculation of the degree of circular polarization ρ, of the light emitted from a scanning tunneling microscope due to tip asymmetry. In order to take into account the essential geometrical features of an imperfect tip its shape is approximated by a tilted spheroid. We work in the non-retarded limit and use experimentally measured dielectric functions to describe the electromagnetic properties of the tip (W and Ir) and sample (noble metals) materials. The results show that the polarization can reach 20–30 % for what we think are moderately asymmetric tips. This result, as well as the strong dependence of ρ on the azimuthal observation angle, is in reasonable agreement with experimental findings [Vázquez de Parga and Alvarado, Europhys. Lett. **36**, 577 (1996)].

PACS numbers: 61.16.Ch, 73.20.Mf, 41.20.Cv

I. INTRODUCTION

Over the last decade, the scanning tunneling microscope (STM) as well as other scanning probe techniques, for example the atomic force microscope (AFM), have become standard experimental tools in surface science. The main purpose of using these techniques is to gain information about the surface topography and structure with high, often atomic, resolution. But the field of scanning probe microscopy (SPM) has also diversified in many different directions. One of the new subfields is devoted to the study of interactions between the tunneling electrons and the electromagnetic field.

In this paper, we will address experiments in which the STM is operated at a relatively large bias voltage so that some of the tunneling electrons can transfer part of their excess energy to the electromagnetic field, and in this way cause photon emission from the STM. These experiments were first carried out by Gimzewski, Berndt and co-workers,[1] but later several other groups have observed the same effect.[2] Typically these experiments used noble metal samples

(Au, Ag, or Cu) and standard tip materials (W or Ir).

The most conspicuous results of these experiments are (i) the enhancement of the emitted light intensity as compared with inverse photoemission from an isolated metal surface, and (ii) the spectral resonances in the light emission. The quantum efficiency reached 10^{-4} or even 10^{-3} to be compared with the typical inverse photoemission yield of 1 photon per 10^8 electrons impinging on the surface.

A number of theories addressing these experiments have been brought forward.[3–8] The main features of the experimental results can be explained as a result of the interaction between the tunneling electron and an interface plasmon resonance that is localized to the region between the tip and the sample. The electron transfers energy to the interface plasmon, the plasmon will then in turn decay. Most of the time this decay is due to dissipative losses to the tip and the sample, but some plasmons decay into photons. As an alternative to the two-step process outlined above, one can view the light emission process as a one-step process in which the interaction between the tunneling electrons and the electromagnetic field is enhanced because the photon states are modified near the tip and sample. In other words, the rate of spontaneous emission is enhanced.

In recent years, a few experiments have also aimed at understanding, and possibly also using, the polarization properties of the emitted light. Much of the motivation for this research comes from the fact that it could provide a technique for probing surface magnetic structure with very good spatial resolution. The optical properties of a magnetic surface are such that p-polarized light (**E** field in the plane of incidence) and s-polarized light (**E** field orthogonal to the plane of incidence) are coupled. As a consequence, the intensities of emitted left- and right-circularly polarized light may differ. Vázquez de Parga and Alvarado[9] studied a Co sample which was magnetized parallel to the surface and found that the degree of circular polarization $\rho = (I_{\text{left}} - I_{\text{right}})/(I_{\text{left}} + I_{\text{right}})$, could reach about 10 % (note that 2ρ was plotted in their paper). This is indeed a large number for a magneto-optic effect, and no good explanation of the result exists. It should also be said that later experiments by Pierce *et al.*,[10] in which a magnetic Fe sample was used, gave a much smaller degree of circular polarization.

Using a magnetic sample is, however, not the only way in which one can get emission of circularly polarized light. Also various asymmetries of the tip-sample geometry can give the same effect. (We hasten to add that such effects were compensated for in the experimental results obtained from magnetic samples.[9,10]) This issue was studied in more detail by Vázquez de Parga and Alvarado.[11] They measured the degree of circular polarization for a number

of tips, and found that ρ in some cases could reach values as high as 80 %. Vázquez de Parga and Alvarado argue that this presumably happens when the tip is asymmetric, having, for example, a knife-edge-like protrusion to one side of the apex. This kind of protrusion can yield a high degree of coupling between p and s polarization, and consequently a high degree of circular polarization of the emitted light.

In this paper, we present a theoretical investigation of the effects tip asymmetry has on the polarization properties of the emitted light. To this end, we perform calculation of the emitted light intensity from an STM with a model tip in the form of a tilted spheroid. While the ultimate goal in this research field is to understand the relation between the polarization of the emitted light and surface magnetism, there are several reasons for why it is valuable to understand the tip asymmetry problem in its own right: (i) Are the values for ρ that were found experimentally reasonable? (ii) Can this type of experiment be used as a probe of tip quality? (iii) The formalism developed here can be useful in treating the magnetic-surface problem. (iv) In spite of the fact that the experiments on magnetic surfaces were done in such a way that the straightforward consequences of any tip asymmetry are compensated for, it is not excluded that some non-trivial coupling between the two mechanisms remains. The results show that the values for ρ can reach 20–30 % and sometimes more for what we think are moderately asymmetric tips. This finding is in reasonable agreement with the experimental results.[11]

The paper is organized in the following way. In Sec. II we describe the model used in our calculations. In Sec. III we develop the mathematical formalism which leads to a set of coupled equations for the expansion coefficients of the scalar potential in prolate spheroidal coordinates which are solved numerically and related to the measurable quantities. Our main results are presented and discussed in Sec. IV, and a brief summary is given in Sec. V.

II. THE MODEL

In order to have a model tip that is *not* cylindrically symmetric we start from a spherical model tip used in most previous calculations,[3,4,6,8,12] and then stretch and tilt it to obtain a spheroid. Thus, cylindrical symmetry is lost and only a vertical symmetry plane drawn through the tilted spheroid axis is left. The geometric setup is sketched in Fig. 1 where we also show two Cartesian coordinate systems. The first one has its z axis directed normal to the sample surface, while the other (primed) one has its z' axis pointing along the major axis of the spheroid in order to facilitate the transition to the prolate spheroidal

coordinates[13] (ξ, η, ϕ). The distance between the foci of the spheroid is chosen as the unit length $a = 1$. The tip surface is given by $\xi = \xi_0 = \text{const}$ where ξ is the radial spheroidal coordinate. Its eccentricity equals $\varepsilon = 1/\xi_0$. We define the tilting angle β as the angle between the spheroid axis and vertical direction, so that $\beta = 0$ corresponds to an upright, symmetric tip. Finally, the tip-sample separation d, is the shortest distance between the tip and the sample surface.

Typical values for the tip radius are 100 – 400 Å and the tip-sample separation is of order 5 – 10 Å. Comparing these numbers with $\lambda\!\!\!^{-}$ $(\lambda/2\pi)$ for the emitted photons (typically $\lambda\!\!\!^{-} \approx 1000$ Å) we see that it is possible to calculate the electromagnetic fields around the tip in the non-retarded limit. A recent calculation[12] taking retardation into account showed that this approximation is reasonable.

The general approach of our calculation follows Ref. 3. We use the reciprocity theorem of electrodynamics[14] which states that interchanging the source with the point of measurement leaves the result unchanged. Thus, while we need to know the electric field far from the tip resulting from a driving current situated between the tip and the sample, we place the driving current far away from the tip and ask what electric field we obtain between the tip and sample. As a consequence, the amplitude of the linearly polarized electric field radiated in the direction (ϑ, ψ) (polar and azimuthal angles, respectively) can be written[3]

$$E_{p(s)}(\mathbf{r}, \omega) = \frac{i\omega}{c^2} \frac{e^{ikr}}{r} \int d^3r'\, j(\mathbf{r}', \omega) G_{p(s)}(\vartheta, \psi, \mathbf{r}', \omega). \tag{1}$$

Here $j(\mathbf{r}, \omega)$ denotes the classical current corresponding to an inelastic transition in which the tunneling electron loses energy $\hbar\omega$. The prefactor gives the amplitude of the $\mathbf{E}$ field of a plane wave coming from a δ function source of unit strength a distance r far away in the (ϑ, ψ) direction. The function $G(\vartheta, \psi, \mathbf{r}', \omega)$ is an enhancement factor resulting from the response of tip and sample. It is defined as the ratio between the vertical component of the electric field at $\mathbf{r}'$ near the tip and the electric field of the incoming plane wave. Equation (1) can be simplified by setting $G = G(\vartheta, \psi, \mathbf{r}'_{\text{apex}}, \omega)$, and taking this quantity outside the integral, because the tunneling current is non-zero only within a small region right below the tip apex $(\mathbf{r}'_{\text{apex}})$ where G is essentially independent of $\mathbf{r}'$.

Once G and $j(\mathbf{r}', \omega)$ are known, the total radiated power and its angular distribution can be calculated from Eq. (1). However, we will restrict ourselves to calculating G, because $j(\mathbf{r}', \omega)$ is rather structureless as a function of ω, and the quantity of primary interest to us, the degree of circular polarization ρ, can be obtained directly from the enhancement factor as

$$\rho = \frac{I_{\text{left}} - I_{\text{right}}}{I_{\text{left}} + I_{\text{right}}} = \frac{|G_{\text{left}}|^2 - |G_{\text{right}}|^2}{|G_{\text{left}}|^2 + |G_{\text{right}}|^2}. \tag{2}$$

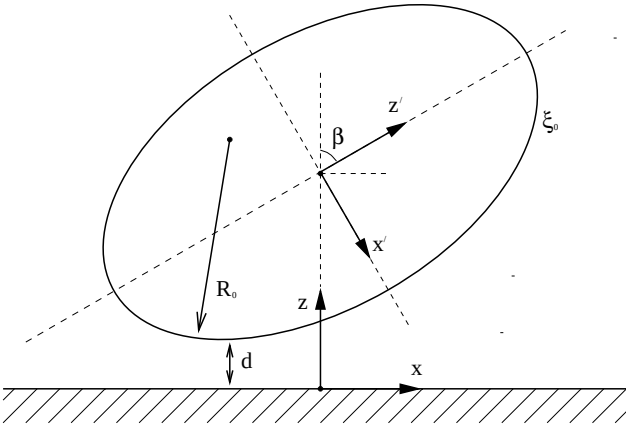

FIG. 1: The overall geometry used in our calculation.

Here the subscripts label the two circular polarization states of the *radiated* light. A simple analysis shows that their respective enhancement factors are related to the linear ones as $G_{\substack{\text{left}\\\text{right}}} = (G_p \mp iG_s)/\sqrt{2}$.

We use experimentally measured dielectric functions[15] to describe the optical properties of the tip and sample materials in the calculations. While this is an approximation, for example, damping due to extra surface scattering and electron-hole pair excitation is neglected, it is usually a rather good approximation. Reference 12 contains a more extensive discussion of this point.

III. THEORY

The calculation of the electric field enhancement factor G is done in two steps. First the "external" field $\mathbf{E}^{\text{ext}}$, which we define as the electric field above the sample surface in the absence of the spheroid, is computed. Then the spheroid is introduced, and the near-field corrections due to its presence are calculated in the second step. As a matter of fact $\mathbf{E}^{\text{ext}}$, being the electric field of a propagating wave far away from the source, is transverse. Nevertheless, within the region of interest which is smaller than λ, transverse and longitudinal fields cannot

really be distinguished. Therefore, we treat the (nearly constant) field $\mathbf{E}^{\rm ext}$ as a longitudinal one there, and express it as a gradient of a scalar potential.

The electric field created by a plane wave coming from a remote source of radiation above a reflecting dielectric surface is straightforwardly obtained by employing the Fresnel formulas. We denote the sample dielectric function $\epsilon_1(\omega)$, the strength of the electric field of the incoming light E_1, the ratio between the vertical components of its wave-vectors in the sample and vacuum $f = \sqrt{(\epsilon_1 - \sin^2\vartheta)}/\cos\vartheta$, and express the tilted frame Cartesian components of $\mathbf{E}^{\rm ext}$ as

$$\begin{aligned}\mathbf{E}_p^{\rm ext} &= \{E'_x, E'_y, E'_z\} = \frac{2E_1}{\epsilon_1 + f}\big\{ - f\cos\vartheta\cos\psi\cos\beta - \epsilon_1\sin\vartheta\sin\beta, \\ &\quad - f\cos\vartheta\sin\psi,\ -f\cos\vartheta\cos\psi\sin\beta + \epsilon_1\sin\vartheta\cos\beta\big\} \qquad (3)\end{aligned}$$

and

$$\mathbf{E}_s^{\rm ext} = \{E'_x, E'_y, E'_z\} = \frac{2E_1}{1+f}\{\sin\psi\cos\beta,\ -\cos\psi,\ \sin\psi\sin\beta\} \qquad (4)$$

for the p and s polarizations, respectively. As a result, the external potential equals $\phi^{\rm ext} = -E'_x x' - E'_y y' - E'_z z'$ and we transform this expression to the spheroidal coordinate system (ξ, η, ϕ) employing

$$\begin{pmatrix} x \\ y \end{pmatrix} = -\frac{a}{2}P_1^1(\xi)P_1^1(\eta)\begin{pmatrix} \cos\varphi \\ \sin\varphi \end{pmatrix}, \quad z = \frac{a}{2}P_1^0(\xi)P_1^0(\eta), \qquad (5)$$

where a is the interfocal distance subsequently set equal to 1,[16] and P_l^m denotes an associated Legendre function.

Let us now introduce the tilted spheroid into this external field. The effect on the scalar potential everywhere outside a body due to the (complicated) charge distribution inside it can be expressed in terms of the boundary values of the potential and its normal derivative on a surface surrounding the body. The boundary values can be interpreted as those resulting from a surface-charge density $(1/4\pi)(\partial\phi/\partial n)$ and a dipole layer $(-\phi/4\pi)$ and lead in the present case to the following equation for the potential

$$\phi(\mathbf{r}) = \phi^{\rm ext}(\mathbf{r}) + \frac{1}{4\pi}\oint_s \big\{\mathcal{G}(\mathbf{r}|\mathbf{r}')\frac{\partial}{\partial n'}\phi(\mathbf{r}') - \phi(\mathbf{r}')\frac{\partial}{\partial n'}\mathcal{G}(\mathbf{r}|\mathbf{r}')\big\}dS'. \qquad (6)$$

The integration surface S is placed just outside the spheroid (note that the positive direction of the normal points into the spheroid). The Green's function

$\mathcal{G}$ takes into account both the direct Coulomb interaction and the presence of the image charges that the spheroid induces in the sample

$$\mathcal{G}(\mathbf{r}|\mathbf{r}') = \frac{1}{|\mathbf{r}-\mathbf{r}'|} - \left(\frac{\epsilon_1 - 1}{\epsilon_1 + 1}\right) \frac{1}{|\mathbf{r}-\mathbf{r}''|}, \tag{7}$$

where $\mathbf{r}$ is any point above the sample and outside the spheroid, and $\mathbf{r}''$ is the image of $\mathbf{r}'$ in the plane. For what follows, it is useful to express the Coulomb potential in terms of functions that solve the Laplace equation in the spheroidal coordinates. We have the multipole expansion

$$\begin{aligned} \frac{1}{r} &= \frac{1}{|\mathbf{r}-\mathbf{r}'|} = \frac{2}{a} \sum_{l=0}^{\infty} \sum_{m=0}^{l} (2l+1)(2-\delta_{m,0})(-1)^m \left[\frac{(l-m)!}{(l+m)!}\right]^2 \\ &\times P_l^m(\eta) P_l^m(\eta') Q_l^m(\xi_>) P_l^m(\xi_<) \cos[m(\varphi - \varphi')] \end{aligned} \tag{8}$$

where $\xi_>$ ($\xi_<$) is the greater (lesser) of ξ and ξ', and Q_l^m is an associated Legendre function of the second kind.

Inside the spheroid, the scalar potential can be expressed as a general solution to $\nabla^2\phi = 0$ that remains finite on the interfocal line $\xi = 1$:

$$\phi(\xi, \eta, \varphi) = \sum_{l=0}^{\infty} \sum_{m=0}^{l} P_l^m(\xi) P_l^m(\eta) \left\{ \begin{array}{c} A_{lm} \cos(m\varphi) \\ B_{lm} \sin(m\varphi) \end{array} \right\}. \tag{9}$$

In fact, the modes varying as $\cos(m\varphi)$ and $\sin(m\varphi)$, respectively, do not mix thanks to the presence of the symmetry plane, and the following calculations can be carried out separately for both sets. Since in the end we are only interested in obtaining the electric field component in the symmetry plane where $\varphi = 0$ or $\varphi = \pi$ and thus $\sin(m\varphi) = 0$, we restrict the calculation to the cos-modes.

We obtain the values of $\phi(\mathbf{r}')$ and $\partial\phi(\mathbf{r}')/\partial n'$ outside the spheroid from Eq. (9) and the boundary conditions

$$\begin{aligned} \phi(\mathbf{r}')|_{\text{in}} &= \phi(\mathbf{r}')|_{\text{out}}, \\ \epsilon_2 \frac{\partial}{\partial n'} \phi(\mathbf{r}')|_{\text{in}} &= \frac{\partial}{\partial n'} \phi(\mathbf{r}')|_{\text{out}}, \end{aligned} \tag{10}$$

where $\epsilon_2 = \epsilon_2(\omega)$ denotes the tip dielectric function. Letting $\mathbf{r} \to \mathbf{r}'$ (from the outside of the spheroid) in Eq. (6), we arrive at an integral equation for the potential on the spheroid surface.

The surface integrals occurring in Eq. (6) can be evaluated explicitly using the expansions of potential and Green's function in spheroidal coordinates. We look

at the two terms in the Green's function separately. The direct term $(1/|\mathbf{r}-\mathbf{r}'|)$ yields

$$\frac{1}{4\pi}\oint_s \left\{ \frac{1}{|\mathbf{r}-\mathbf{r}'|}\frac{\partial}{\partial n'}\phi(\mathbf{r}') - \phi(\mathbf{r}')\frac{\partial}{\partial n'}\frac{1}{|\mathbf{r}-\mathbf{r}'|} \right\} dS' = -(\epsilon_2 - 1) \qquad (11)$$
$$\times \sum_{l=0}^{\infty}\sum_{m=0}^{l} A_{lm}(-1)^m \frac{(l-m)!}{(l+m)!} P_l^m(\xi_0) D_l^m(\xi_0) Q_l^m(\xi_0) P_l^m(\eta)\cos(m\varphi),$$

for which we have used the normalization conditions

$$\int_{-1}^{1} P_l^m(\eta) P_{l'}^m(\eta) d\eta = \delta_{ll'} \frac{2}{2l+1}\frac{(l+m)!}{(l-m)!} \quad \text{and}$$
$$\int_0^{2\pi} \cos(m\varphi)\cos(m'\varphi) d\varphi = \delta_{mm'} \frac{2\pi}{2-\delta_{m,0}}, \qquad (12)$$

and the shorthand notation

$$D_l^m(\xi) = \left[(\xi'^2 - 1)\frac{\partial}{\partial \xi'} P_l^m(\xi') \right]_{\xi'=\xi}. \qquad (13)$$

When evaluating the analogous integral with the reflection part of the Green's function $(1/|\mathbf{r}-\mathbf{r}''|)$ it is convenient to transfer the integration onto the image of the spheroid by changing the integration variable from $\mathbf{r}'$ to $\mathbf{r}''$, thus expressing the potential in terms of the image charges. Then the result will resemble the one in Eq. (11), but the last three factors $Q_l^m(\xi_0)P_l^m(\eta)\cos(m\varphi)$ which describe the lm mode on the spheroid surface have to be replaced by $Q_l^m(\tilde{\xi})P_l^m(\tilde{\eta})\cos(m\tilde{\varphi})$ where $\tilde{\xi}, \tilde{\eta}, \tilde{\varphi}$ are the coordinates of the point $\mathbf{r}$ in the frame associated with the spheroid image.

Of course, in order to transform the integral equation (6) into a matrix equation for the expansion coefficients A_{lm}, one has to expand the modes centered on the spheroid image in terms of modes centered on the spheroid. This will couple the different modes. We get

$$-\left(\frac{1-\epsilon_1}{1+\epsilon_1}\right)(\epsilon_2 - 1)\sum_{l'=0}^{\infty}\sum_{m'=0}^{l'} A_{l'm'}(-1)^{m'}\frac{(l'-m')!}{(l'+m')!}$$
$$\times P_{l'}^{m'}(\xi_0) D_{l'}^{m'}(\xi_0) Q_{l'}^{m'}(\tilde{\xi}) P_{l'}^{m'}(\tilde{\eta})\cos(m'\tilde{\varphi}) \qquad (14)$$
$$= \left(\frac{1-\epsilon_1}{1+\epsilon_1}\right)(\epsilon_2 - 1)\sum_{l=0}^{\infty}\sum_{m=0}^{l} M_{lm}(\xi_0) P_l^m(\eta)\cos(m\varphi),$$

where the coefficients $M_{lm}(\xi_0)$ are obtained from the orthogonality conditions for $P_{lm}(\eta)$ and $\cos(m\varphi)$

$$\begin{aligned} M_{lm}(\xi_0) &= -\sum_{l'=0}^{\infty}\sum_{m'=0}^{l'} \frac{2-\delta_{m,0}}{2\pi}\frac{2l+1}{2}(-1)^{m'}\frac{(l-m)!}{(l+m)!} \\ &\times \frac{(l'-m')!}{(l'+m')!}P_{l'}^{m'}(\xi_0)D_{l'}^{m'}(\xi_0)\mathcal{J}_{l'm'}^{lm}A_{l'm'} \end{aligned} \tag{15}$$

and the overlap integral

$$\mathcal{J}_{l'm'}^{lm} = 2\int_{-1}^{1}d\eta\int_{0}^{\pi}d\varphi\, Q_{l'}^{m'}(\tilde{\xi})P_{l'}^{m'}(\tilde{\eta})P_{l}^{m}(\eta)\cos(m'\tilde{\varphi})\cos(m\varphi) \tag{16}$$

is the projection of the mode $l'm'$ centered on the image spheroid onto the mode lm centered on the spheroid.

Substituting Eq. (11), its reflected counterpart Eq. (14), and ϕ^{ext} expressed as

$$\phi^{\text{ext}}(\xi,\eta,\varphi) = \sum_{l=0}^{\infty}\sum_{m=0}^{l} P_l^m(\xi)P_l^m(\eta)\left\{\begin{array}{l} f_{lm}\cos(m\varphi) \\ g_{lm}\sin(m\varphi)\end{array}\right\} \tag{17}$$

(note that in view of Eqs. (3), (4), and (5) only f_{10}, f_{11}, and g_{11} have non-zero values) into the integral equation (6) and collecting the contributions to each mode $P_l^m(\eta)\cos(m\varphi)$, we arrive at the following matrix equation for the expansion coefficients A_{lm}

$$\sum_{l'=0}^{\infty}\sum_{m'=0}^{l'} T_{l'm'}^{lm}A_{l'm'} = f_{lm}P_l^m(\xi_0). \tag{18}$$

The matrix elements $T_{l'm'}^{lm}$ are given by

$$\begin{aligned} T_{l'm'}^{lm} &= (\epsilon_2-1)\left\{\mathcal{J}_{l'm'}^{lm}\left(\frac{1-\epsilon_1}{1+\epsilon_1}\right)\frac{2-\delta_{m,0}}{2\pi}\frac{2l+1}{2}\frac{(l-m)!}{(l+m)!} + Q_l^m(\xi_0)\delta_{ll'}\delta_{mm'}\right\} \\ &\times (-1)^{m'}\frac{(l'-m')!}{(l'+m')!}P_{l'}^{m'}(\xi_0)D_{l'}^{m'}(\xi_0) + P_l^m(\xi_0)\delta_{ll'}\delta_{mm'}. \end{aligned} \tag{19}$$

Solving Eq. (18) we obtain the expansion coefficients A_{lm} from which the potential and the electric field in the symmetry plane can be determined. The

electric field enhancement factor at the tip apex is found by letting $E_1 = 1$ and evaluating the normal derivative of the potential which yields

$$G = 2\epsilon_2 \sqrt{\frac{\xi_0^2 - 1}{\xi_0^2 - \eta_0^2}} \sum_{l=0}^{\infty} \sum_{m=0}^{l} A_{lm} P_l^m(\eta_0) \left[\frac{\partial}{\partial \xi} P_l^m(\xi) \right]_{\xi=\xi_0} . \tag{20}$$

The expressions for ξ_0 and η_0, together with those for the principal radii of curvature, are given in the Appendix.

The calculation of the overlap integrals and matrix inversion is carried out numerically. We include a sufficient number of modes in order to get a converged solution, and truncate the rest of the matrix. The maximum l that has to be included to calculate the field enhancement factors can be estimated to be R_0/d. However, the degree of polarization, which is expressed through the ratio of two different enhancement factors, converges considerably faster.

IV. RESULTS AND DISCUSSION

We have used the expressions derived in Sec. III to calculate frequency and directional dependencies of the enhancement factors $|G|$ and the degree of polarization ρ for a number of different geometric setups. In most of our calculations we used a W tip and a Au sample, occasionally switching to an Ir tip and a Ag sample.

We varied the spheroid stretching factor $\Lambda = r_2/r_1$ between the limits $\sqrt{3/2} \approx 1.2247$ and 2 and the tilting angle between 15° and 75°. The constraints on possible geometries are set by the validity of our approximation. To be able to work correctly in the non-retarded limit one cannot go to too large Λ values. Moreover, extending the model tip too much leads not only to changes of the shape of the bottom of the tip, but also to a distortion of overall geometric setup. As a measure of such a distortion one can consider the ratio of the two principal radii of curvature at the tip apex. It can be seen from Eqs. (24) and (25) that its difference from unity is given by

$$1 - \frac{R_1}{R_0} = (\epsilon \sin \beta)^2 \tag{21}$$

and that this difference stays below 1/6 (a reasonably small quantity) as long as e. g. $\Lambda \leq \sqrt{3}$ and $\beta \leq 30°$.

When changing from one geometry to another we choose to keep the ratio R_0/d (where d is the tip-sample separation) fixed. Previous calculations using spherical model tips showed that this quantity is the essential one in determining

the characteristics of the electromagnetic response. In fact, in the spherical geometry all the characteristic lengths (the radius of curvature at the apex, the total horizontal size of the cavity and the vertical extension of the tip) are determined by its radius. Introducing more degrees of freedom decouples different characteristic lengths from each other and makes the choice of the "essential" ones more involved. As we will see, the resonance frequencies are mostly determined by horizontal dimensions of the cavity while the magnitude of the response is mainly determined (in a non-retarded calculation) by the vertical size of the tip. The degree of polarization, however, is not particularly sensitive to these quantities (see below).

In Fig. 2, we show how the light polarization varies with the azimuthal observation angle ψ. One sees that the maximum of the degree of polarization occurs at $\psi = \pi/2$ and $\psi = 3\pi/2$ as one may expect since the tip-shape distortion is maximally exposed when seen from the direction perpendicular to the symmetry plane. (Consequently, we present the other dependencies as observed in the direction $\psi = 3\pi/2$ where ρ assumes the largest positive values.) The light radiated along the symmetry plane, on the other hand, is not circularly polarized. It can be seen, however, that the maxima of the enhancement factors are not necessarily observed in the direction of largest polarization.

Another easily noticeable feature is the very nearly sinusoidal shape of the calculated degree of polarization which resembles that measured experimentally.[11] In fact, a closer inspection would reveal an admixture of a few percent of higher modes (i. e. $\propto \sin 2\psi, \sin 3\psi, \ldots$) whose magnitude grows with the nonsphericity of the tip. Obviously, the presence and relative magnitudes of these modes are very much geometry dependent both in the theoretical model and in the experimental situation. This means that if it becomes possible to measure the contribution of the second and higher modes experimentally (which is clearly beyond the experimental accuracy at present) information about the actual shape of the tip could be revealed. Also it is worth mentioning that, as our results indicate, the higher harmonics become more easily detectable at smaller observation angles ϑ.

In Fig. 3 we show a typical polar observation angle dependency of the degree of polarization which develops a very high peak at $\vartheta \approx 0.1$ rad. Its presence is easy to understand recalling that for such a small observation angle the $\mathbf{E}$ fields of both s- and p-polarized light are nearly horizontal. However, in the case of s-polarization the field vector lies in the symmetry plane and thus the tip shape distortion is maximally exposed to it but not to the p-polarized light. One sees in Fig. 3 that in this limit the enhancement factor $|G_p|$ goes to zero while $|G_s|$ approaches a rather small but finite value. The maximum in ρ occurs when $|G_p|$ and $|G_s|$ have approximately equal values.

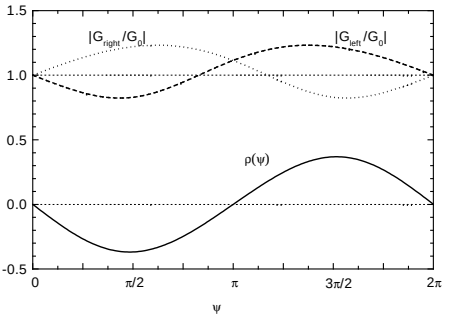

FIG. 2: The azimuthal-angle dependency of the enhancement factors for circularly polarized light and the resulting degree of polarization for a W/Au tip-sample combination at the frequency 2.1 eV. The other parameter values are $\Lambda = \sqrt{3}$, $\beta = \pi/4$ and the polar observation angle $\vartheta = \pi/4$. The enhancement factors are normalized to their common value $|G_0| = 21.92$ in the direction $\psi = 0$.

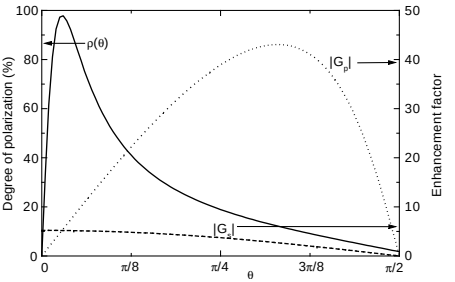

FIG. 3: The polar-angle dependency of enhancement factors for linearly polarized light and the resulting degree of polarization for a W/Au tip-sample combination at the frequency 2.1 eV. The other parameter values are $\Lambda = \sqrt{2}$, $\beta = \pi/6$ and the azimuthal observation angle $\psi = 3\pi/2$. Note the two different vertical scales.

It would be interesting if such an angular distribution of the light polarization could be detected experimentally. However, one should keep in mind that measurements near the vertical direction ($\vartheta \approx 0.1$ rad) are complicated or even impossible because the light is shadowed by the tip. Also it can be seen from Fig. 3 that most of the radiated intensity goes into the p-channel and is concentrated in a rather narrow region centered at $\vartheta \approx 1$ rad. Inside this region, one should be able to detect a steady growth of the degree of polarization with decreasing polar observation angle ϑ.

Now let us turn to the frequency dependency of the radiated light concentrating on its polarization. In Figs. 4 and 5 the different enhancement factors and the degrees of polarization versus frequency are plotted. One sees that $|G_p|$ is essentially the same as in a spherical-tip model[3] while the maximum of the $|G_s|$ response is shifted towards higher frequencies. As a consequence of this, the degree of polarization (which is elsewhere a smooth function of photon energy) develops a characteristic peak at frequencies slightly higher than the spherical-tip resonances, i.e. in the frequency range where $|G_p|$ drops rather abruptly. The possibility to observe the peak in practice is very much dependent on the light intensity which is determined by the materials in use. In the case of our

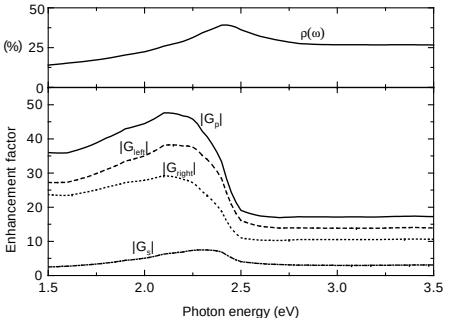

FIG. 4: The frequency dependencies of the enhancement factors and the resulting degree of polarization. The results presented here are those obtained for a W tip scanning a Au sample with $\Lambda = \sqrt{3}$ and $\beta = \pi/6$. The observation direction is $\psi = 3\pi/2$, $\vartheta = \pi/4$.

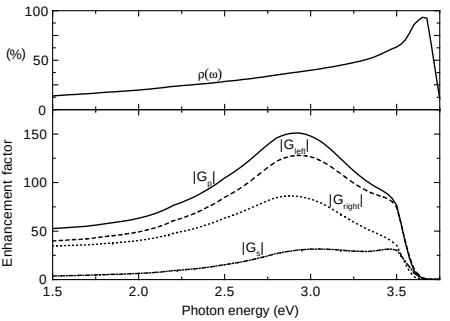

FIG. 5: The frequency dependencies of the enhancement factors and the resulting degree of polarization. The results presented here are those obtained for an Ir tip scanning a Ag sample. The rest of the parameter values are the same as in Fig. 4.

model calculation performed for a W tip and a Au sample, the resonance is found to be rather broad and the light intensities remain quite large after it occurs. This would imply that the above mentioned peak should be possible to observe.

The numerical values of the degree of polarization are directly dependent on the tip asymmetry. In Table I we show the numbers for various geometries. One can see that their typical values are of the order of several tens of percent, thus comparable to the experimental results.[11] It is also easy to trace their growth with increasing spheroid stretching factor and tilting (note that when β approaches $\pi/2$ the polarization decreases because then the tip again becomes more symmetric). On the other hand, it is worth noticing that the degree of polarization in contrast to other characteristic features (the magnitude and resonant frequencies) of the response is not sensitive to the relative size of the tip radius compared to the tip-sample separation. All our calculations are done for $R_0/d = 20$ except for those presented in parentheses in Table I which are obtained for $R_0/d = 40$.

The frequency at which the maximum of $\rho(\omega)$ occurs was also found to be stable at 2.4 eV for a W tip and a Au sample independently of the geometry. When the asymmetry increases and the two principal radii of curvature start to differ considerably [see Eq. (21)] one expects a blue shift of the maximum in the polarization since the size of the resonant cavity becomes effectively smaller.

	Λ			
β	$\sqrt{3/2}$	$\sqrt{2}$	$\sqrt{3}$	2
15°	10.1	15.3 (15.8)	20.3 (20.7)	22.7
30°	18.5	28.9 (29.8)	39.1 (40.2)	44.3
45°	23.3	37.6	53.7	62.1
60°	22.1	38.1	58.4	69.9
75°	13.8	25.5	43.1	55.0

TABLE I: The maximum degree of polarization for a W tip and a Au sample at the photon energy $\hbar\omega = 2.4$ eV measured in the direction $\vartheta = \pi/4$ and $\psi = 3\pi/2$. All values were obtained with $R_0/d = 20$, except those within parenthesis for which $R_0/d = 40$.

We noticed this for an Ir tip and a Ag sample where one has sharper resonances, but it was almost not discernible for a W tip and a Au sample.

Our model geometry can also be used to provide some insight into the calculations of electromagnetic response in the case of a symmetric tip. Leaving aside other details, one can argue that the spectra are characterized by the peak positions and peak heights. Earlier investigations (see, for example Refs. 3,8,18) have already addressed the question of dependency of these quantities on the radius of curvature of the spherical tip compared to the tip-sample separation. Having introduced more degrees of freedom into the model geometry we present in Fig. 6 a calculation of the enhancement factor $|G_p|$ for an upright prolate ($\Lambda = \sqrt{2}$) spheroid (curve 2) and compare it with the results obtained from two spherical-tip calculations: (curve 1) the one of the same radius of curvature at the bottom and the one of the same height (curve 3) as depicted in the inset. These results show that the magnitude of the response in this model is mainly determined by the vertical extension of the tip while the resonant frequency is more sensitive to the shape of the resonant cavity formed between the tip and the sample. Of course, in a fully retarded treatment the growth of the magnitude of the response with increasing vertical extension will eventually be cut off once the tip "height" becomes larger than $\lambda\!\!\!^{-}$ or so.

V. SUMMARY

We have investigated the effects of tip asymmetry on the polarization properties of light emitted from a scanning tunneling microscope. We find a number of characteristic features in the directional and frequency dependencies of the degree of circular polarization ρ: (i) It has a nearly sinusoidal dependence on the azimuthal observation angle. Moreover, (ii) ρ grows with decreasing polar observation angle and (iii) as a function of photon energy its maximum is blue-shifted compared with the maximum of the total light emission intensity. The resulting numerical values of the degree of polarization are rather large (up to

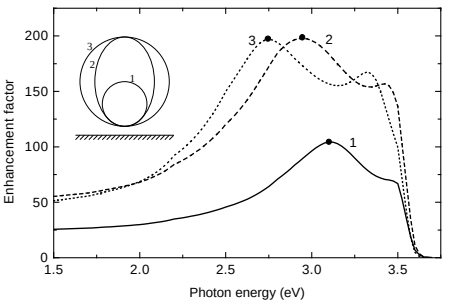

FIG. 6: The cylindrically symmetric tip response functions: Curves 1 and 3 show results for spherical tips with $R = 100$ Å and $R = 200$ Å, respectively; curve 2 shows results for a spheroidal tip whose total height is that of the curve-3 sphere, and the radius of curvature at the bottom is that of the curve-1 sphere. The tip sample separation is 5 Å.

50 %) even for moderately distorted tips and are comparable to those measured experimentally.[11]

Some of these results, such as the relative blue-shift of the circular polarization, indicate that, at least for the geometries we have considered, polarization and enhancement of the emitted light are somewhat separate effects, even though they both originate from the presence of the tip near the sample. Furthermore, in the numerical calculations a larger number of basis functions are needed to accurately describe the enhancement of the light intensity than to get a correct value for the polarization. These results can qualitatively be understood in the following way: The enhancement is determined by the tip-sample geometry in the part of space where the tip and sample are in close proximity to each other; this is where the interface-plasmon mode is formed. The polarization, on the other hand, mainly results from the interaction between the outgoing electromagnetic waves and the tip as a whole.

ACKNOWLEDGMENTS

One of us (P.J.) is supported by the Swedish Natural Science Research Council (NFR).

APPENDIX

For practical purposes it is convenient to work in terms of the stretching factor of the spheroid, defined as the ratio of its major and minor axes, $\Lambda = r_2/r_1$ and

the tilting angle β as shown in Fig. 1. Straightforward geometric considerations lead to the following expressions for the spheroidal coordinates of the apex (lowest point) of the tip in terms of Λ and β

$$\xi_0 = \frac{1}{\varepsilon} = \frac{\Lambda}{\sqrt{\Lambda^2 - 1}}, \quad \eta_0 = \frac{1 + \xi_0 \cos\gamma_0}{\xi_0 + \cos\gamma_0}, \tag{22}$$

where

$$\gamma_0 = \pi/2 + \beta + \arccos(\epsilon \sin\beta). \tag{23}$$

For the radius of curvature in the symmetry plane we get

$$R_0 = \frac{a}{2} \frac{\xi_0^2(\xi_0^2 - 1)}{(\xi_0^2 - \sin^2\beta)^{3/2}}. \tag{24}$$

It can be shown that this is one of the two principal radii of curvature while the other one equals

$$R_1 = \frac{a}{2} \frac{\xi_0^2 - 1}{\sqrt{\xi_0^2 - \sin^2\beta}}. \tag{25}$$

REFERENCES

* Electronic address: egidijus@teorfys.lu.se
† Electronic address: epj@teorfys.lu.se

[1] J. K. Gimzewski, B. Reihl, J. H. Coombs, and R. R. Schlittler, Z. Phys. B **72**, 497 (1988); J. K. Gimzewski, J. K. Sass, R. R. Schlittler, and J. Schott, Europhys. Lett. **8**, 435 (1989); R. Berndt, J. K. Gimzewski, and P. Johansson, Phys. Rev. Lett. **67**, 3796 (1991); R. Berndt and J. K. Gimzewski, Phys. Rev. B **48**, 4746 (1993).

[2] I. I. Smolyaninov, V. S. Edelman, and V. V. Zavyalov, Phys. Lett. A **158**, 337 (1991); V. Sivel, R. Coratger, F. Ajustron, and J. Beauvillain, Phys. Rev. B **45**, 8634 (1992); K. Ito, S. Ohyama, Y. Uehara, and S. Ushioda, Surf. Sci. **324**, 282 (1995); T. Umeno, R. Nishitani, A. Kasuya, and Y. Nishina, Phys. Rev. B **54**, 13 499 (1996); Ph. Dumas, C. Syrykh, I. V. Makarenko, and F. Salvan, Europhys. Lett. **40**, 447 (1997).

[3] P. Johansson, R. Monreal, and P. Apell, Phys. Rev. B **42**, 9210 (1990); P. Johansson and R. Monreal, Z. Phys. B **84**, 269 (1991).

[4] B. N. J. Persson and A. Baratoff, Phys. Rev. Lett. **68**, 3224 (1992).

[5] W. Denk and D. W. Pohl, J. Vac. Sci. Technol. B **9**, 510 (1991).

[6] Y. Uehara, Y. Kimura, S. Ushioda, and K. Takeuchi, Jpn. J. Appl. Phys. **31**, 2465 (1992).

[7] A. Madrazo, M. Nieto-Vesperinas, and N. Garcia, Phys. Rev. B **53**, 3654 (1996).
[8] A. Downes, M. E. Taylor, and M. E. Welland, Phys. Rev. B **57**, 6706 (1998).
[9] A. L. Vázquez de Parga and S. F. Alvarado, Phys. Rev. Lett. **72**, 3726 (1994).
[10] D. T. Pierce, A. Davies, J. A. Stroscio, and R. J. Celotta, Appl. Phys. A **66**, S403 (1998).
[11] A. L. Vázquez de Parga and S. F. Alvarado, Europhys. Lett. **36**, 577 (1996).
[12] P. Johansson, Phys. Rev. B **58**, 10 823 (1998).
[13] P. M. Morse and H. Feshbach, *Methods of Theoretical Physics* (McGraw-Hill, New York, 1953).
[14] L. D. Landau, E. M. Lifshitz, and L. P. Pitaevskii, *Electrodynamics of Continuous Media* (Pergamon, Oxford, 1984), 2nd ed., pp. 308–309.
[15] J. H. Weaver, C. Krafka, D. W. Lynch, and E. E. Koch, *Physik Daten* (Fachinformationszentrum, Karlsruhe, 1981).
[16] Note, that we used the definition of the associated Legendre polynomials $P_l^m(x)$ as given in Ref. 17 which involves a sign factor $(-1)^m$ for $|x| < 1$ only. Hence the minus sign in the expression for x and y in Eq. (5).
[17] M. Abramowitz and I. Stegun, *Handbook of mathematical functions* (Dover, New York, 1970).
[18] R. W. Rendell and D. J. Scalapino, Phys. Rev. B **24**, 3276 (1981).